Deutsches Zentrum
DLR für Luft- und Raumfahrt
Raumflugbetrieb und
Astronautentraining

FSD Flight System Dynamics | RWTH AACHEN UNIVERSITY

Master Thesis

ANALYSIS OF DISTURBANCE TORQUES ON SATELLITES IN LOW-EARTH ORBIT BASED UPON GRACE

This work was submitted to

Department of Flight System Dynamics (FSD)
Univ.-Prof. Dr.-Ing. Dieter Moormann
Faculty of Mechanical Engineering
RWTH Aachen

by

Michael Tolstoj

Supervisors:

Dipl.-Ing. Yavor Dobrev
FSD, RWTH Aachen

Dr. rer.-nat. Jacobus Herman
GSOC, Deutsches Zentrum für Luft- und Raumfahrt

Aachen, Juli 2017

Eigenständigkeitserklärung

Hiermit versichere ich, dass ich die vorliegene Masterarbeit selbständig verfasst habe. Ich versichere, dass ich keine anderen als die angegebenen Quellen und Hilfsmittel benutzt und alle wörtlich oder sinngemäß aus anderen Werken übernommenen Aussagen als solche gekennzeichnet habe.

Aachen, den 27. Juli 2017

_____

(Unterschrift)

Kurzfassung

GRACE (Gravity Recovery and Climate Experiment) ist eine wissenschaftliche Mission, initiiert durch die beiden Principle Investigators UTCSR (University of Texas, Center for Space Research) und GFZ (Geoforschungszentrum Potsdam). Die Nutzlast wurde vom Unternehmen JPL (Jet Propulsion Laboratory) gefertigt, welches gleichzeitig für Nutzlast- und Softwarebetrieb verantwortlich ist. Für den Satellitenbetrieb ist das GSOC (German Space Operation Center) zuständig.
In 2002 wurden zwei baugleiche Satelliten in einen polaren Orbit in 500 km Höhe geschossen. Das Missionsziel ist die Untersuchung des Gravitationsfeldes der Erde mit deutlich erhöhter Genauigkeit, verglichen mit Vorgängermissionen. Die Mission übertraf die ursprünglich geplante Dauer von fünf Jahren deutlich. Bis heute werden wissenschaftliche Daten produziert, trotz der reduzierter Leistungsfähigkeit der Batterie in den letzten Jahren. Die Erkenntnisse erlauben Aussagen sowohl hinsichtlich der Zeitvariation des hydrologischen Zykluses als auch das Alterungsverhalten und die Langzeitstabilität des Raumsegments.

Die Lageregelung der Satelliten wird gewährleistet durch drei magentische Torquerods und ein Kaltgas-Antriebssystem bestehend aus 12 Schubdüsen. Während der Analyse der Telemetrie wurde ein Unterschied zwischen den Aktivierungszeiten der Schubdüsen beobachtet, besonders deutlich bei Betrachtung des Rollverhaltens. Dieser asymmetrische Betrieb deutet auf einen periodischen Störeffekt hin, der die Satelliten sich abwechselnd in positive und negative neigen lässt bei einer Periode von etwa 322 Tagen. Ein präzises Verständnis aller Störkräfte ist enorm wichtig. Lagestörungen durch das Gravitationsfeld, die für die Erstellung des Feldmodells notwendig sind, können nur ermittelt werden, wenn alle weiteren Störgrößen herausgerechnet werden können.

Primäres Ziel dieser Arbeit ist die Analyse des genannten Effektes und die Ermittlung seines Ursprungs, um so neues Verständnis im Hinblick auf Langzeit-Störeffekte auf niedrigfliegende Satelliten zu erhalten. Hierfür werden zwei möglich Effekte untersucht: Der Strahlungsdruck der Sonne, sowie magnetische Störeffekte. Letztere könnten als Ursache die Wechselwirkung von Stromflüssen im Satelliten mit dem Erdmagnetfeld haben. Besonders interessant is die Möglichkeit ungewollter Ströme in den Solarpanelen. Für die Analyse aller Szenarien werden entsprechende Modelle konstruiert. Alle Störeffekte werden auf langen sowie kurzen Zeitskalen betrachtet und so die Einflüsse auf die Lagestabilität der Satelliten spezifiziert.

Schlagwörter: GRACE, Gravitationsfeld, Lageregelung, Magnetische Störeffekte, Solarpanele

Abstract

GRACE (Gravity Recovery and Climate Experiment) is a scientific mission initiated by its principal investigators UTCSR (University of Texas Center for Space Research) and GFZ (Geoforschungszentrum Potsdam). The payload was built by JPL (Jet Propulsion Laboratory) who are also responsible for payload and software operations. Satellite operations are handled by GSOC (German Space Operation Center).
In 2002 two identical satellites were launched into a polar orbit at 500 km altitude to measure the gravity field of the Earth with significantly increased accuracy compared to other missions. Designed for a mission duration of 5 years, the two satellites surpassed expectations and continue to provide scientific data to date despite the declining performance of the battery in recent years. Other important insight is gained on the time-dependent variations of the hydrological cycle as well as long-term behavior and degradation of the space segment.

Attitude control is provided by three magnetic torque rods and a cold gas propulsion system with 12 thrusters. During the analysis of telemetry data a difference in thruster on-time has been observed, especially when looking at thrusters that control positive and negative roll rates. This asymmetric operation indicates a periodic disturbance effect which tilts the satellite in the respective roll direction alternately with a period of roughly 322 days. An accurate understanding of the cause is highly important. Disturbances due to the gravity field and its variations can only be deduced if all disturbance torques are removed from the measurements.

The goal of this work is to analyze the aforementioned effect, determine its origin and gain new insight on long-period disturbance forces on satellites in low-earth orbits. For that two possible effects will be analyzed: the solar radiation pressure and magnetic disturbance forces. The latter could originate from the interaction of current flows within the satellite – especially the body mounted solar arrays – and the magnetic field. Models are developed for all scenarios. In addition to the long-term effect, the simulation is done on the time scale of single orbits, to include shorter-term effects of the disturbance forces in the analysis.

Keywords: GRACE, Gravity Field, Attitude Control, Magnetic Disturbances, Solar Panels

Contents

List of abbreviations

AHM	Attitude Hold Mode.
AOCS	Attitude and Orbit Control System.
ATH	Attitude Thruster.
AU	Astronomical Unit.
BAHM	Backup Attitude Hold Mode.
BOL	Beginning of Life.
BSM	Backup Science Mode.
CESS	Coarse Earth and Sun Sensor.
CFRP	Carbon Fiber Reinforced Plastic.
CHAMP	Challenging Minisatellite Payload.
CICPM	CESS IMU Coarse Pointing Mode.
CMCPM	CESS Magnetometer Coarse Pointing Mode.
COG	Center of Gravity.
COM	Center of Mass.
DC	Direct Current.
DOY	Day of Year.
ERDM	Emergency Rate Damping Mode.
FFT	Fast Fourier Transformation.
GFO	GRACE Follow-On.
GFZ	Geoforschungszentrum Potsdam.
GN2	Gaseous Nitrogen.
GOCE	Gravity Field and Steady-State Ocean Circulation Explorer.
GPS	Global Positioning Sysytem.
GRACE	Gravity Recovery and Climate Experiment.
GSOC	German Space Operation Center.
IAGA	International Association of Geomagnetism and Aeronomy.
ICU	Instrument Control Unit.

IGRF	International Geomagnetic Reference Field.
IMU	Inertia Measurement Unit.
IPU	Instrument Processing Unit.
JPL	Jet Propulsion Laboratory.
LSQ	Least Squares.
MET	Mission Elapse Time.
MTE	Mass Trim Electronics.
MTQ	Magnetic Torque Rods.
MWI	Microwave Instrument.
NASA	National Aeronautics and Space Administration.
OBC	On-Board Computer.
OBDH	On-Board Data Hub.
OTH	Orbit Thruster.
PCDU	Power Control and Distribution Unit.
PWM	Pulse Width Modulator Error.
RAAN	Right Ascension of the Ascending Node.
RDM	Residual Dipole Moment.
RES	Residue.
RFEA	Radio Frequency Electronics Assembly.
SA	Solar Array.
SCA	Star Camera Assembly.
SM	Science Mode.
SMC	Science Magnetic Control.
SRP	Solar Radiation Pressure.
TM	Telemetry.
TOT	Thruster On-Time.
USA	United States of America.
UTCSR	University of Texas, Center for Space Research.
WHM	Weilheim.
ZARM	Center of Applied Science Technology and Micro-gravity.

Directory of symbols

Symbol	Unit	Description
		GREEK SYMBOLS
α	$[-]$	Incident angle of light
β	[deg]	Orbit beta angle
ε	$[-]$	Reflectivity of a surface
γ	[deg]	Angle of rotation of a panel relative to the satellite coordinate frame
ω	[1/s]	Angular velocity
		LATIN SYMBOLS
a	$[-]$	Factor used for a least squares calculation
b	$[-]$	Factor used for a least squares calculation
c	$[\mathrm{m/s}]$	Speed of light
h	[m]	Orbital altitude
i	[A]	Current
m	$[\mathrm{Am}^2]$	Magnetic dipole moment
n	$[-]$	Number of windings of a coil
p	$[\mathrm{kgm/s}]$	Momentum
r	[m]	Momentum lever
t	[s]	Time
A	$[\mathrm{m}^2]$	Area
B	[T]	Magnetic field vector
C	$[-]$	Rotation matrix
F	[N]	Force
G	$[\mathrm{m}^3/(\mathrm{kgs}^2)]$	Gravitational Constant of the Earth
H	[Nms]	Angular momentum

Symbol	Unit	Description
I	$[\mathrm{kgm}^2]$	Momentum of inertia
K	$[-]$	Coordinate frame
M	$[\mathrm{kg}]$	Mass
P	$[\mathrm{N}/\mathrm{m}^2]$	Pressure
R	$[-]$	Factor comparing two values of angular momentum
S	$[-]$	Solar vector
T	$[\mathrm{Nm}]$	Torque
U	$[\mathrm{s}]$	Orbital period

Directory of subscripts

Symbol	Description
1	Magnetic Torque Model #1
2	Magnetic Torque Model #2
ATH	Attitude Thruster
b	Satellite body frame
d	diffuse
est	estimated
h1	First half of a cycle
h2	Second half of a cycle
i	Placeholder for a consecutive numbering
IGRF	International Geomagnetic Reference Model
L	Lorentz
left	Left panel
LSQ	Least squares
MAG	Magnetic
MM	Magnetometer
MTQ	Magnetic Torque Rod
pole	Magnetic pole
r	reflection
right	Right panel
SRP	Solar Radiation Pressure
top	Top panel
x	Coordinate frame X-axis
y	Coordinate frame Y-axis
z	Coordinate frame Z-axis

1 Introduction

1.1 Motivation

The first satellite, Russian Sputnik 1, was launched in 1957. Since then the number of satellites has grown enormously while the scope of applications has been expanding continuously. Scientific data provided by satellites has augmented our knowledge and understanding of our world and the universe itself. Technical possibilities in the fields of telecommunication, navigation and Earth observation have interconnected the population of the world, and have become an inherent part of our life. In recent decades awareness has been raised of topics such as climate change, melting ice caps and the rise of sea levels. The assessment and monitoring of these processes function as an early-warning system for natural disasters. An essential observable in regard to all of these processes is the terrestrial gravity field. Monitoring its temporal variation allows drawing direct conclusions on the distribution and shift of mass inside the planet. This provides valuable knowledge about geodynamics, the hydrological cycle and other fields of interest. Further, the data is used for attitude and orbit control of satellites.

The history of experiments measuring the gravitational force goes back to 17th century. Back then the first method to determine the gravitational acceleration g using a pendulum was introduced by Huygens. Advances in the field of gravimetry and the development of different types of gravimeters in the course of the 20th century allowed increasingly accurate determination of the local gravity.[1] Today Earth-based technologies provide highly precise, but only point wise measurements [2]. The dawn of the space flight era opened up the way for orbit-based Earth observation and scientific experiments. The first global gravity field model was published as early as 1966 [3].
Over the last two decades three scientific missions were launched with the main mission goal of analyzing the gravity field. The first mission was the Challenging Minisatellite Payload (CHAMP) in 2000, followed by its direct successor the Gravity Recovery and Climate Experiment (GRACE) in 2002, and the Gravity Field and Steady-State Ocean Circulation Explorer (GOCE) in 2009. Only the GRACE satellites are still operational thanks to a very reliable performance far beyond the planned mission duration of 5 years. The basic principle behind the measurement is similar for all missions: The imperfect form of the geoid and the inhomogeneous distribution of mass inside it cause perturbations in a satellite's orbit. Tracking these

perturbations makes it is possible to derive the local magnitude of the gravitational field. Consecutive measurements reveal the temporal variation. Individual technological implementations were designed for each mission. The methods include orbit tracking via GPS and filtering of non-gravitational perturbations with accelerometers.[4], [5], [6] The unique feature of GRACE is the inter-satellite ranging. Two identical satellites move in the same orbit about 220 km apart. A microwave instrument determines fluctuations of the relative distance in the order of $1 \cdot 10^{-6}$ m [7]. The accuracy of the derived gravity field models is substantially improved compared to all previous missions [4].

The GRACE satellites collect a sufficient amount data to generate a new model every 30 days. The benefit of a continuous monitoring of the field and its variation has become more apparent in recent years [8]. To provide the availability of data during the next years a successor mission named GRACE Follow-On (GFO) is set to launch in 2018. GFO utilizes a very similar principle for data collection, proving the success of the inter-satellite ranging technology. Additionally to the ranging technology used with GRACE, GFO will test a laser-based ranging interferometer that could further increase ranging accuracy [7]. The GRACE mission is planned to continue as long as possible to shorten a data gap until the launch of GFO [8].

1.2 Investigating disturbances from GRACE telemetry

A precise measurement of the inter-satellite distance is necessary at all times, to guarantee a high accuracy of the gravity field model. Profound understanding of all occurring disturbance forces is crucial to subtract their influence on the satellite's attitude and receive only the effect of the gravity gradient. A huge amount of telemetry is available thanks to the remarkably long mission duration of more than 15 years. Thorough analysis of the data can provide new insight on satellite-specific short-term attitude behavior as well as the long-term stability of the general satellite design. Unfavorable degradation can have an influence on the magnitude of particular disturbance effects. Negligence of such effects can have an increasingly negative influence on the scientific data over time. The gained knowledge may identify potential to optimize attitude control customs, and further improve the quality of the gravity field model. This could be especially beneficial for GRACE Follow-On given the similarity of the two missions.

Routine analysis of GRACE telemetry revealed a striking behavior of the thrusters controlling the roll attitude of the satellites. The observation shows that the summed thruster on-times of one day, positive as well as negative, display a systematic variation over time. This phenomenon implicates a cyclic tilt of the satellite in alternating direction over a constant period of time, that can not be explained straight-forward.
The primary scope of this work is to determine the cause of this long-period effect and explain it in detail. For this purpose, all relevant disturbance effects that have an influence on the roll attitude need to be identified and modeled. A special focus is put on the investigation of magnetic disturbance effects in connection to the solar panels. Analysis on short and long time-scales

may provide qualitative as well as quantitative information regarding the behavior of the attitude error in roll in consequence of acting disturbance torques. A temporal change or variation of the effect, and possible differences between both GRACE satellites are considered.

1.3 Structure

To analyze the stated problem the work is subdivided in four parts:
In the first part (chapter 2) the main characteristics of the GRACE mission are presented. This includes basic design parameters, a view on the orbit, peculiarities in regard to mission operations, and an overview of the GRACE attitude and orbit control system (AOCS) comprising sensors and actuators.
In the second part (chapter 3) an overview of typical disturbance forces is given, pointing out the most relevant effects for GRACE w.r.t mission design and build. Detailed models of the solar radiation pressure and magnetic disturbances are worked out. The latter differentiates between a torque due to the satellite's magnetic dipole moment and a disturbance that is caused particularly by undesired effects within the solar panels.
The analysis of the individual disturbance forces is conducted in the third part (chapter 4). The effects are observed on a long time scale in the order of years and a short time scale in the order individual orbits. The results identify the main influences on the roll stability, give information about the existence of magnetic effects and the long-term stability of the satellites design.
In the fourth part (chapter 5) all results of the work are summarized. Conclusions drawn from the analysis are evaluated and put into perspective. Finally, proposals for future work are suggested.

2 The GRACE mission

2.1 Overview

The two identical GRACE satellites were launched on March 17, 2002, from Plesetsk Cosmodrome with a Russian Rockot launcher. The mission was initiated under the NASA Earth System Science Pathfinder Program with the objective to analyze and map the gravity field of Earth and its temporal variations. [4] The principal investigators of the mission are UTCSR (University of Texas, Center for Space Research) in the USA and GFZ (Geoforschungszentrum Potsdam) in Germany. Responsible for the development and operation of the payload is JPL (Jet Propulsion Laboratory). The GSOC (German Space Operation Center) handles satellite operations. At the time this work was done the planned mission duration of 5 years had been exceeded by more than 10 years. GRACE is the first mission ever to utilize an inter-satellite ranging system between two satellites. See Figure 2.1 for an artist's impression.

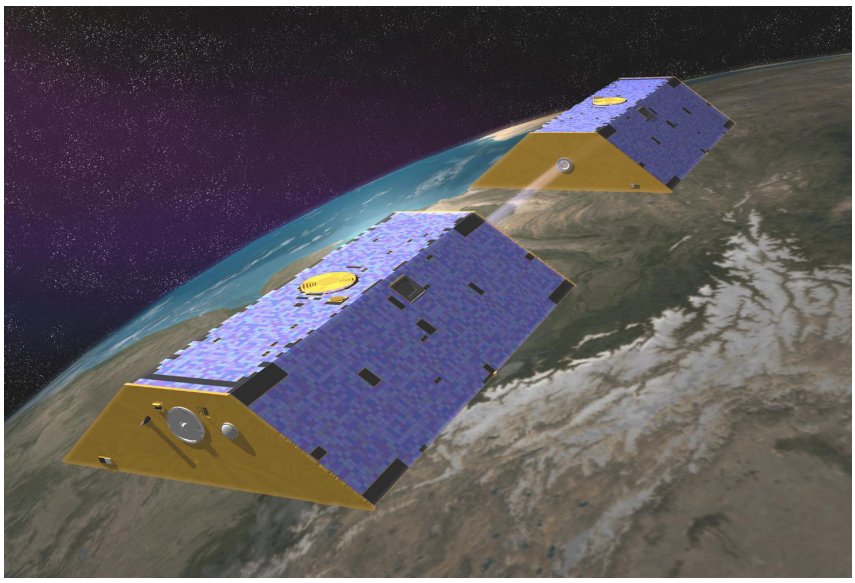

Fig. 2.1: Artist's impression of the two GRACE satellites in orbit [9].

The basic principle behind the modeling of the global gravity field can be explained in a few steps: Any fluctuation in the gravitational potential induces orbit perturbations. These are tracked consistently to create a global map of the gravity field. A combination of three key technologies is necessary for this purpose. Firstly, both GRACE satellites accommodate GPS receivers which are necessary for precise orbit determination. Secondly, measurement of the

relative distance is accomplished by a K-band antenna located on the front panel of both satellites. The antenna is part of an MWI (Microwave Instrument) whose accuracy is in the range of 1 μm [7]. This allows tracking of tiny variations in the inter-satellite distance caused by local fluctuations in the gravitational potential. Thirdly, highly accurate accelerometers are located at the center of gravity and are used to subtract non-gravitational disturbances from the total measurements. Data from consecutive measurements averaged over a period of months shows deviations from the static (long-term average) field, enabling analysis of temporal variations. Such changes indicate shift of mass within Earth caused by melting of ice, rise of sea levels or lowering of groundwater.

GRACE has successfully provided scientific data for more than 15 years. The data allowed scientists to create models of the gravity field more than an order of magnitude better when compared with previous missions [4]. However, effects of aging and failure of hardware components have complicated operations considerably in recent years [10]. Special measures are required all the time. Technical problems with the Star Trackers on both satellites require satellite swaps approximately every 160 days starting in 2014. Declining battery performance due to natural degradation and loss of battery cells required a multitude of operational measures to keep the satellites alive. For example, instruments have to be switched of for about 20 days around the longest eclipses. Fortunately, enough scientific data can be gathered to generate new gravity field models, despite all difficulties. A high interest exists within the scientific community to continue the mission as long as possible to maintain the availability of new data before the start of GRACE Follow-On [8].

2.2 Orbit

The satellites were injected into a nearly circular, polar orbit at an initial altitude of 490 km (Fig. 2.2). Over the course of the mission the distance from Earth has decreased to about 330 km (May 2017). The relative distance is set to 220$\pm$50 km. Alignment of the MWI towards each other requires a rotation of the leading satellite by 180 deg about the Z-axis (nadir direction). The orbit is characterized by a low eccentricity of < 0.002 and an high inclination of about 89 deg. The β' (read β *prime*) angle oscillates between $\pm$88 deg whereby the extrema may vary from cycle to cycle. Low β' imply long eclipses, whereas values < -70 deg or > 70 deg are orbits with continuous sunlight.
Another important feature of the GRACE orbit is a natural drift, which causes a slow progression of the RAAN (Right Ascension of the Ascending Node) with a period of 8 years. The satellites thus complete a period in an inertial frame within 321.6 days. In the context of this work this period is referred to as **cycle**. An overview of all cycles with corresponding dates, the effect of a changing β' angle and the principle of the orbit drift are illustrated in appendix A.1. The orbit design allows a new determination of the gravity field every 30 days explaining why the scientists publish monthly models.

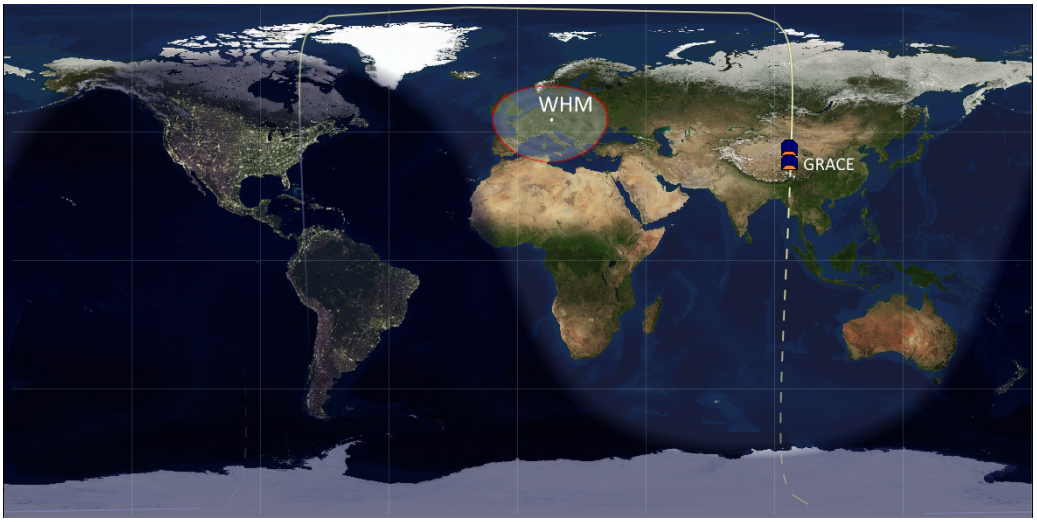

Fig. 2.2: Illustration of the ground track of the GRACE orbit and the ground station in Weilheim (WHM). (DLR internal image)

2.3 Attitude and Orbit Control System

The AOCS (Attitude and Orbit Control System) consists of sensors, actuators, and control and command functions implemented in the OBC (On-Board Computer). The choice of sensors, actuators and implementation is tailored for each satellite to meet the mission's objective. In the case of GRACE the AOCS ensures 3-axis stabilization. Any orientation can be commanded if necessary. Remarkably, the GRACE satellites are the payload themselves as they are mass probed by the gravity field. To guarantee the exchange of the K-band signal a relative pitch bias of -1 deg has to be maintained constantly.

AOCS sensors determine the satellite's location, trajectory and orientation. The sensitivity varies between high precision sensors such as star cameras (0.001 deg) and those with limited accuracy such as Coarse Earth and Sun Sensors (10 deg) [11]. A very high sensor accuracy is not always necessary. The sensitivity of coarse sensors is sufficient in certain cases, e.g. for ensuring a stable attitude in Save Mode, or is accepted in favor of a smaller mass and lower costs. To complement the robust coarse sensors, highly accurate attitude sensors are also mounted on the satellite. Yet, their operational range is typically limited to, e.g., low rotation rates of the satellite. In this case coarse sensors are used to stabilize the attitude, before fine pointing can be attained.

Actuators compensate deviations from nominal flight conditions induced by disturbance forces, realign the satellite when a mode switch is required, initiate corrective orbit maneuvers and, in rare cases, evasive maneuvers. Different types of actuators include internal and external actuators. External actuators distinguish between those that consume a limited resource (fuel) and those that use electric energy. Table 2.1 summarizes all attitude sensors and actuator used on GRACE.

Sensor / Actuator	Function
CESS	Coarse Earth and Sun Sensor. Basic attitude sensor with low accuracy compared to other sensors. Determines attitude relative to Earth and Sun based on temperature variations due to the respective illumination.
Magnetometer	Determination of attitude based on local terrestrial magnetic field vector.
SCA	Star Camera Assembly. High accuracy attitude sensor used for fine pointing. Imagery of surrounding stars is compared to on-board star catalouge.
IMU	Inertial Measurement Unit. Inertial rates computed from angular increments.
ATH	Attitude Thrusters. Two branches à 6 10 mN thrusters used for precise attitude control about all axes.
OTH	Orbit Thrusters. Two 40 mN thrusters for orbit control located on the rear panel of both satellites.
MTQ	Magnetic Torque Rods. Regulated currents are sent through coils. The resulting dipole moment interacts with the magnetic field.
COM Trim Assembly	Center-of-Mass Trim Assembly. Balancing of COM shift caused by uneven fuel mass in tanks. The control is achieved by movement of a balance mass.

Table 2.1: Overview of all attitude sensors and actuators comprised by the GRACE AOCS.

Mode switches are commanded when the task of the satellite changes or attitude is lost. An overview of all operational modes is provided in table 2.2. In scope of this work it is assumed that the satellites are in Science Mode 100% of the time (the mission average is about 94% [12]). An overview of all sensors and actuators relevant for this work is given in the section below.

2.3.1 Sensors

Coarse Earth and Sun Sensor (CESS)

The CESS determine the attitude of the satellite relative to the Earth and the Sun. It is a typical low-cost, low-accuracy sensor used in Earth observation missions. The accuracy is 5 deg – 10 deg for the Earth vector and 3 deg – 6 deg for the Sun vector, respectively [13]. The

Mode		Function
Science Mode	SM	Payload operational, collection of scientific data. GRACE operates in Science Mode 94% of the time.
Coarse Pointing Mode #1	CICPM	Rate damping and step-wise attitude acquirement with three sub-modes. Uses Inertial Measurement Unit (IMU).
Coarse Pointing Mode #2	CMCPM	See CICPM. In case of IMU failure the magnetometer is used.
Emergency Rate Damping	ERDM	Damp rotation rate below 10 mrad/s using Magnetometer and MTQ.
Attitude Hold Mode	AHM	Hold specified 3-axis attitude relative to orbit frame.
Back Up AHM	BAHM	After failure of one Star Camera, hold AHM attitude by integrating through Sun blinding of remaining camera.
Back Up SM	BSM	After failure of one Star Camera, hold SM attitude by integrating through Sun blinding of remaining camera.

Table 2.2: Overview of all operational flight modes in scope of the GRACE mission. Depending on the current objective a new mode can be commanded by the on-board computer and attained by the AOCS.

system comprises six identical sensors. The sensor heads (Fig. 2.3) are positioned such that the normals of two sensor head planes align with the GRACE body frame axes, pointing in opposite directions. Each head owns two segments of different coating materials with precisely known absorption properties in visible and infrared light spectra. The functional principle is based on temperature measurement by PT1000-resistors. The six heads register different temperatures depending on the current orientation of the satellite. The difference in temperature causes a change of the resistance within the resistors and a voltage drop that is measured by the on-board computer. During eclipse the Sun is not visible and the sensor returns zero. At the beginning of every new Sun phase the CESS require a calibration time of about 60 s that may falsify the returned values. An anomalous behavior of the solar vector data was noticed around phases with $\beta' = 0$. The plots displays an unchanged progressing for more than one week, despite a changing β'. This problem will be further addressed in chapter 4.

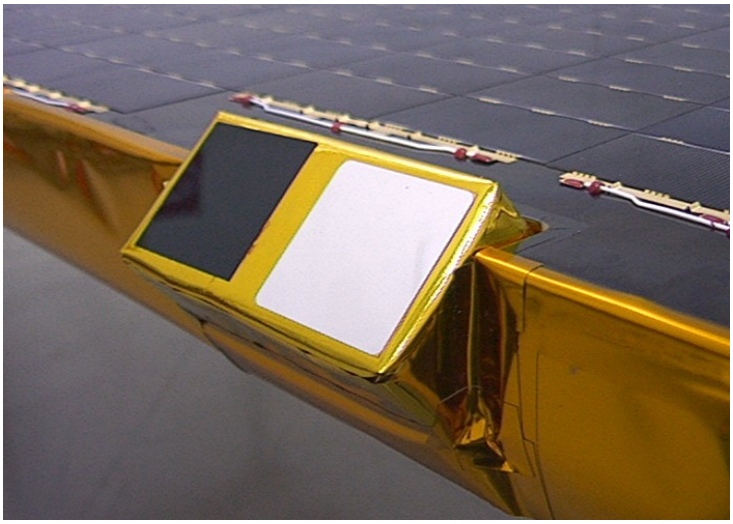

Fig. 2.3: Coarse Earth and Sun Sensors on GRACE. The system accommodates six sensors in total. The plane normals are aligned with the axes of the satellite body frame.[12]

Magnetometer

A magnetometer measures the direction and strength of the terrestrial magnetic field vector $\vec{\mathbf{B}}_{MM}$ at the satellite's position. The information is then processed by the AOCS to determine the necessary currents for the magnetic torque rods (see. section 2.3.2). GRACE accomodates a lightweight Fluxgate Magnetometer located on top of a boom on the nadir panel. The sensor consists of a ferromagnetic core material surrounded by a coil, plus harness. A magnetic flux is produced inside the core by the local magnetic field. The permeability of the core is designed to decrease when the material is saturated. This change induces a current inside the coil which is converted into information on the magnetic field. Applying this principle for all three axes yields the magnetic field vector and its strength. [14] Interference of satellite generated magnetic fields need to be considered as it may lead to wrong measurements. The disturbing magnetic field typically created by the satellite can be determined prior to the launch. This allows subtracting the error from the magnetometer measurements during the mission. Within GRACE the main source of magnetic disturbances are the MTQ.

In early mission years, the magnetometer data was used in conjunction with data taken from an IGRF magnetic field model stored on board to determine the magnetic field vector $\vec{\mathbf{B}}_{est}$ in body coordinates. This was done mainly to account for the error in the magnetometer measurements induced by the magnetic field of the MTQ. The International Geomagnetic Reference Field, short IGRF, is a mathematical description of Earth's magnetic field, published and updated regularly by the IAGA (International Association of Geomagnetism and Aeronomy) [15]. Input to the model are the satellite's location and velocity that are provided by the GPS. The resulting field vector $\vec{\mathbf{B}}_{IGRF}$ is determined in the WGS-84 frame, an Earth Centered, Earth Fixed frame [16]. Prior to calculation of $\vec{\mathbf{B}}_{est}$ both, magnetometer and IGRF data, are converted into the satellite body frame [12]. The weighting of magnetometer and model values was changed

during the first years of the mission. Since 2006 $\vec{\mathbf{B}}_{est}$ is derived solely from the magnetometer measurements corrected for an estimated error.

Star Cameras

Star cameras, also referred to as Star Trackers, are optical attitude sensors used in satellite missions that require stable pointing. The accuracy of up to 0.001 deg [11] surpasses that of all other sensor types. In terms of GRACE this level of precision is crucial for the inter-satellite ranging that largely influences the quality of the recovered gravity field data. GRACE is designed with two Star Cameras on each satellite, embedded within the side panels.
As the name suggests, the camera takes an image of the stars in its field of view. The position and brightness of the visible stars are analyzed and compared to the data from an on-board star catalog [17]. Each star is represented by just a small number of pixels. A high sensitivity of the camera is required to identify the respective stars correctly. In consequence star cameras are easily blinded by bright sources of light such as the Sun or the Moon. The placement of the cameras on GRACE does not prevent simultaneous blinding of both cameras during phases with small β' angles. In case of blinding the trajectory is derived from calculation until one camera is functional.

Technical difficulties and a limited power availability do not allow proper usage of the star cameras. Since 2014 only one camera is operational on both satellites (Left camera on GRACE 1 and right camera on GRACE 2). This poses a delicate issue for further mission success as precise pointing is crucial for the measurement of the gravity field. Phases with high β' in which the single operational camera is directed towards the Sun make usage impossible. Thanks to the rotation of the satellites by 180 deg relative to each the two operational cameras always point in one direction. This fact allowed the avoidance of severe problems by performing swaps of the leading and following satellite, and directing the operational side towards deep space. Since July 2014 swaps are performed ca. every 160 days. This knowledge is relevant in regard to the analysis of long-period effects in chapter 4.

2.3.2 Actuators

Magnetic Torque Rods

The Magnetic Torque Rods (MTQ) are the primary means of attitude control for GRACE as they use regenerative, electric energy. GRACE utilizes MT30-2 magnetic torque rods manufactured by ZARM (Center of Applied Science Technology and Microgravity). The basic idea of the MTQ is to create a reaction torque $\vec{\mathbf{T}}$ on the satellite by generating a magnetic dipole moment $\vec{\mathbf{m}}$ within an external magnetic field $\vec{\mathbf{B}}$. The torque can be calculated by equation 2.1.

$$\vec{T} = \vec{m} \times \vec{B} \tag{2.1}$$

Similar to the magnetometer, MTQ generate a dipole moment $\vec{\mathbf{m}}$ using a magnetic core material surrounded by two coaxial coils. The coils are galvanically isolated from one another. Each coil consists of a fixed number of parallel windings **n** each of which encloses an area **A**. A dipole moment $\vec{\mathbf{m}}$ is induced when a current is sent through the coil. The direction of $\vec{\mathbf{m}}$ is parallel to the plane normal of the cross-section area **A**; its sign is determined by the right hand rule: the thumb of the right hand indicates the direction of $\vec{\mathbf{m}}$ when the remaining fingers are curved along the flow direction of the current. The size of the components can be controlled by adjusting the size of the current **i**. Equation 2.1 can be written in the form 2.2, if the orientation of the enclosed area **A**, the current **i**, and the number of loops **n** are known.

$$\vec{T} = i\vec{A}n \times \vec{B} \tag{2.2}$$

The MT30-2 comprises three such components, each aligned with one axis of the satellite body frame. Superposition of three $\vec{\mathbf{m}}$-components thus allows precise 3-axis attitude control. A major constraint is the limited control authority of the magnetic torque rods in some locations of the orbit. At the equator the magnetic field has the approximate form $B = (B_x, 0, 0)^T$ (in body coordinates). Equation 2.1 yields $\vec{T}_x = 0$ such that no torque about the X-axis can be applied. This requires activation of the attitude thrusters to maintain control. The main MTQ performance parameters are listed in table 2.3.

Characteristics	Value / Unit
Minimum Linear Momentum Range	$\pm 30\,Am^2$
Maximum Residual Momentum at zero input Current	$\pm 0.2\,Am^2$
Maximum deviance from linear characteristics	$\pm 0.3\,Am^2$
Maximum current range for Momentum specified above	$\pm 120\,mA$
Quantization of coil currents	$2\,mA$
Maximum currents in failure case	$\pm 160\,mA$

Table 2.3: Overview of relevant characteristics of the GRACE magnetic torque rods type MT30-2.

Cold Gas Assembly

GRACE utilizes a pressure fed system of 14 thrusters as means of orbit and complementary attitude control. Orbit control is realized by two 40 mN thrusters located on the front panels. Twelve 10 mN attitude thrusters (ATH), separated in two branches, are used for attitude control. The branches are used simultaneously, which means that one pair of thrusters is used per axis and per direction of rotation. Both branches can be isolated in case of failure. The system uses gaseous nitrogen (GN2) stored in two tanks that are mounted close to the satellite's center of mass (COM). A small mass with an adjustable position is integrated to balance out COM shift produced by uneven fuel consumption. Relevant characteristics of the ATH are summarized in table 2.4. The nominal torque values listed in the table include the respective levers of the

thrusters relative to the center of gravity. An overview of the position of all attitude thrusters is provided in appendix A.1.

Characteristics	Value / Unit
Nominal torque about X-axis (pitch)	$2 \times \pm 0.0145$ Nm
Nominal torque about Y-axis (roll)	$2 \times \pm 0.003$ Nm
Nominal torque about Z-axis (yaw)	$2 \times \pm 0.0072$ Nm
Minimum activation time (quantization)	30 ms (1 ms)
Minimum number of actuations per thruster	10^6
Total GN2 fuel mass at BOL*	35 kg

Table 2.4: Overview of relevant characteristics of the GRACE attitude thrusters [12]. *Beginning of life.

Thruster actuation is commanded by the Pulse Width Modulator discussed below. Availability of the ATH is essential for a stable attitude during orbit phases where MTQ control is limited. The total number of thruster activations has exceeded the minimum life expectancy of 10^6 activations in yaw and roll. Fuel usage has been trimmed down to <5 g per day to extend the possible mission duration [12]. The increased number of technical problems in recent mission years demanded a higher consumption. At the time this work is conducted GRACE 2 has about 3 kg of fuel left, GRACE 1 has ca. 7 kg. The exhaustion of fuel reserves is one of the issues limiting the possible continuation of the mission.

2.3.3 Pulse Width Modulator Error

The Pulse Width Modulator is a part of the GRACE AOCS software responsible for the control of thruster activation. Input is a parameter named *Pulse Width Modulator Error*. This error is a combination of an attitude error [mrad] and rate error [mrad/s], and the primary indicator of the attitude on GRACE. Understanding of this parameter is highly important for further analysis of disturbance effects.
The simplified structure of the AOCS control circuit is shown in Figure 2.4. Inputs to determine the Pulse Width Modulator Error are the desired attitude, AOCS sensor data and the actuator torques calculated for the previous time step. The Error is then processed by the Pulse Width Modulator (denoted by PWM only in this scheme) and the Science Magnetic Control (SMC). Output are the required torques $\vec{T}_{ATH}$ and $\vec{T}_{MTQ}$ for the next time step.

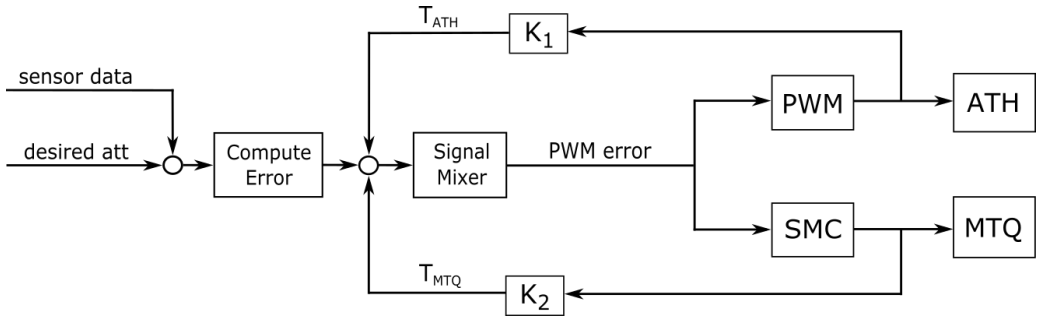

Fig. 2.4: Simplified scheme of the GRACE AOCS control circuit. AOCS sensor data, information on the desired attitude, and the actuator torques from the previous time step are used to determine thruster pulses and MTQ currents for the new time step. All abbreviations are explained in the text and the glossary.

The Pulse Width Modulator Error will be referred to as PWM from here on. The X-component of the three dimensional PWM vector reflects the attitude about the X-axis (roll) and so forth. PWM data of one day is exemplified in Figure 2.5. It is recognizable from the plot that in roll the range of tolerance or dead band is set to -0.003 < PWM < +0.003. The Pulse Width Modulator typically operates in an *adaptive mode*, which commands additional and/or longer thruster pulses the closer the error gets to either boundary [12]. The interpretation of the PWM

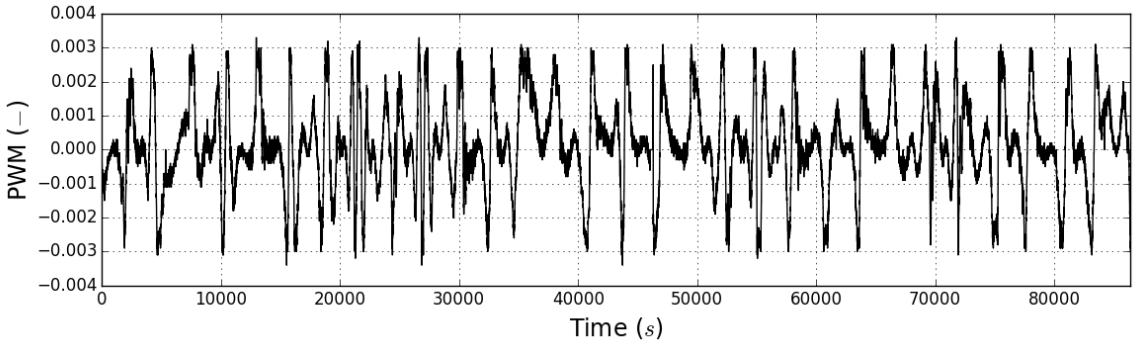

Fig. 2.5: Example of PWM telemetry of MET 3273. The dead bands for the roll attitude are set to ±0.003.

data with respect to disturbance forces is complicated by the following factors:

- Combination of several different units
- Influence of AOCS actuator torques
- Influence of stochastic disturbances, maneuvers etc.
- Available information on the software architecture

The latter denotes two different aspects. Firstly, no documentation is available regarding the formation of the PWM from attitude and rate errors. Secondly, the exact structure of the control circuit shown above is unknown. A parameter KMAG is used by satellite operators to switch between MTQ-dominated and ATH-dominated attitude control. Low values of KMAG used during most of the mission indicate a weighting towards more ATH performance. At this point it is not fully evident, whether the *desired* MTQ currents taken from the telemetry are equal to the effectively commanded currents. A possibility exists that KMAG affects the desired values before a torque is exerted. It is worth mentioning that in line with past disclosure regulations the software was first coded in the United States, then documented, then re-coded in Europe based on the documentation. Naturally, the software functionality has been validated, information on the exact implementation is not available, though.

3 Disturbance models

3.1 Overview of typical disturbance forces on satellites

There are several external forces that influence the attitude of a satellite. The effects of these must be counteracted in order to maintain the desired pointing accuracy. The main forces and respective torques acting on a satellite in low-earth orbit are:

- Gravity gradient [$1 \cdot 10^{-5}$ Nm]
- Solar radiation pressure [$1 \cdot 10^{-6}$ Nm]
- Magnetic torques [$1 \cdot 10^{-5}$ Nm]
- Air drag [$1 \cdot 10^{-7}$ Nm]

Note, that the listed orders of magnitude are exemplary and differ slightly on every satellite. Other disturbances, e.g. re-radiation from the Earth, Albedo, or solar wind, can typically be neglected as they are comparatively small.[18]
Further, a satellite can also have internal effects that may influence its attitude. They include torques induced by moving parts and mechanisms (antennas, solar arrays, booms, etc.), propellant slosh inside the tanks, misalignment of thrusters and reaction wheels or out-gassing. None of these apply to GRACE. The more accurate the model for attitude or orbit propagation has to be, the more effects have to be included in the simulation which in turn increases the required computational capacities. The exact torques differ considerably for each satellite and depend among others upon build and orbital height. Atmospheric drag is highest in very low orbits due to the density of the atmosphere, which drops exponentially with increasing height. The magnetic and gravitational effects influence the satellite in all altitudes up to geostationary orbits. The solar radiation pressure (SRP) is nearly constant for all altitudes given the small changes in orbital altitude compared to the distance of 1 AU between Sun and Earth. It becomes more important as the altitude grows. In interplanetary flight SRP is the main acting disturbance force [11].
Any disturbance force typically affects all three axes. However, the simple geometry of the GRACE satellites allows making some simplifying assumptions:

- Secondary effects such as the gravitational forces of other bodies are neglected.
- The atmospheric drag does not produce a torque for a symmetric front surface. The required pitch bias of -1 deg needed for the satellites' correct orientation towards each other causes a pitch torque. The roll and yaw motion stay unaffected during Science Mode.

- A constant, homogeneous distribution is assumed for all types of radiation. Considering that the normal of the bottom panel is always nadir pointing, the Earth's radiation pressure does not apply a torque as the force vector points towards the center of gravity and has no lever. The SRP affects all three axes; it is most interesting for the analysis of the observed long period roll effect and will be explained in more detail in chapter 3.2.

- The properties of the magnetic disturbance are hard to predict or specify. A magnetic torque is generated whenever currents inside the bus interact with a magnetic field. Current loops within the electronic sub-system induce a magnetic dipole moment vector that tries to align with the vector of the magnetic field [18]. This effect is used by the magnetic torque rods for attitude control. At the same time, undesired effects that can't be avoided completely in practice, cause attitude perturbations. The description and quantization of magnetic effects stands in the center of this work and will be analyzed in more depth in chapter 3.3.

3.2 Solar radiation pressure model

The solar radiation pressure is based on the momentum of photons. During interaction with other particles energy and momentum can be transferred between the particles. Energy and momentum are conserved quantities that can't be lost, only transformed. The relation between these two properties is

$$E = pc \tag{3.1}$$

where **E** is the energy, **p** is the momentum and **c** the speed of light. The energy can be formulated as

$$dE = S_0 A dt \tag{3.2}$$

with the Solar Constant $S_0 = 1366\ W/m^2$ [18], the area **A** and the time **t**. The momentum is

$$dp = \frac{S_0 A dt}{c}. \tag{3.3}$$

The radiation pressure **P** is calculated considering that the force **F** is the first derivative of the momentum:

$$F = \frac{P}{A} = \frac{dp}{dt}. \tag{3.4}$$

This yields

$$P = \frac{dp}{Adt} = \frac{S_0}{c} = 4.563 \cdot 10^{-6} \frac{N}{m^2}. \tag{3.5}$$

The SRP comprises two components. One part of the radiation hitting a surface is absorbed while the other part is reflected. How much radiation is reflected and how much is absorbed depends on the respective coefficients ε and $1-\varepsilon$. Their sum always equals one. The properties of the surface material determine the coefficients. Note that the amount of radiation absorbed is highly important for the thermal control of a spacecraft. An average reflectivity coefficient ε = 0.35 was measured for the solar panels. Both principles are shown in Figure 3.1. Figure 3.1b

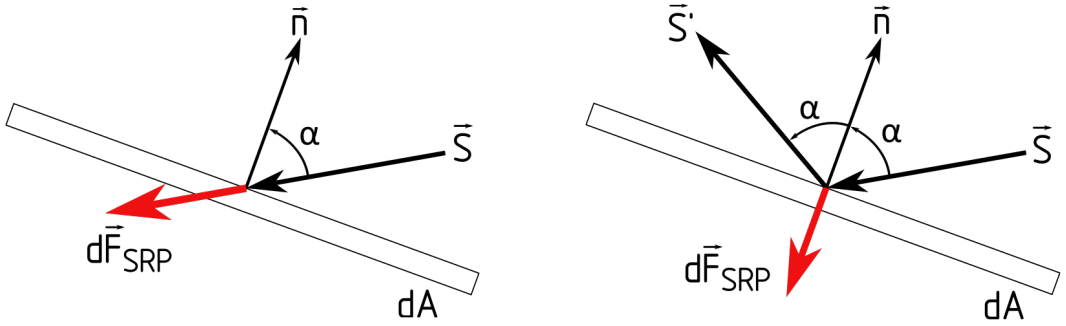

(a) Illustration of perfect light absorption ($\varepsilon = 0$). The incident radiation absorbed by the surface A creates a force $\vec{F}_{SRP}$ parallel to the incident light vector $\vec{S}$.

(b) Illustration of perfect, specular light reflection ($\varepsilon = 1$). Even surfaces reflect radiation under the same angle α the indicdent vector $\vec{S}$ encloses with the plane normal $\vec{n}$. Reflected light creates a force in the opposite direction on $\vec{n}$.

Fig. 3.1: Principle of light absorption and reflection

illustrates that reflection distinguishes between specular reflection ε_r and diffuse reflection ε_d. Rough surfaces reflect the light diffusely (in all directions). Perfectly even surfaces reflect the light under the same angle α that the incident ray forms with the plane normal. The sketch also shows that while absorbed light creates a force in the direction of the incident ray (3.1a), the force vector of the reflected light is strictly parallel to the plane normal. According to Newton's Second Law the surface experiences a force when it is hit by photons; according to the Third Law, another force acts upon the surface when the light is reflected. This results in a factor 2 for the force induced by reflected light. For absorption and diffuse as well as specular reflection the resulting force is then given by equation 3.6 [19].

$$\vec{F} = -PA\cos\alpha\left[\left((1-\varepsilon)+\varepsilon_d\right)\vec{S}+\frac{2}{3}\vec{n}+2\varepsilon_r\cos\alpha\vec{n}\right]. \tag{3.6}$$

A last term completes the equation under the assumption that absorbed radiation is re-radiated immediately (Lambert's Law [20]):

$$\vec{F} = -PA\cos\alpha\left[\frac{2}{3}(1-\varepsilon)\vec{n}\right]. \tag{3.7}$$

The total force induced by the solar radiation is then

$$\vec{F} = -PA\cos\alpha\left[\left((1-\varepsilon)+\varepsilon_d\right)(\vec{S}+\frac{2}{3}\vec{n})+2\varepsilon_r\cos\alpha\vec{n}.\right] \tag{3.8}$$

Factor $A\cos\alpha$ accounts for the projected area that is perpendicular to the incident light, $\vec{\mathbf{S}}$ is the vector of the incident Sun, $\vec{\mathbf{n}}$ is the plane normal. All vectors are formulated in the satellite body frame. The angle of incidence can be expressed as $\cos\alpha = \vec{S}\cdot\vec{n}$. The fraction of diffusely reflected light is neglected and the equation can be simplified to

$$\vec{F} = -PA\cos\alpha\left[(1-\varepsilon)\,\vec{S} + 2\,\varepsilon_r\cos\alpha\,\vec{n}\right]. \tag{3.9}$$

The generated torque $\vec{\mathbf{T}}$ can be acquired via equation 3.10 from the cross product of momentum lever $\vec{\mathbf{r}}$ and force $\vec{\mathbf{F}}$:

$$\vec{T} = \vec{r}\times\vec{F} = -PA\cos\alpha\left[\vec{r}\times\left((1-\varepsilon)\,\vec{S} + 2\,\varepsilon_r\cos\alpha\,\vec{n}\right)\right] \tag{3.10}$$

Equation 3.10 allows building a model that calculates the SRP torque on GRACE. Modeling is done using a python script. Satellite telemetry is available for the whole mission, hence, no further modeling of the orbit is necessary.
The geometric parameters can be taken from the sketch in Figure 3.2. As may be recognized from the sketch, the torques point of application is in the middle of each panel. Minor asymmetries of the surface are neglected. In Science Mode the bottom panel is pointed at Earth and does not contribute to the torque.

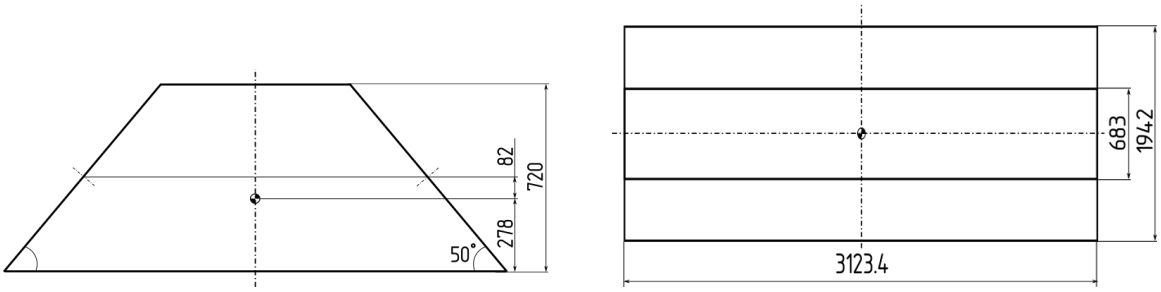

(a) Front view (b) Top view

Fig. 3.2: Overview of geometric parameters of the GRACE satellite bus. Values in mm.

GRACE follows a near polar orbit with constantly changing β' angle and eclipse duration. The momentary eclipse duration is different for each panel and is calculated for each side individually. For this purpose a rotation is done from the satellite body frame $\vec{K}_b$ into the respective panel frames $\vec{K}_i$ about the angle γ_i.

$$\vec{K}_i = C\,\vec{K}_b \tag{3.11}$$

A 2D-rotation is sufficient as the X-axis stays the same for all frames. The respective rotation matrix $\mathbf{C}$ is

$$C = \begin{pmatrix} 1 & 0 & 0 \\ 0 & \cos\gamma_i & \sin\gamma_i \\ 0 & -\sin\gamma_i & \cos\gamma_i \end{pmatrix} \tag{3.12}$$

The principle is illustrated in Figure 3.3. The transformation is done such that the Y-axes of

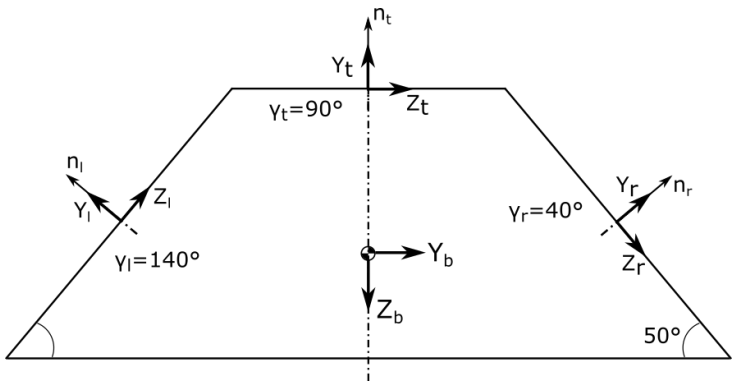

Fig. 3.3: Illustration of the coordinate frame transformation from GRACE body coordinates into the panel centered frames. The X-axis remains the same for all frames. The subscripts denote the left (l), top (t) and right (r) panel, γ is the angle of rotation.

the local frames are parallel to the panel normals. To check whether the panel is in the Sun or in eclipse the algorithm monitors the Y-component of the transformed Sun vector. A positive value means illumination from above; a negative value means that the Sun vector points to the back side of the panel which is equivalent to an eclipse. In the latter case the torque is set to zero, otherwise equation 3.9 is used to calculate the force. The resulting three force vectors are then rotated back into the satellite body frame and the X, Y and Z components are summed. In a final step the torque is calculated using the lever $\vec{\mathbf{r}}$ in body coordinates and equation 3.10.

The resulting torque about the X-axis is visualized in Figure 3.4. Figure 3.4a shows a scenario with $\beta' = 0$ deg. During this phase the satellites experience the longest eclipses and a symmetric illumination of the satellite. In roll and yaw the torques fluctuate about zero during Sun phases. The trend slowly shifts from negative to positive values as β' changes its sign. The pitch torque shows a consistent progression from positive to negative with a zero crossing each time the Sun is in zenith. All values are in the order of 10^{-6} Nm to 10^{-7} Nm. Figure 3.4b exemplifies a phase with a large β'. This period is characterized by a nearly Sun synchronous orbit with short eclipses and a one sided illumination of the satellite. In the shown case the maximal beta angle is -88 deg. The orbit is not perfectly Sun synchronous due to the tilt of 23 deg between ecliptic and equator. In pitch a similar pattern is visible, but with values one order of magnitude smaller compared to yaw and roll. The yaw torque follows a sine-shaped curve with a zero crossing at the point closest to the Sun. The roll torque is induced by one side panel and has therefore consistently positive values (negative for a positive β') during light phases. The anomaly at ca. 1000 min may be due to a stochastic attitude perturbation. Relatively long eclipses of about 20 minutes were noticed during modeling, despite a very high β'. The observation was attributed to the CESS measurements which are set to zero (full eclipse) even during penumbra phases. In all other aspects the graphs comply with expectations. The structure of the SRP model is summarized in the flow chart in Figure 3.5.

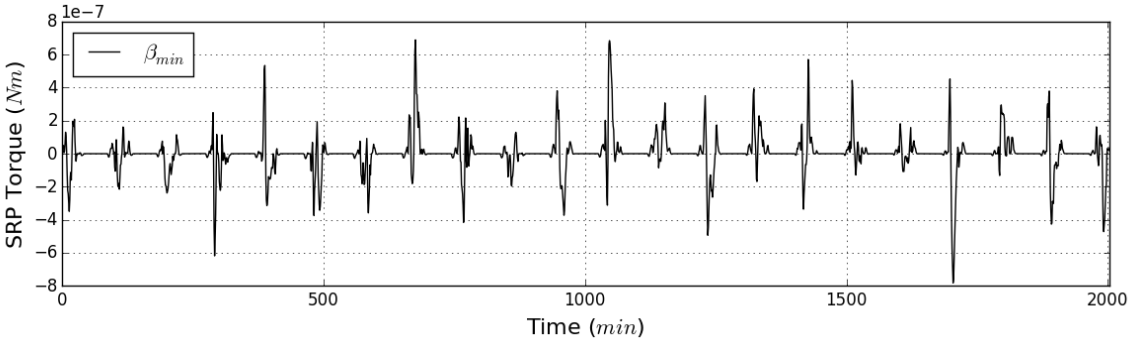

(a) Modeled SRP torque about X for $\beta' = 0$ deg (MET 3212). The forces on the panels are balanced out. The phase is characterized by long eclipses.

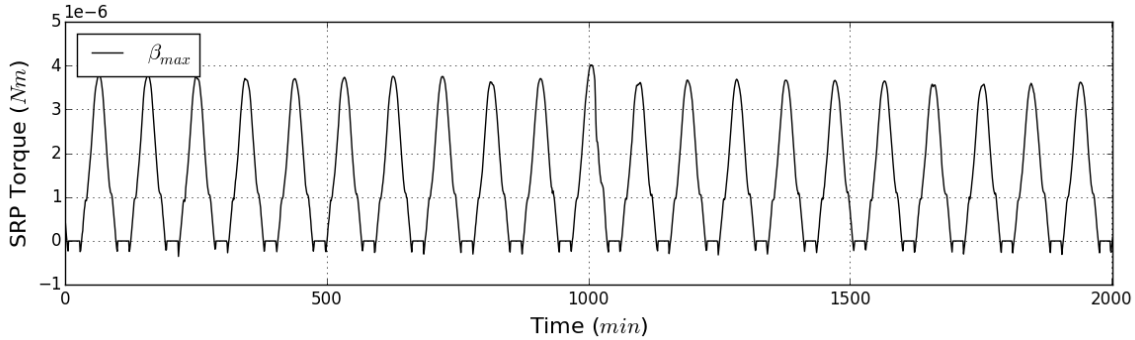

(b) Modeled SRP torque about X for $\beta' = -88$ deg (MET 3272). Illumination of just one side panel yields a torque with (here) continuously positive or negative values depending on the sign of β'.

Fig. 3.4: Illustration of the modeled SRP torque on GRACE 1 for phases with a low and a high β'.

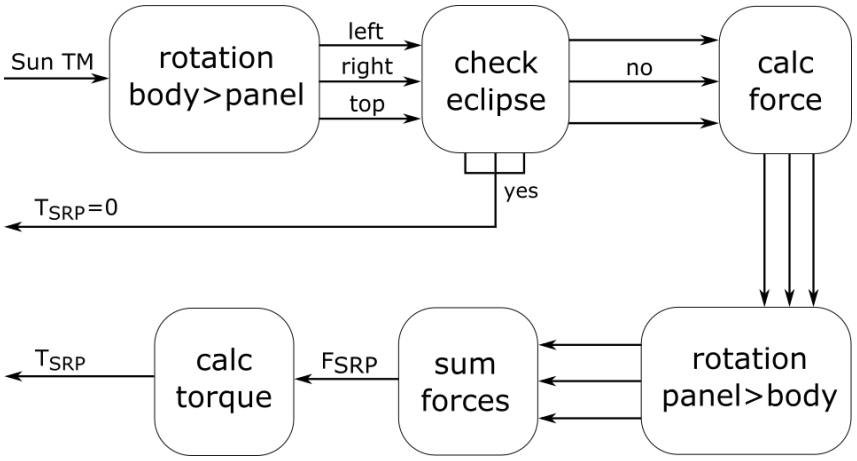

Fig. 3.5: Overview of the model structure of the solar pressure induced disturbance torque.

3.3 Magnetic disturbance model

3.3.1 Magnetic dipole moment

The liquid iron core of the Earth works like a large dynamo creating a magnetic field around the planet. The field is large enough to be relevant for space flight. Any interaction with a satellite's residual magnetic dipole moment (RDM) generates a torque that has an influence on the attitude. Magnetic torque rods use this effect for attitude control with a regulated current output; equally, parts of the satellites power harness can induce undesired magnetic disturbances. To reduce any sort of interaction as far as technically possible the wiring is coated with 25×0.3 mm aluminum foil. An example of the insulation of the GRACE PCDU (Power Conditioning and Distribution Unit), OBDH (On-board Data Handling), and adjacent harness is shown in Figure 3.6. Satellites

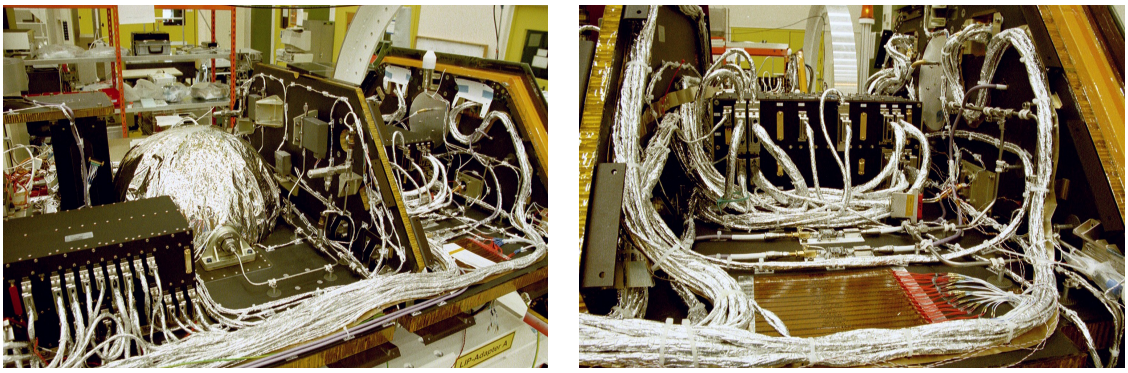

(a) Insulation at PCDU. (b) Insulation at OBDH.

Fig. 3.6: Example of the insulation of the power harness rails inside the GRACE bus [12].

have a typical RDM of $0.1 - 20\ Am^2$ [18]. In individual cases values can become higher, for example due to special instruments with a high power demand. A maximum RDM of $5\ Am^2$ was specified for GRACE for a maximum nominal power consumption of $136.7\,W$ [21].

The torque $\vec{\mathbf{T}}$ induced by the magnetic dipole moment $\vec{\mathbf{m}}$ and the terrestrial magnetic field $\vec{\mathbf{B}}$ is determined by equation 2.1. It is further referred to as *RDM Torque*. Acquiring information on the RDM of the satellite bus is fairly difficult. The structure of the power harness is designed to prevent the formation of wiring loops that contribute to the components of $\vec{m}$. The total RDM can be further reduced by the formation of loops with reversed direction of flow in which case the contributions cancel each other out. An overview of the arrangement and potential flow direction of the rails of the power harness is illustrated in Figure 3.7. Extensive knowledge of the hardware design and processes is necessary to design an accurate model of the RDM. However, an exact model is not of much interest with regard to mission operations. In scope of this work the focus is set on characterization of the RDM as a whole, weighting of the individual components of the vector, and estimation of its order of magnitude. A simplified model is sufficient for this estimation. It is assumed that:

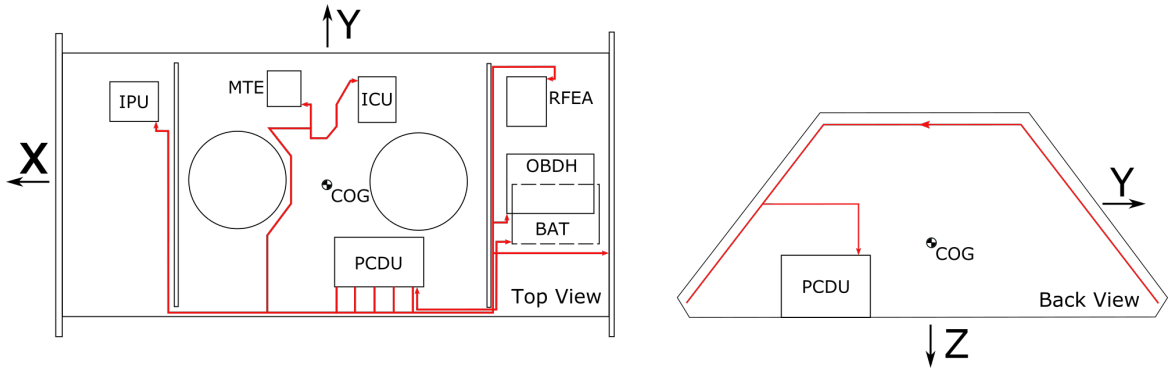

Fig. 3.7: Overview of the power harness structure on the GRACE bottom panel (left) and along the side and top panels (right).

- In phases with $\beta' > 0$ only the left panel contributes to the RDM. The sign of the contribution by the panel changes with every zero crossing of β'.
- The direction of flow within the harness is constant. Any RDM component that is not influenced by the side panels has a constant sign.
- Eclipses are neglected.
- The asymmetric design of the satellite interior may cause an asymmetric RDM, depending on which side panel is currently illuminated.

The progression of the torque depends strongly on the components of the RDM. At this point no information is available. Some examples of the roll torque with different weightings are provided in Figure 3.8. In all plots one period represents one orbit. The magnetic torque is further analyzed in chapter 4.

3.3.2 Solar panel induced disturbance

In the forefront of this work a magnetic disturbance was suggested that is caused specifically by the solar panels (SP). SP can induce magnetic effects in two ways - through the magnetization of ferromagnetic materials and through interactions coming from the wiring, especially the current loops typically used in the cells.[22]

The panels on GRACE were designed by GLOBALSTAR and carry Silicon cells, type 2PR/200. The arrays have a total size of 3120×969 mm (side) and 3120×691 mm (top). The side arrays comprise 11 strings à 86 cells, the top arrays 7 strings à 86 cells. All panels consist of a 20 mm CFRP and aluminum honeycomb sandwich structure, a 37 mm layer of foam, a 1 mm CFRP sheet and a 125 μm insulating Kapton layer. The cells ($65 \times 40 \times 2$ mm) are mounted on top of the Kapton. The inter-connectors of the cells are made of gold. The layering is shown in Figure 3.9. The choice of materials can be ruled out as cause of magnetic effects, as none of the above components have ferromagnetic properties.[12]

In the simplest case every cell holds a current loop (wire) and all currents have the same sense

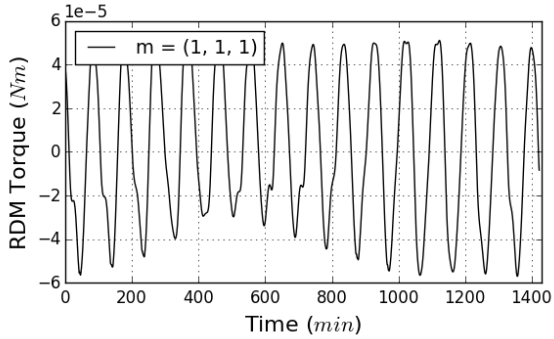

(a) RDM torque for $\vec{m} = (1,1,1)^T\, Am^2$.

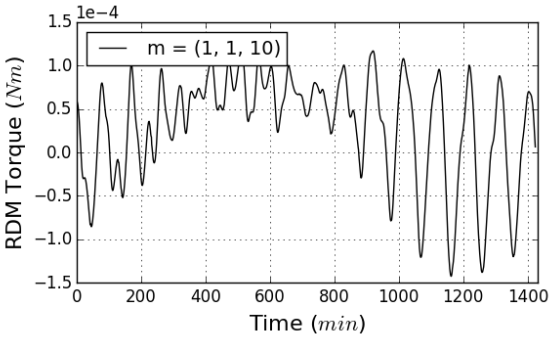

(b) RDM torque for $\vec{m} = (1,1,10)^T\, Am^2$.

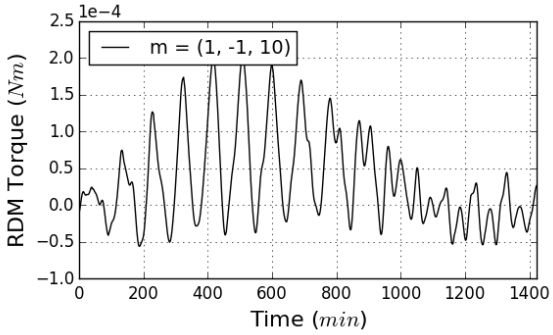

(c) RDM torque for $\vec{m} = (1,-1,10)^T\, Am^2$.

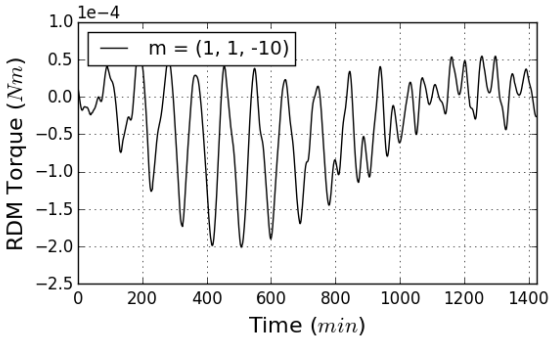

(d) RDM torque for $\vec{m} = (1,1,-10)^T\, Am^2$.

Fig. 3.8: Illustration of the modeled RDM torque about the X-axis for different possible weightings of the magnetic dipole moment $\vec{m}$.

of direction. Following equation 2.1 and neglecting the rest of the harness, one side panel alone with 946 cells, a cell area of 26 cm^2 and an average current at maximal power of 1 A could generate a dipole moment of roughly 0.025 Am^2. At a magnetic pole with an estimated $\vec{B}_{pole} = (0,0,45)^T \mu$T this yields a torque $T_{pole} = 9 \cdot 10^{-7}$ Nm which is in the range of other typical perturbations. Different technical solutions and wiring techniques exist to avoid large disturbances of this kind. Possible measures are [22]:

- The flow direction inside neighboring loops is reversed
- The flow direction inside the loops is opposed to that inside the harness on the back side of the array structure
- The wires are twisted to partially cancel out each others magnetic dipole moments.

According to DLR internal documentation regarding the power system the following techniques are used on GRACE:

- String polarity and layout is selected to minimize the panel DC magnetic moment and DC magnetic fields emanating from local current loops on the panels.
- All wire pairs are run tightly twisted.

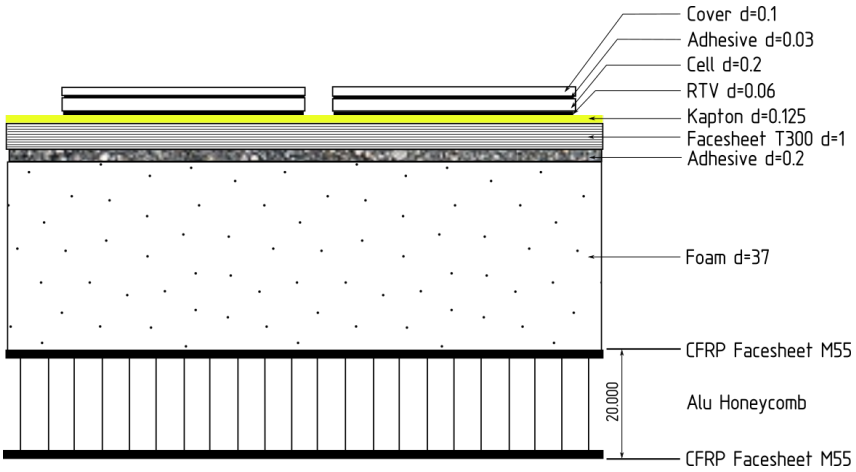

Fig. 3.9: Illustration of the solar panel layering structure. All values in mm. [12]

It the scope of this work it is assumed that magnetic effects are created, despite all measures taken. The effects may be supported by unfavorable aging behavior, partial failure of the panel or damage due to impact of space debris. In all cases failure of individual strings may cause an imbalance within the panel that may cause an increase of the magnetic disturbance. This is realistic considering the long duration of the mission. The model differentiates between two possible scenarios illustrated in Figure 3.10: This net current can't be transformed into a dipole

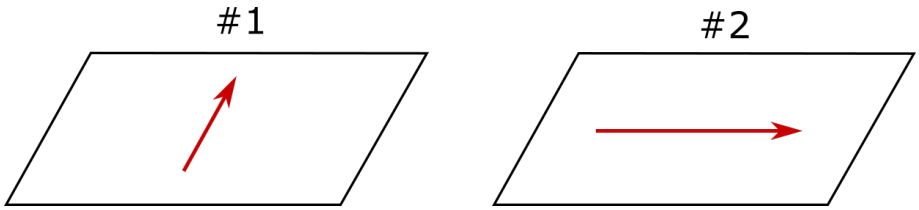

(a) Model #1: A net current parallel to the short side of the panel (Y-Z-plane).

(b) Model #2: A net current parallel to long side of panel (parallel to X-axis).

Fig. 3.10: Illustration of two possibles scenarios of a net current running within the solar panels. The current may be be caused by an imbalance within the panel due to aging effects or partial failure of the panel. Interaction with the magnetic field may induce a Lorentz force and a torque on the satellite

moment straight-forward. Instead, the approach is to calculate the Lorentz Force induced by the current in connection with a lever. The Lorentz Force acting upon a straight wire in a surrounding magnetic field $\vec{\mathbf{B}}$ is determined by equation 3.13. Calculation requires knowledge of the current $\mathbf{i}$ and the length and orientation of the wire $\vec{\mathbf{l}}$.

$$\vec{F}_L = i\,(\vec{l} \times \vec{B}) \tag{3.13}$$

The torque is then:

$$\vec{T}_L = \vec{r} \times \vec{F}_L \tag{3.14}$$

The force applies in the geometrical center of the panel, the momentum lever $\vec{\mathbf{r}}$ can be derived from Figure 3.2. The following $\vec{l}_i$ are assumed w.r.t. the size of the solar panels:

$$\vec{l}_{1,left} = \vec{l}_{1,right} = \vec{l}_{1,top} = (3.12,\, 0,\, 0)^T m \tag{3.15}$$

for model #1 and

$$\vec{l}_{2,left} = (0,\, 0.74,\, -0.62)^T m \tag{3.16}$$

$$\vec{l}_{2,right} = (0,\, -0.74,\, -0.62)^T m \tag{3.17}$$

$$\vec{l}_{2,top} = (0,\, 0.69,\, 0)^T m \tag{3.18}$$

for model #2, with the convention that the *left* panel is the one in *negative Y-direction*. The current shall be maximal when the Sun vector $\vec{\mathbf{S}}$ is parallel to the panel normal $\vec{\mathbf{n}}$ and decline as the enclosed angle α grows. The following cosine relation can be formulated:

$$i = i_0 \cos\alpha = i_0 \left(S_x n_x + S_y n_y + S_z n_z\right). \tag{3.19}$$

The frame rotation is chosen such that all normal vectors have the form $(0,1,0)^T$, which simplifies the equation to

$$i = i_0 S_y. \tag{3.20}$$

The maximal current $\mathbf{i}_0$ is the scaling factor for the magnetic effect. 1 A is chosen as a starting point. Obviously, the SP do not generate any currents during eclipses. The determination of Sun and eclipse phases is analogous to that in chapter 3.2. The necessary Sun and magnetic field telemetry is stored in different 24 hours data packages with unequal sampling rates. The data arrays are fitted by filling up blank time steps with the last known value. This allows calculating derived values for every second of the observed period. The arising error is neglected given that the observed time scales do not go lower than individual orbits. Figure 3.11 shows the resulting torque for both scenarios as well as low and high β'. In the first scenario a torque about all three axes is generated. The values are constantly positive in roll during Sun periods. Remember that the SRP roll torque is approximately zero for a small β'. The explanation is that the magnetic torque on the left and right side has the same sense of rotation and adds up, while opposing SRP torques cancel each other out. In the second scenario only a torque about X is induced. All curves show an oscillation with a period of one day that originates from the natural form of the magnetic field. The scheme in Figure 3.12 gives an overview of the model structure. Both magnetic effects are further analyzed in chapter 4.

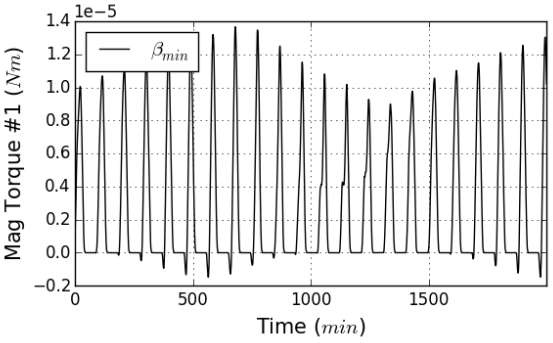

(a) Panel induced torque #1 for $\beta' = 0$ deg.

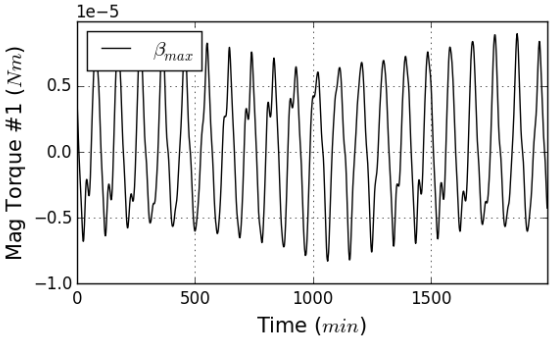

(b) Panel induced torque #1 for $\beta' = -88$ deg.

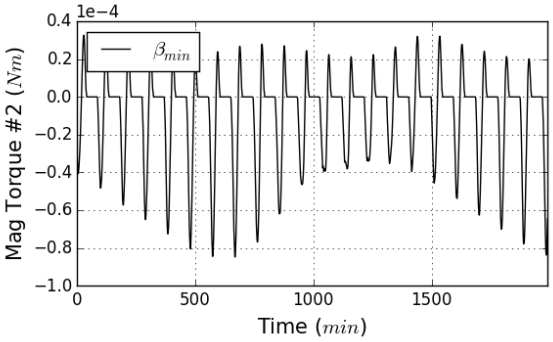

(c) Panel induced torque #2 for $\beta' = 0$ deg.

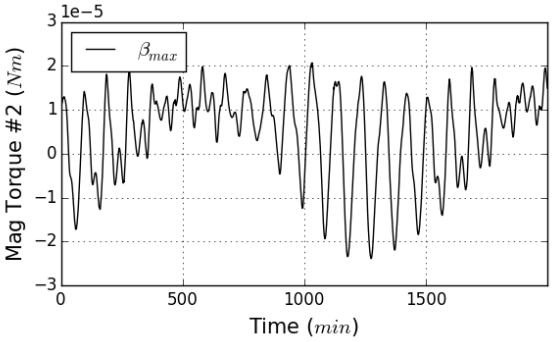

(d) Panel induced torque #2 for $\beta' = -88$ deg.

Fig. 3.11: Illustration of the modeled magnetic torque about the roll axis originating from a current leak within the solar panels. Model #1 denotes a current in satellite Y-Z-direction along the short side of the panel, model #2 a current in X-direction parallel to the long side. The torque is modeled with a hypothetical current size of 1 A.

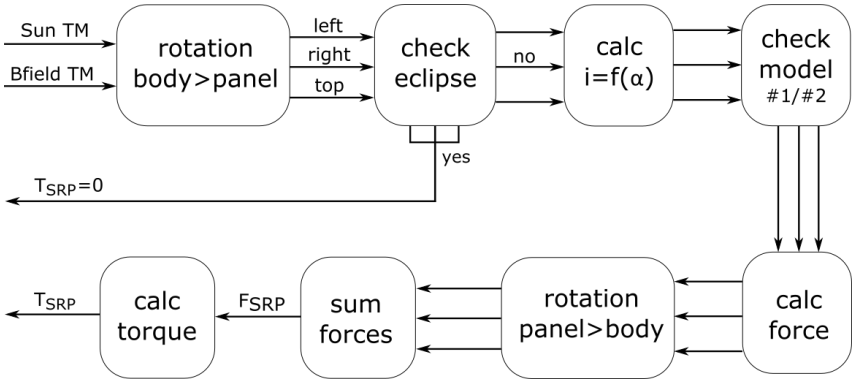

Fig. 3.12: Model structure of the panel induced disturbance torque.

4 Analysis of disturbance forces

With the models described in the previous chapter, the effect of the disturbance forces on the attitude of GRACE can now be analyzed. The main goal is to determine the cause of the observed asymmetry in the roll thruster activation in consequence of orbital disturbance forces. A special objective is to prove or disprove the existence of perturbations originating specifically from current flows within the solar panels. The detection of an effect may provide evidence of possible damage or limited functionality of the panel.
Before an analysis of the long-period effect can be made, it is necessary to take a close look at the Pulse Width Modulator Error (PWM). The strong noise in the data does not allow a straight-forward interpretation of the progression. A detailed analysis is done to reveal the main influences on the attitude and to confirm that all major disturbance torques have been considered and modeled correctly.
A comprehensive characterization of the roll attitude demands the consideration of its behavior on all time scales. The observation of long-period effects stands in the focus of this work. Along with the explanation of the thruster activation it, the observation of long time intervals is well suited to inspect the long-term stability of the GRACE satellite design. However, this type of analysis requires a lot of averaging of the data, which can lead to the loss of relevant information.
The analysis of the short-term attitude is necessary to account for this loss and obtain information that cannot be gained from the study of long-period effects alone. This applies to the missing information on the magnetic dipole moment vector $\vec{m}$, specifically the weighting of the individual X, Y and Z-components. At the same time, the inspection of the short-term attitude implies significantly stronger fluctuations of the attitude data. Knowledge of the long-term effect of certain disturbances is helpful to subtract it from the PWM data and reduce the noise.
This illustrates the interconnection between short and long time scales and the necessity to consider both types of effects.

4.1 Validation of disturbance models

In this section the structure of the primary attitude parameter, the PWM, is analyzed. The objective of this analysis is to determine the main influences on the roll stability and thus verify that all relevant disturbance forces are covered by the models presented in chapter 3.
In chapter 2.3.3 the difficulty of interpreting the PWM was stated. It comprises the weighted attitude and rate errors caused by external disturbance forces, stochastic perturbations, maneuvers as well as the corrections by the thruster and MTQ torques. An example of smoothed PWM

data for one day is shown in Figure 4.1 for the attitude about the X-axis. Small fluctuations are filtered out by taking the mean value of each minute. Additionally, a Savitzki-Golay filter is used upon the data set. The algorithm is similar to a classic moving average, but here the sampling points are individually weighted to account for local extrema [23]. The resulting plot hints at periodicities in the data. However, a detailed interpretation is still not possible without further information.

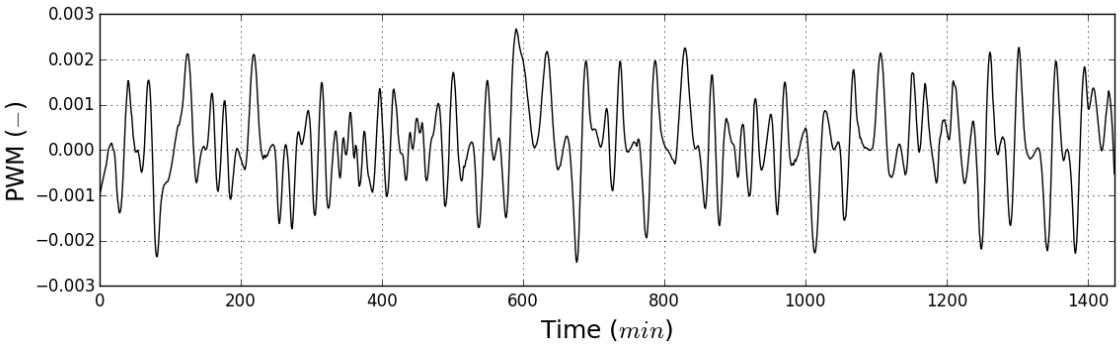

Fig. 4.1: Example of PWM data smoothed with a 60s average and a Savitzki-Goley (SG) filter. First periodicities are visible compared to raw PWM data.

Here, a Fast Fourier transformation (FFT) is used to search large sets of PWM data for characteristic frequencies of periodic effects in an efficient way. In this work a Cooley and Tuckey algorithm is used [24]. The idea is to compare the FFT spectrum of the PWM with the spectra of the modeled disturbance effects. Corresponding frequencies should indicate, whether the effect can potentially have an influence on the attitude. The models should include all periodicities discernible in the PWM data. The obtained spectrum of the PWM is presented in Figure 4.2 for GRACE 1. It is derived using 322 days of telemetry. The spectrum of the GRACE 2 PWM can be found in appendix A.2.2. All three axes are included here for the sake of completeness.

The distinct peaks in the graphs prove that the influence of various effects can be found in the data. In the interval from 100 min to 1440 min (full day) distinct periodicities are visible at 1440 minutes in yaw and 720 minutes in roll. Both are visible in pitch, but are not very pronounced. Smaller peaks are noticeable in roll and pitch at 360 minutes (1/4 day). In the range below 100 minutes similar patterns are visible in all three axes. Most pronounced is a pattern of three peaks, one at ca. 94 minutes (orbital period) and two neighboring peaks about 6 minutes before and after (side peaks). A similar pattern can be seen around ca. 47 minutes (half orbital period) which is less pronounced in pitch. The same phenomenon is found again at shorter periods. The repetition of the same pattern indicates that it is caused by one particular effect. In pitch, a cluster of peaks is visible at short periods (<10 minutes) that is not found in roll and yaw.

The following comparison is focused on the effects in roll, but builds bridges to the other axes where possible. Analysis of pitch and yaw requires consideration of additional disturbance effects that may be further investigated in the context of follow-on work.

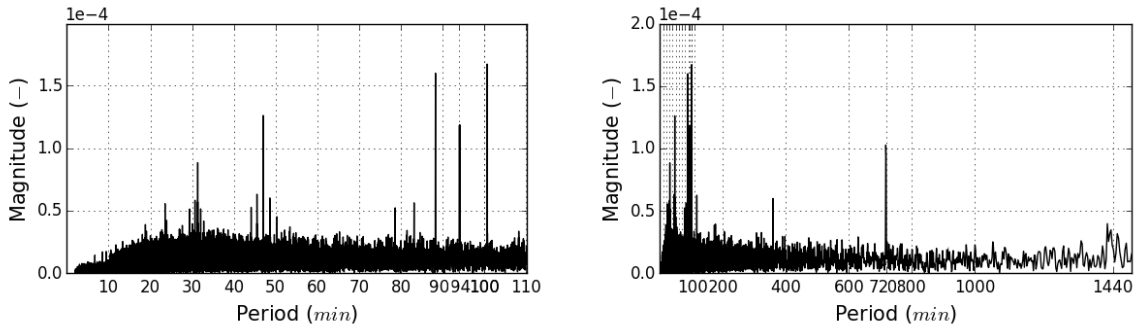

(a) Spectrum of the PWM for the Roll attitude. A pronounced pattern of peaks is visible at the orbital (ca. 94 minutes) and half orbital (ca. 47 minutes). Less distinct repetitions are visible at smaller periods. Further periodicities are noticeable at the 720 minutes (half a day) and 360 min marks. A weak 1440 minutes (full day) periodicity is discernable.

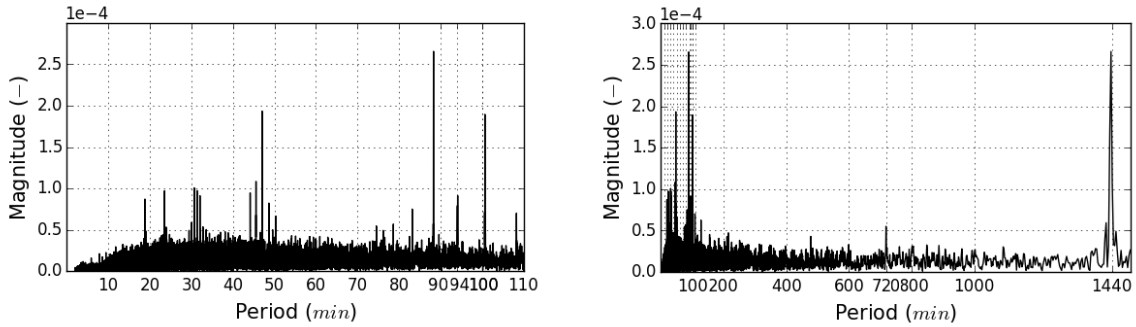

(b) Spectrum of the PWM for the Yaw attitude. The distribution of peaks resembles that in roll closely. The peak at the orbital period (ca. 94 minutes) is slightly less pronounced. A very disitnct peak is located at the 1440 minutes mark. The 720 minutes peak is very small compared to roll.

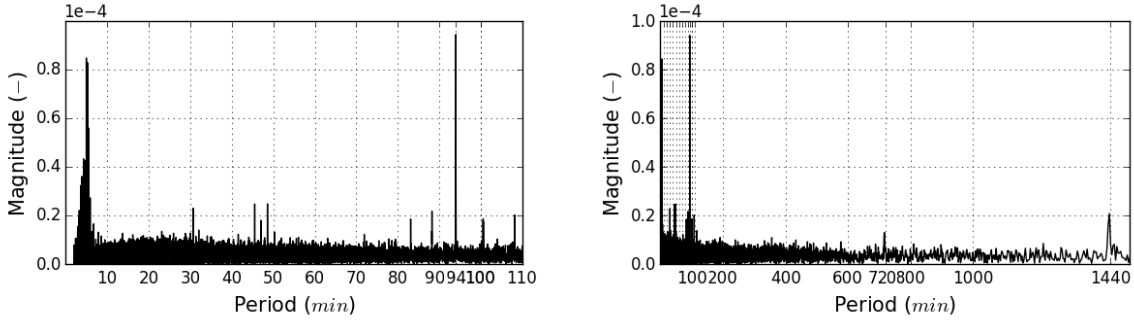

(c) Spectrum of the PWM for the Pitch attitude. The strongest periodicity is visible at the orbital period (ca. 94 minutes) mark. It is surrounded by a sequence of smaller peaks. The peak at the half orbital period is less pronounced compared to the other axes. A cluster of high-frequent peaks (<10 minutes) is noticeable that doesn't appear in roll and yaw.

Fig. 4.2: Fast Fourier spectra of the PWM in all three axes derived from 322 days of data (cycle 4, GRACE 1). All peaks indicate periodicities of the effects that influence the respective attitude.

Comparison with spectra of other cycles shows that sometimes the distinctiveness of peaks may vary slightly, most-likely due to the large amounts of input data and the multitude of influencing effects. No significant changes or appearance of previously non-detected peaks was noticed over the course of the mission.

The spectra in Figure 4.2 show the Fourier Transformations of the four modeled disturbance torques and the MTQ torque.

Solar Torque

The SRP torque (Fig. 4.3a) shows a dominant periodicity at the orbital period. This conforms to the fact that the satellite reaches the same position relative to the Sun precisely after one revolution, independently of Earth's rotation. Naturally, this periodicity appears in the PWM. A smaller peak is visible at a half orbital period. This peak was found to have no physical meaning in regard to the Sun. It may be caused by other effects influencing the roll attitude, which in turn may influence the CESS measurements. Imagine that twice per orbit

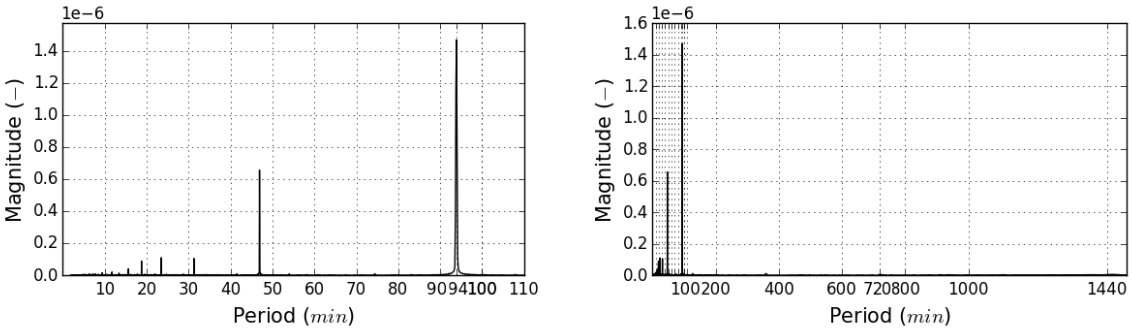

(a) Spectrum of the SRP torque. The most pronounced peak is visible at the orbital period that is clearly connectable to the motion of the satellite realtive to the Sun that repeats itself with every revolution. The smaller peak at the half orbital period may be indirectly caused by other disturbances that influence the CESS measurements. No periodicities longer than the orbital period are visible.

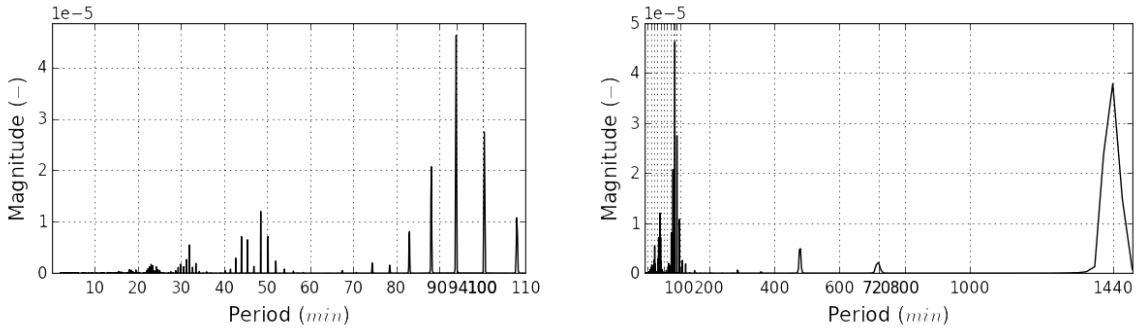

(b) Spectrum of the RDM torque. Characterisitc patterns of peaks are located around the orbital and half orbital period. Another distinct peak is visible at the 1440 minutes (full day) mark that is no found in the PWM. The periodicity may be caused by modeling specifics. Another explanation is a cancellation with the respective periodicity of the MTQ torque (see text).

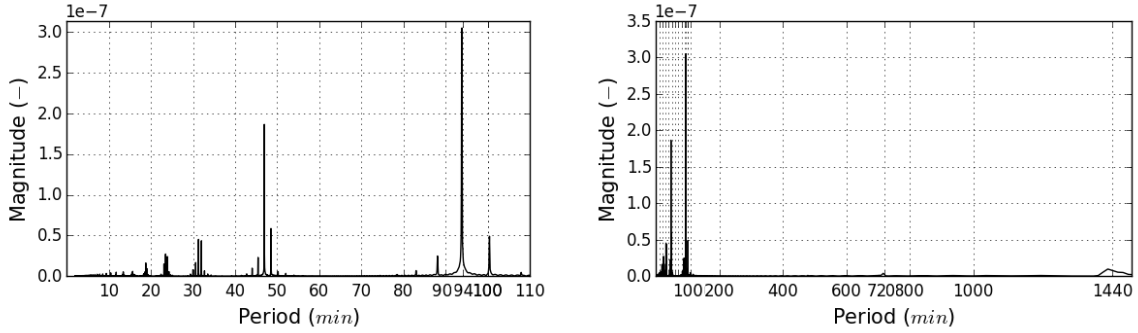

(c) Spectrum of the panel induced torque #1. The characterisitc patterns of peaks are visible but less pronounced. The most dominant peaks are located at the orbital and half orbital periods. No peaks are visible above the 100 minutes mark.

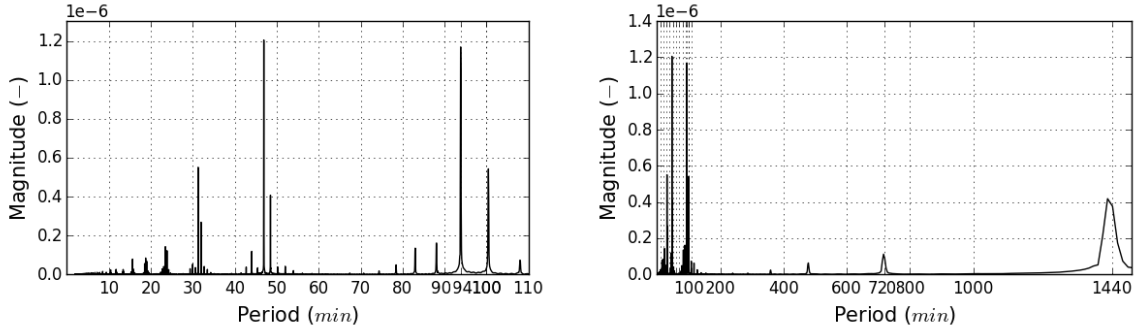

(d) Spectrum of the panel induced torque #2. The distribution closely resembles that of the panel torque #1. The peak at the 31 minutes mark is slightly more pronounced. Small peaks are visible at the 480, 720, and 1440 minutes marks.

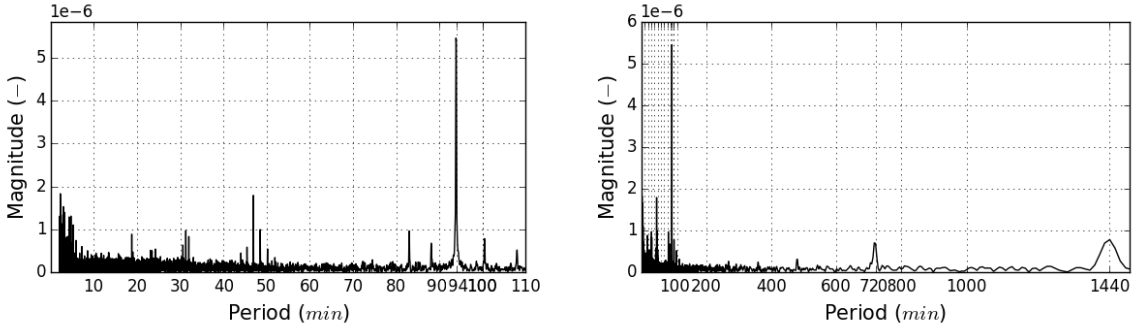

(e) Spectrum of the MTQ torque. A repeated pattern of peaks is noticeable around the orbital and half orbital period marks. The orbital periodicity is the most dominant in the spectrum. Small peaks are discernable at the 720 and 1440 minutes marks. A cluster of peaks at periods <10 minutes may be connected to the cluster seen in the spectrum of the pitch attitude.

Fig. 4.2: FFT spectra of all modeled disturbance effects and the MTQ torque in roll. All peaks present characteristic periodicities of the respective effect. A consistency with peaks observed in the PWM indicates that the effect does potentially influence the attitude.

the attitude of the satellite changes is changed from a positive to a negative tilt. This then would influence the CESS measurements and cause a peak at the half orbital period. This assumption may, however, need further investigation. The SRP shows no periodicities above the orbital period.

RDM Torque

The spectrum of the RDM torque can be modeled even though detailed information on the components of $\vec{m}$ is not available. This is due to the fact that the main contributors to the torque are the B_y and B_z components of the magnetic field. Their inherent periodicities stay the same, irrespective of the weighting of $\vec{m}$. Nonetheless, it has to be noted that the model is strongly simplified, above all due to the largely constant magnetic dipole moment used in the model. This simplification may influence the peaks of the FFT. The resulting loss of information has to be accepted at this point.
The spectrum (Fig. 4.3b) shows a strong periodicity at 1440 min. Physically this peak can be attributed to the tilt between the geographic and magnetic axes of the Earth. The magnetic pole 'rotates' about the geographic axis in one day. This rotation is also noticeable in the spectra of panel torque #2 and the MTQ. Interestingly, this peak is not visible in the PWM. A possible explanation could be related to the fact that the torques of disturbance and actuator are reversed. Given the relatively long period, the two effects may cancel each other out so well that the effect is no longer pronounced in the PWM. The same reasoning does not hold true for effects at higher frequencies such as the orbital period. Another theory is that all visible full day periodicities may be connected to the telemetry packages that contain 24 hours of data. A long sequence of files may cause a periodic effect during linking of the cutting points. Small peaks are visible at the 480 and 720 minutes marks. A physical explanation of these effects was not found, however the latter peak can be found in the magnetometer data and the FFT spectrum of the magnetic field vector shown in appendix A.5.
Below 110 minutes, familiar patterns of peaks are visible at orbital and half orbital periods. This is a strong indicator that the roll attitude of GRACE is dominated by magnetic effects. The repeated pattern is clearly noticeable in all spectra that use magnetic field data as input. Indeed, the same patterns can be observed in the spectrum of the magnetic field vector. They display inherent properties of the magnetic field's dynamics. The orbital peak may, to some extent, reflect the Sun's influence on the form of the magnetic field between day and night side. Similar to the half orbital peak in the SRP spectrum it may be enhanced by the interconnection of all effects. The nature of the pattern is not further investigated in the scope of this work. The correspondence between the PWM and the disturbance model is sufficient for the analysis.

Panel induced torques

The spectra of the panel induced disturbances (Fig. 4.2c, 4.2d) closely resemble the spectrum of the RDM torque. The peak patterns due to the influence of the magnetic field are clearly visible. The side peak at approximately 100 minutes appears to be more pronounced, especially in model #2. The orbital and half orbital peaks are further emphasized by the Sun as second

influencing factor in both models. Above 100 minutes model, #1 does not show any pronounced peaks. In model #2 a peak is clearly visible at the full day period. Two small peaks are discernible at the 480 and 720 minutes marks that are also found in the PWM. The same argument applied to the full day peak in the RDM spectrum can be used again here. The correspondence with the PWM confirms that either torque could potentially exist. Both models will be further analyzed to find evidence of a panel induced disturbance.

Magnetic Torque Rods

The MTQ spectrum (Fig. 4.2e) comprises a half day peak corresponding with the equivalent peak in the PWM. This periodicity originates from the magnetometer data. The full day periodicity has been discussed in line with the RDM spectrum. It may cancel each other out with the peak in the magnetic spectra, such that no pronounced peak appears in the PWM roll spectrum. The peak patterns induced by the magnetic field are visible yet again. It is not exactly clear why the cluster of high frequent peaks is not visible in the PWM spectrum. The periodicities could be connected to the Z-current of the MTQ, which is also required to control the pitch torque. That way the peaks may be related to the cluster of peaks observed in the spectrum of the pitch attitude at high frequencies. In any case, this does not question the existence of the MTQ torque.

Summary

The correspondence of the individual periodicities is illustrated in Figure 4.3. The most characteristic peaks found in the PWM can be traced back to the modeled disturbance and actuator effects. The weakly pronounced full day peak in the PWM is attributed to a possible cancellation of the disturbance and actuator peaks as the respective torques have opposed signs and the period is relatively long compared to the orbital and shorter periods. Another explanation may be related to the size of the telemetry packages, which contain exactly 24 hours of data. This could induce an anomaly during the linking of many consecutive packages. A peak in the PWM spectrum that is larger than the respective peaks in the disturbance models is the 360 minutes peak. This duration of 1/4 of a day could not be logically explained by the motion of the satellite relative to the Sun or the magnetic field. However it seems to be related to the latter, as a weak 360 minutes periodicity is noticeable in the Figures 4.2d and 4.2e. Finally, three models show a peak at 480 minutes (1/3 day) that is not visible in the spectrum of the attitude error. The fact that the peak is visible in the spectrum of the MTQ, which is assumed to be free of any modeling errors, suggests that it has a natural cause. It may be some sort of distinct feature in the data that is not pronounced in the PWM due the strong noise. This phenomenon has to be accepted. The following analysis should not be hindered significantly as the observation of short-period effects focuses on single orbits. Up to the orbital periodicity a match of all peaks can be confirmed.
On a last note, a transformation of the thruster activity could not be modeled. Thorough inspection of the telemetry showed that the thrusters responsible for the roll torque are typically activated in either direction twice per orbit which translates to a half orbital peak in the FFT.

This frequency corresponds to the explanation in chapter 2.3.2 stating that roll thrusters are commanded in the vicinity of the equator where MTQ control is limited.

Effect	Period [min]										
		47				94		360	480	720	1440
PWM	+	+	+		+	+	+	+		+	+
Solar Torque		+				+					
Mag Dipole	+		+		+	+	+		+		+
Panel #1	+	+	+		+	+	+				
Panel #2	+	+	+		+	+	+	+	+	+	+
MTQ	+	+	+		+	+	+	+	+	+	+

Fig. 4.3: The graphic illustrates the correspondence of periodicities between the PWM and the modeled disturbance forces, including the magnetic torque rods. Green boxes mark peaks that match with peaks in the PWM. Orange boxes indicate frequencies not found in the attitude error.

4.2 Long-period effects

4.2.1 The anomalous roll thruster behavior

This section focuses on an observation that was made during routine analysis of AOCS telemetry. It is illustrated in Figure 4.3. The vertical axis of the plots shows the difference between the summed thruster on-times (ΔTOT) of two opposing thrusters, e.g. +roll and –roll, for one day. On first thought, one may expect the thrusters to be activated approximately the same amount of time in both directions, with a certain amount of non-systematic deviations. This thought is confirmed for the motion about the pitch axis (Fig. 4.3c). Very high deviations, e. g. at day 60, 110 or 170 suggests a maneuver or mode switch that was performed in that period. However, the deltas calculated about the roll (Fig. 4.4a) axis display a clear, systematic variation of the values. Following a sine-shaped form the ΔTOT grow over a period of about 80 days up to a maximum amplitude of ca. -30 s to -50 s per day. The curve then drops over another 80 days. After the values cross zero, the pattern is repeated in the opposite direction, that means with positive deltas. Thus, the same oscillation is repeated over a period of approximately 322 days, which is exactly one GRACE cycle. In Figure 4.3 every curve or color represents one cycle of the mission between cycles 6 and 14. It can further be stated that the zero crossings correlate with small β' while maxima of the curve correspond to periods with high β'.
A very similar pattern is noticeable in the yaw motion (Fig. 4.4b), but with a clearly smaller amplitude, approximately by a factor 10 compared with roll. This large difference suggests that the visibility of the effect in the long-period yaw attitude is caused by a coupling of the roll and yaw motions rather than the axis being affected by the same effect(s). It can be noted that

the sine-shaped form is even less visible in the yaw plot on GRACE 2 (appendix A.13b) which further stresses the assumption the effect is caused by a coupling of the axes.
The surplus of thruster activation hints at the existence of an effect that causes an undesired tilt of the satellite. Judging from the fairly consistent progression of the curves even in the later cycles of the mission, the responsible disturbance must have a constant magnitude. The relevance of the asymmetric thruster performance becomes more obvious when looking at the total activation time of the roll thrusters per day. Between cycles 6 and 14 the roll thrusters operated $140 s/day$ on average. This means that large ΔTOT of ≈ 40 s amount to a surprising 28.6 % of the total thruster activation of one day. The average fuel consumption is $\approx 0.02\,g$ per second of thruster activation. An estimation yields that over the whole mission (17 cycles) about 2.7 kg of fuel have been consumed by the asymmetric thruster activation. This is equal to 7.8 % of the total fuel mass of one satellite. All of the above observations are equally true for GRACE 2. The respective plots including the earlier cycles of the mission are shown in appendix A.2.5. The periodicity suggests that the phenomenon may be related to the solar cycle. All disturbance forces which are modeled in chapter 3 are connected to the solar cycle and could theoretically contribute to the thruster actuation.

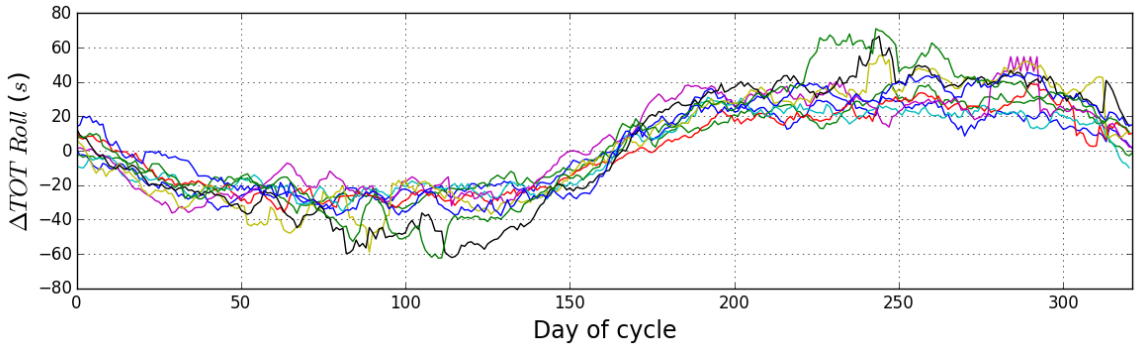

(a) ΔTOT values in roll. The values show a sine-shaped progression with a period of 321.6 days.

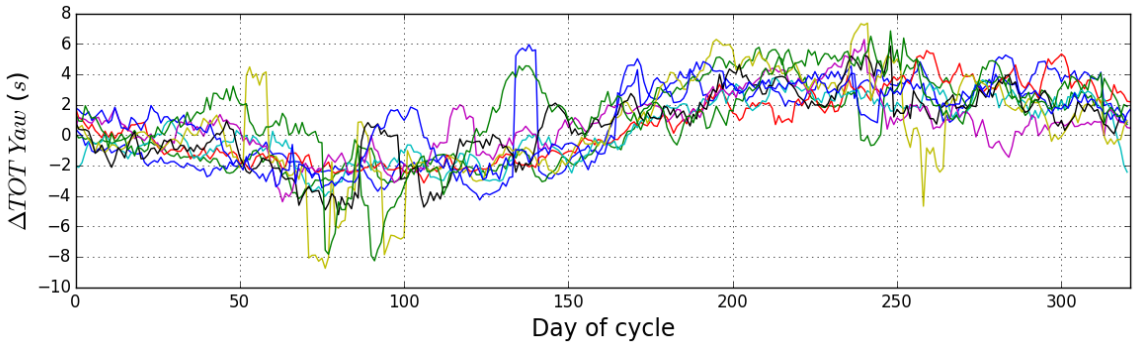

(b) ΔTOT values in yaw. The pattern is similar compared to roll. The amplitude is smaller by a factor of 10 compared to roll, which indicats that in all likelihood the effect is visible due to a coupling of the roll and yaw motion.

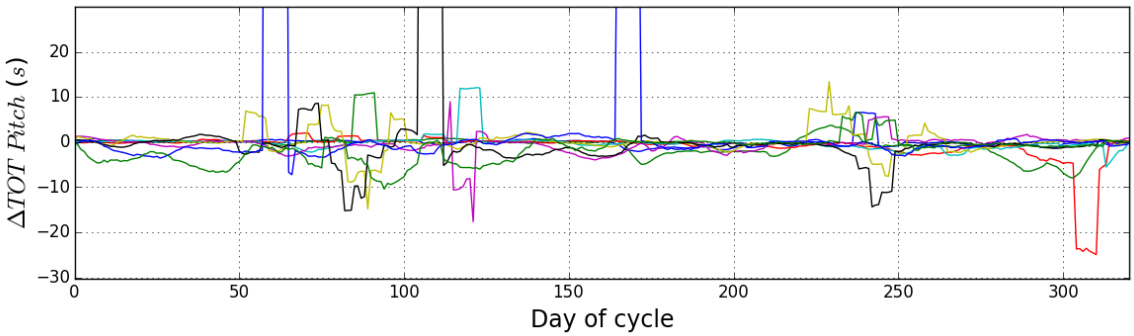

(c) ΔTOT values in pitch. The values show non-systematic fluctuations about zero. This suggests that the pitch attitude is not influenced by the periodic effect.

Fig. 4.3: Illustration of the ΔTOT observed in the ATH actuation based on data from cycles 6 to 14 (GRACE 1). The values are derived from the sum of all thruster activations (positive and negative) of one day. In roll and yaw a deviation from zero is noticeable indicating a long-period effect on the satellites.

4.2.2 Long-period effects of the disturbance torques

To understand the effect, the first step is to verify whether the performance of the attitude thrusters can be seen in the general attitude of the satellite about the X-axis. It is highly unlikely that *no* effect is visible given the significant amount of fuel consumption the thruster activation has caused. However, primary means of attitude control are the MTQ. If no similar pattern is noticeable in the PWM this would mean that the effect has a negligible impact on the satellite. The analysis then needs to continue without consideration of the PWM. To get a representative value of the PWM for each day, the arithmetic mean of all values is calculated. In a sense, the derived value compares all positive and negative deviations of the attitude from zero and checks for a notable tendency to either side. To compare the two parameters that are of different magnitude a linear least-squares (LSQ) algorithm is used on the ΔTOT values. The algorithm is has the form shown in equation 4.1 [25].

$$TOT_{LSQ} = a + b \cdot TOT \tag{4.1}$$

Figure 4.4 exemplifies the fitted curves for cycle 8. The progression of both curves are clearly similar with a sine-shaped form. The same similarity holds true for other cycles (see appendix A.2.4). This comparison clearly shows that the disturbance is large enough to influences the long-term roll attitude of both satellites.

In a next step, the long-period plots of the solar pressure and magnetic torques are derived analogously to the PWM. By logic, the derived curves must display the sine-shaped progression and periodicity of one cycle, if the respective effect contributes to the observed thruster performance. The resulting plots are visualized in Figure 4.4. The sine-like shape of the SRP torque is clearly identifiable, however some characteristic features stand out (Fig. 4.5a). Particularly

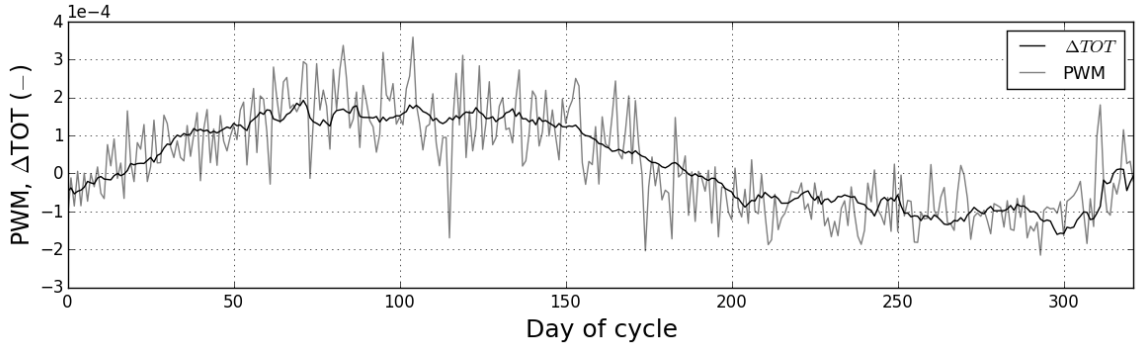

Fig. 4.4: Example of the ΔTOT and PWM long-period plots fitted using a least-squares algorithm (GRACE 1, cycle 8).

noticeable are the inflection points around the extrema of the underlying sine curve, which are also the points with a maximal β'. The curve further passes through a saddle point at β' zero in the middle of the cycle.

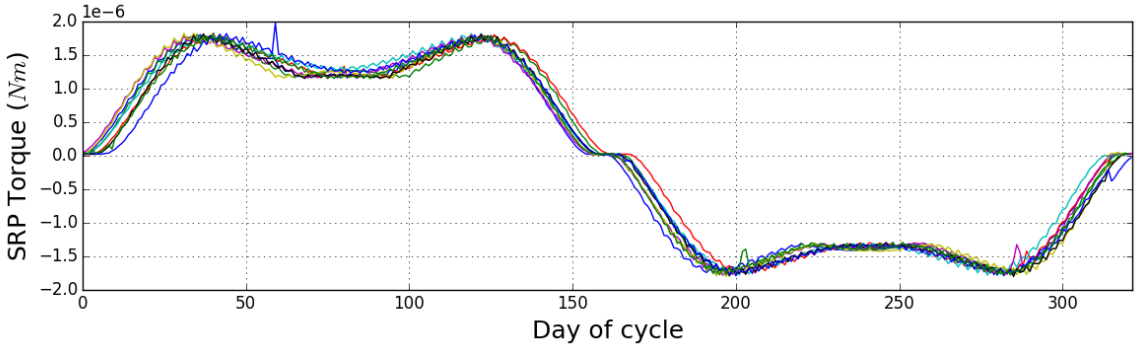

(a) The SRP displays a pronounced long-period effect. The curves show characteristic features around the zero passages and the extrema of the curve.

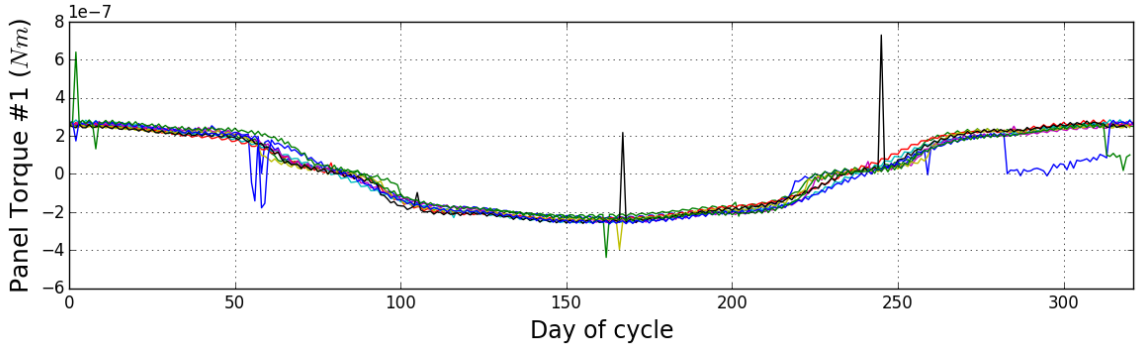

(b) The solar panel induced torque #1 shows a clear periodicity over one cycle. The curves are sine-shaped with a constant phase shift of $\pi/2$ compared to the ΔTOT observation.

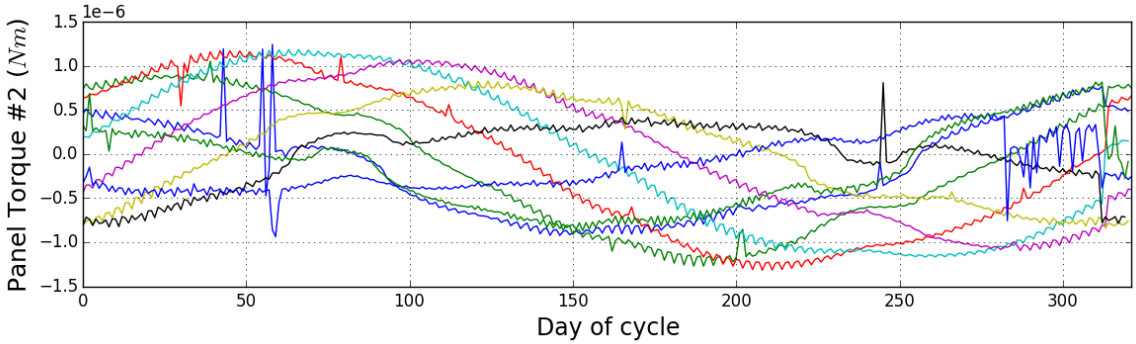

(c) The solar panel induced torque #2 has a sine-shape periodicity with a temporal shift of the phase. The shift is ascribed to the progression of the RAAN. An inconsistent phase argues against the existence of the effect.

Fig. 4.4: Illustration of the long-period effect of SRP and panel induced disturbances (cycles 6 to 14, GRACE 1). All values present the arithmetic mean of one day. A periodicity of one cycle and phase that matches the plot in Figure 4.4a indicate a connection to the observed thruster effect.

The inflection points can be explained by looking at one of the satellites at different phases of the cycle between the positive and negative extrema of β'. The principle is illustrated in Figure 4.6. Starting at β' zero (point A) the forces on the three Sun-pointing panels are balanced out.

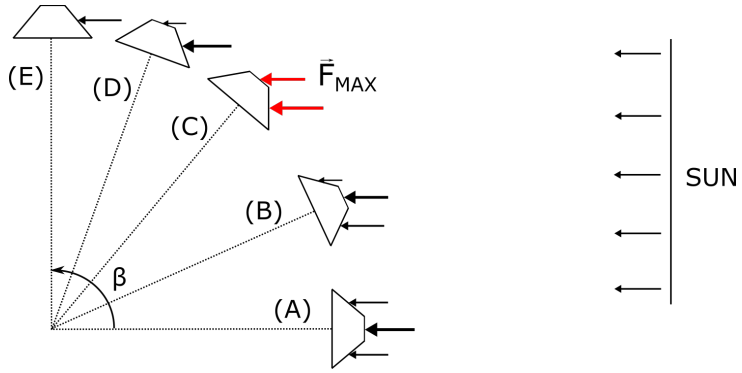

Fig. 4.5: Illustration of the total SRP on GRACE changing for different β' angles. (A) Forces are balanced out for $\beta' = 0$. (B) The balance shifts to one side as β' grows. (C) Maximum force for $\beta = \pm 50\,\text{deg}$ due to GRACE design. (D) Force drops during further growth of β'. (E) Stages are passed in reversed direction after β' reaches its maximum.

As β' starts to grow (point B) the balance shift to one side until at a β' angle of $\pm 50\,\text{deg}$ (point D) the Sun vector shines vertically on one of the side panels. According to equation 3.10 at this point the force on the side panel reaches its maximum. Further growth of β' (point E) reduces the force on the side panel and the top panel; the latter becomes zero at $\beta' = 90\,\text{deg}$. After the passage of an extremum the same states are passed through again in reversed order, hence the second local maximum of the curve. This principle works analogously for negative β' angles.

An observation that was made at this point is that the size of two consecutive indentations are not equal. This can be explained by the variation of the maximal β' angles for each period. This causation is illustrated in Figure 4.6. It shows the progression of the β' angle plotted over the SRP torque for cycles 6 to 12. Smaller maxima of β' yield smaller indentations between the two $\beta' = \pm 50\,\text{deg}$ passages and vice versa. The observed saddle points at each $\beta' = 0$ passage

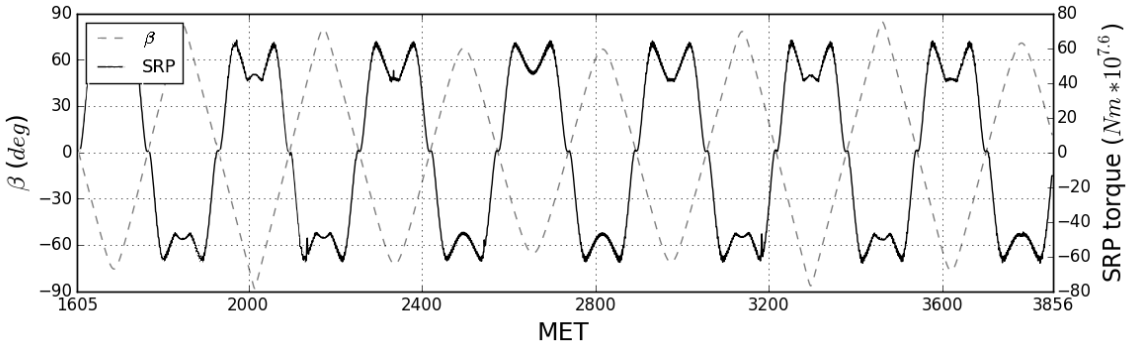

Fig. 4.6: Correlation between the SRP torque progression and the β' angle. Larger extrema of β' correspond to larger indentations in the SRP plot.

seem counter intuitive. A consistently changing β' angle should yield a progression equal to zero whenever all solar forces are balanced out, followed by a reversal of the sign. The analysis didn't provide any hint on a natural cause of this phenomenon. The most probable explanation is that the CESS measure equal Sun/eclipse periods over a period of several days, while in reality, there is a slight change of the full shadow and penumbra phases. The progression of the Y-component of the Sun vector for both side panels is illustrated in Figure 4.7. The vector has been rotated into the respective panel frame and the average values of one day has been calculated. Note that due to the definition of the frames only the Y-component is relevant for the calculation of the SRP torque. The raw telemetry data features the observed plateau around β' zero. Further analysis of this problem can be conducted within the scope of a follow-on work.
The long-period plot of the panel torque #1 (current in the Y-Z-plane) shows sine-shaped curves for all cycles (Fig. 4.5b). However the phase shows a consistent offset of $\pi/2$ compared with the PWM and SRP plots. The curves of panel effect #2 (current in the X-direction) are partially sine-shaped with a clearly pronounced temporal shift of the phase (4.4c). It is noticeable that for some of the cycles, the shape of the curves correspond well with the PWM and SRP curves (see cyan curve, cycle 9). However, this correspondence is not true in general. Both panel torques are influenced by the solar cycle and the magnetic field. The sine-shape is induced by the Sun. The low frequent shift can be explained by a shifting position relative to the magnetic field due to the progression of the RAAN. This shift manifests itself mainly in the B_y component, which has no influence on the torque in model #1, hence no shift is visible. Both effects are modeled using a hypothetical current of 1 A. Overall, the visualization of the long-period plots clearly suggests that the existence of a panel induced disturbance in this form is unlikely. This is a good result, which shows that no disturbance is originating from a malfunction of the panels. A positive result could indicate an insufficiently good design and manufacturing of the panels.

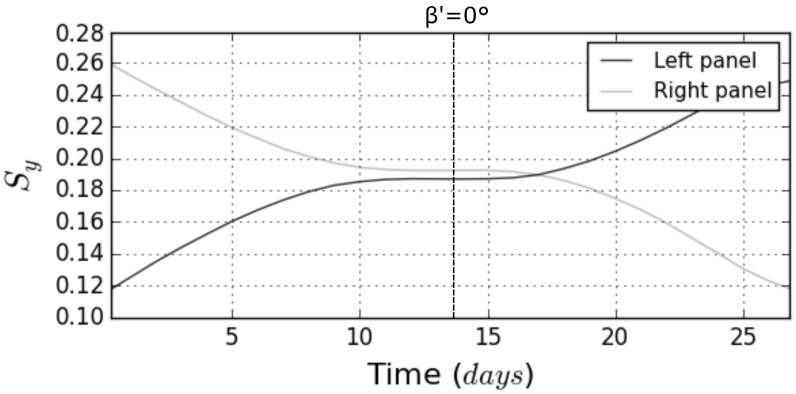

Fig. 4.7: Progression of the Y-component of the solar vector (in panel coordinates) for both side panels of GRACE 1. During phases with small β′ angles a plateau is visible in the data that causes a saddle point in the SRP plot.

A long-period plot of the RDM can't modeled at this point of the analysis due to missing information on the components of $\vec{m}$. In contrast to the panel induced torques it can be assumed that a magnetic dipole moment does exist. A contribution to the thruster effect has yet to be evaluated.

So far, the analysis leaves the solar pressure as the most likely cause of the thruster effect. In a next step the SRP is compared to the PWM data using an LSQ fit, analogously to the previous ΔTOT comparison. The exemplary plot in Figure 4.8 depicts the result for cycle 8. In this context the parameter chi^2 is calculated. Goodness of the LSQ scaling factors is indicated by small values of $chi^2 \ll 1$ [25]. An overview of all values calculated by the algorithm is provided in appendix A.2.3. The two curves show a clear resemblance. This is a very strong indicator

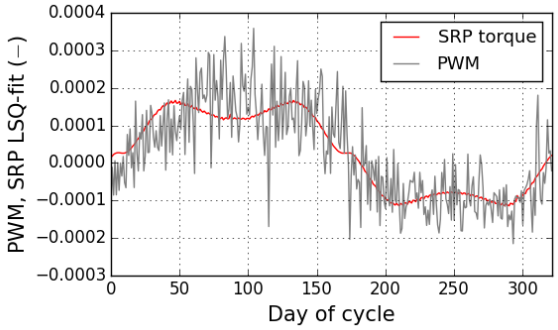

(a) Fit of the plots using an LSQ algorithm. The curves fit well indicating a direct relation between the two effects.

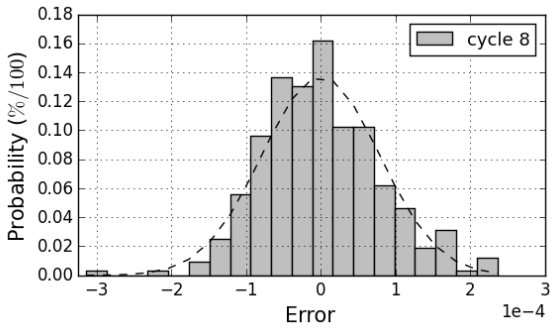

(b) Histogramm of the residues derived from the LSQ fit. The gaussian shape is a sign that no further effects are hiddin within the PWM.

Fig. 4.8: Comparison of the similarity between the long-period plots of PWM and SRP.

that the solar radiation is a main contributor to the effect. A closer look at the residues confirms the similarity of the two curves. The residues $RES_i = PWM_i - SRP_i$ should have a random

distribution, if no further periodic effects are 'hidden' within the PWM. This assumption is confirmed as the respective histogram shown in Figure 4.8b has a Gaussian form. The same analysis yields largely consistent results throughout the whole mission. Histograms of all other cycles are illustrated in appendix A.2.3. Small deviations from the typical Gauss-bell can be caused by local fluctuations of the PWM due to a temporary mode switches (which can last up to several days). An increasing amount of maneuvers were performed during the later cycles due to technical problems.

4.2.3 Quantitative investigation

The analysis calls for a quantitative classification and comparison of the relevant effects. The problem at this point is that the unit of the PWM has no physical meaning and is difficult to compare to physical effects. The ΔTOT parameter is more suitable for this analysis. The physical quantity that connects the torque $[Nm]$ and the time $[s]$ is the angular momentum $[Nms]$. According to Newton's First and Second Laws the satellite will rotate due to the applied torque and in the direction of the acting force vector unless there is an opposed, stabilizing torque. Newton's Second Law of motion for the force **F** is:

$$\vec{F} = m\vec{a} \tag{4.2}$$

where **m** and **a** denote mass and acceleration. The equivalent for a torque **T** and rotational motion is

$$\vec{T} = I\dot{\vec{\omega}}. \tag{4.3}$$

I is the moment of inertia, ώ the angular acceleration. The angular momentum **H** is defined as

$$H = I\omega \tag{4.4}$$

which can be written as

$$H = T\frac{\omega}{\dot{\omega}} = T\Delta t. \tag{4.5}$$

The angular momentum produced by a pair of thrusters during a single firing is then:

$$\Delta H = 2\,T\Delta t_B = 2\,F\,l\Delta t_B \tag{4.6}$$

where **l** is the momentum lever and $\triangle t_B$ the thruster burning duration.
The angular momentum is a conserved quantity. Hence, the total amount can be calculated for any period of time. Approximation of the integrals of both curves allows calculating the total **H** that is generated over a cycle and comparing it. The nominal torque applied by one roll thruster is 0.003 Nm (see 2.3.2). The total burning duration for each day is the ΔTOT value. Every value of the SRP plot represents one day and is therefore multiplied by 86400 s as a replacement for an activation time. Both integrals are thereby approximated by a number of columns equal to the amount of days in the cycle. The curves of angular momentum **H** produced by SRP

and ATH are exemplified in Figure 4.9. To put this in meaningful relation, the parameter **R** is

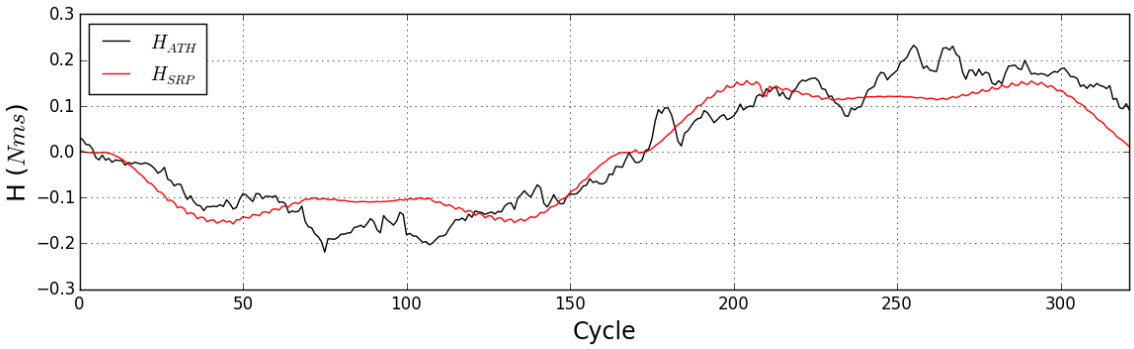

Fig. 4.9: Comparison of angular momentum H generated by the SRP and the ATH over the course of one cycle (GRACE 1, cycle 7).

calculated:

$$R = \frac{\sum(H_{ATH,i})}{\sum(H_{SRP,i})}, \tag{4.7}$$

where **R** represents the percentage of **H** produced by the SRP (H_{SRP}) that is compensated by the thrusters (H_{ATH}). An overview of R is provided in Figure 4.10. If the solar pressure is the

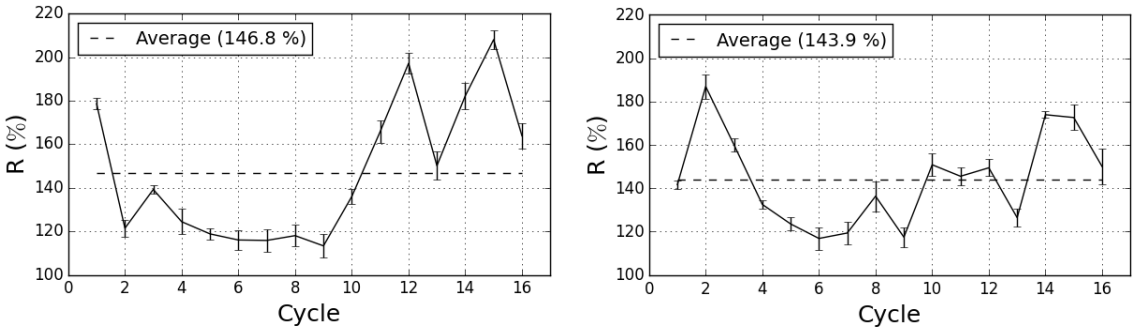

(a) Overview of R factor for GRACE 1.

(b) Overview of R factor for GRACE 2.

Fig. 4.10: Overview of the R factor for GRACE 1 and 2. Values above 100% imply that the thrusters generate more angular momentum than the SRP.

only cause of the thruster effect, R should display values $\leq 100\%$. However, the obtained average values of 143.9% (GRACE 2) to 146.8% (GRACE 1) suggest that the thrusters compensate more angular momentum than is applied by the SRP torque. This is a highly important result indicating that the SRP is not the only disturbance influencing the long-term attitude. The arguments presented in this chapter leave the RDM torque as only other source of disturbances. Up to this point the MTQ have been ignored. It is reasonable to assume that the angular momentum generated by the MTQ H_{MTQ} adds up to H_{ATH}. The MTQ torque is modeled using equation 2.1 and the technical data listed in table 2.3. The telemetry provides the desired coil currents.

Actuator	H_{h1}/H_{h2}
ATH	0.88
MTQ	0.64

(a) GRACE 1

Actuator	H_{h2}/H_{h1}
ATH	0.63
MTQ	0.48

(b) GRACE 2

Table 4.1: Comparison of the total angular momentum produced by ATH and MTQ within two different halves of a cycles H_{h1} and H_{h2}. The values are arithmetic means based on data from cycles 6 to 14. Values $\neq 1$ indicate an asymmetry within the satellites. The asymmetry is more pronounced on GRACE 2.

Calculation of the angular momentum H_{MTQ} is analogous to the calculation of H_{SRP}. A long-period plot of the MTQ torque is shown in Figure 4.11 for cycles 6-14. The shape of the curves

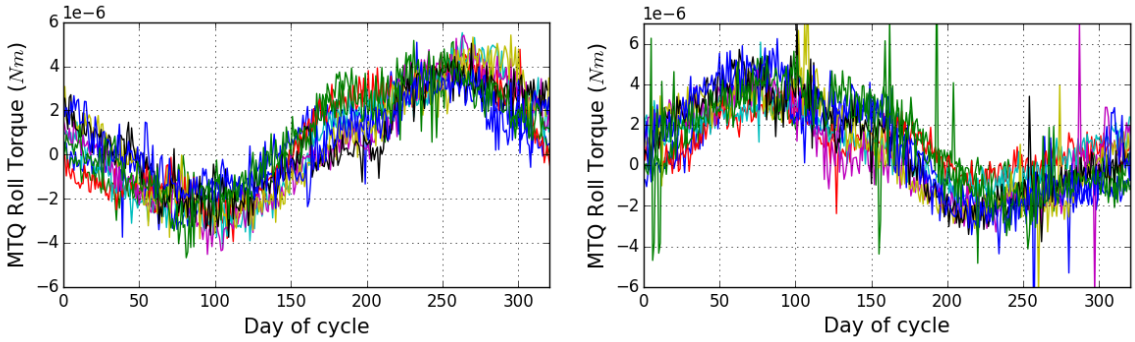

(a) MTQ torque GRACE 1. More activation is commanded during the second half of the shown cycles.

(b) MTQ torque GRACE 2. More activation is commanded during the first half due to the rotation relative to GRACE 1.

Fig. 4.11: Long-period plots the MTQ torque for cycles 6 to 14. An asymmetry is observable on both satellites. More AOCS activation is commanded when left panel is directed towards the Sun.

matches the shape of the ΔTOT. A minor deviance between the curves can be observed on both satellites due to the aforementioned progression of the RAAN. Most noticeable is an asymmetry between the individual halves of each cycle. The curves on GRACE 1 enclose a larger area underneath the curves during half 2. On GRACE 2 the effect is reversed. In other words, more activation of the AOCS actuators is commanded during phases in which the left panel is directed towards the Sun. This observation is confirmed by comparing the cumulated amount of **H** generated by both actuators during the individual halves of cycles 6 to 14. Average values for the observed period are listed in table 4.1. The numbers indicate that the asymmetry is stronger on GRACE 2. According to Figure 4.10, the ATH alone generate more **H** than the solar pressure. Summation of the two actuators yields a total **H** two to four times higher, depending on the half of the cycle. The following conclusions can be drawn from this observation:

- A magnetic disturbance must contribute to the overall effect. The RDM torque is the only reasonable option.
- The magnetic torque must have the same effective direction as the solar torque.
- The RDM torque is asymmetric. The disturbance is stronger when the left panel is illuminated on either satellite.

A long-period plot of the RDM torque that satisfies condition of an equal effective direction is presented in Figure 4.12. It is positive in the first half of the cycle and negative in the second for GRACE 1. The sign changes at every $\beta' = 0$ deg crossing. To receive a plot with this progression, the m_y and m_z components of the RDM must be chosen *negatively* during the first 160 days and *positively* during the second. Hence, the negative components correlate with (predominant) power generation on the left panel. This indicates that both components are influenced by the contribution of the side panels. The assumption made in chapter 3.3 is confirmed that the sign of the affected components has to change depending on which side is illuminated. The very simplified form of the plot results from the limited information on $\vec{m}$. It assumed to be sufficient to estimate the magnitude of the magnetic dipole moment. A detailed modeling is not desired in this work.
Note, that the components of the magnetic dipole moment vector have already been weighted in this plot. Information on the respective weighting factors $\vec{m} = (8, 1, 8)^T$ is derived in the short-period analysis in section 4.3.

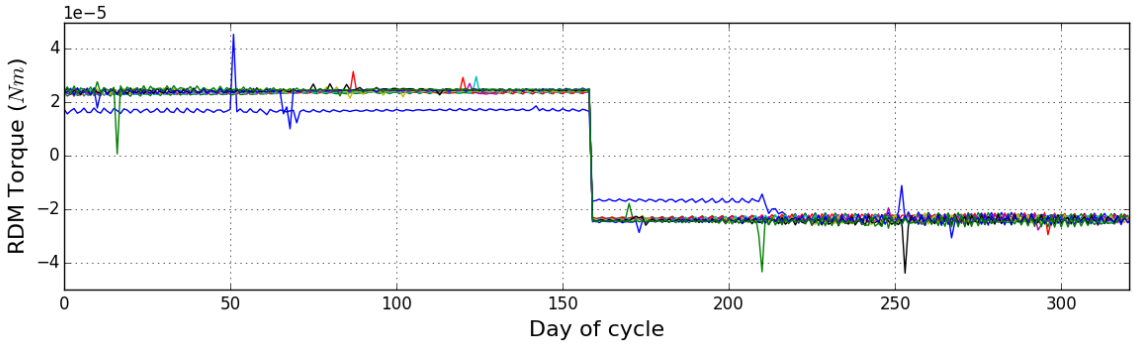

Fig. 4.12: Long-period plot of the simplified RDM torque on GRACE 1 (cycles 6 to 14). The plot is modeled using an RDM $\vec{m} = (8, \mp 1, \mp 8)$. The RDM torque must have the same effective direction as the SRP torque. The effect is reversed on GRACE 2.

Two possible scenarios come to mind that could explain the observed asymmetry. In scenario A, the imbalance is caused solely by the asymmetry within the satellite build. A larger disturbance during illumination of the left panel can be caused, if the contribution of the left panel adds up with the contribution of the rest of the electronic subsystem. The same part of it cancels out the effects induced by the right panel in the other phase. The similarity of the effect on both satellites is conditioned by the identical build.
In scenario B, a part of the imbalance may be caused by a one-sided panel torque. In Figure 4.4 it was assumed for the panel effect that a net current remains on all panels as a consequence

of technical imperfection. Failure of individual strings on just one panel would induce a different progression of the curves. A respective scenario is illustrated in Figure 4.13. The curves of magnetic torque #2 match the form of the actuator curves in first approximation. However, the amplitude of the curves varies immensely between the cycles due to the progression of the RAAN. The respective actuator curves do not show a varying deviation (Fig. 4.4a, 4.11). Additionally, this scenario requires an imbalance on the left panel of both satellites. A symmetric imbalance due to impact of micro debris is unlikely given the rotation between leading and following satellite. A strongly pronounced effect on the same panel simply due to aging is unrealistic, especially since the asymmetry can be observed right from the start of the mission. The above line of thought speaks in favor of scenario A, which will be further investigated.

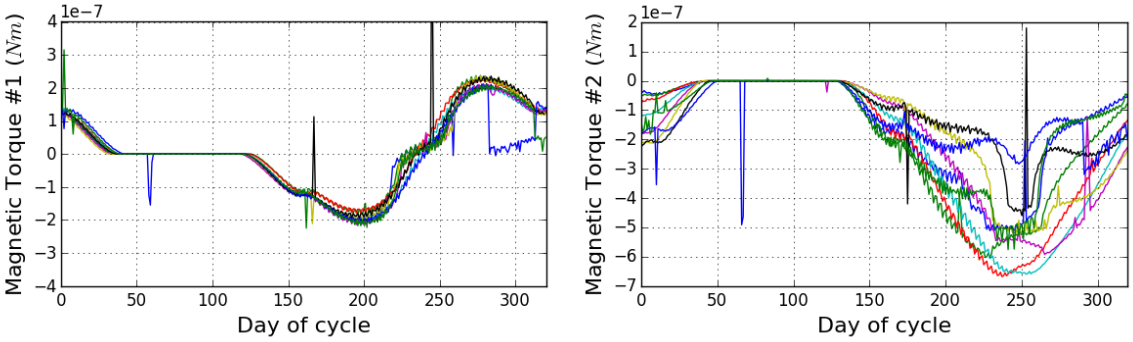

(a) Progression of a panel induced torque #1 generated by the left panel.

(b) Progression of a panel induced torque #2 generated by the left panel.

Fig. 4.13: GRACE 1 long-period plots of the magnetic disturbances #1 and #2 in case that only the left panel induces a torque (cycles 6-14, 1 A current). The effects are exactly reversed on GRACE 2.

At this point, the long-period effect can be lead back to two disturbances that are counteracted by two actuators. Three of the four effects can be modeled accurately leaving the magnetic torque as the only undetermined factor. This allows the desired quantification of the RDM by scaling the magnetic disturbance such that equation 4.8 is fulfilled.

$$H_{ATH} + H_{MTQ} \stackrel{!}{=} H_{SRP} + H_{MAG} \cdot a_{MAG} \tag{4.8}$$

The scaling factor a_{MAG} is calculated for both halves of cycles 2 to 14. Comparison of the factor of the two halves allows to further specify the magnitude of the asymmetry. The a_{MAG} factors are summarized in Figure 4.14. Note that cycles 15 and 16 are left out due to stronger noise in the data and the performed swaps, which keep the same side of the satellites directed towards the Sun. Cycle 1 is also not included due to strong fluctuations during the early mission phase. On GRACE 1 the values display a constant progression. A slight upward trend can be observed on GRACE 2 in the later cycles. It could be caused either by an actual increase of the RDM or possibly due to inaccuracy of the data. Factors of two associated halves show a fairly constant difference in size on both satellites. The relations are reversed after the first swap in cycle 5.

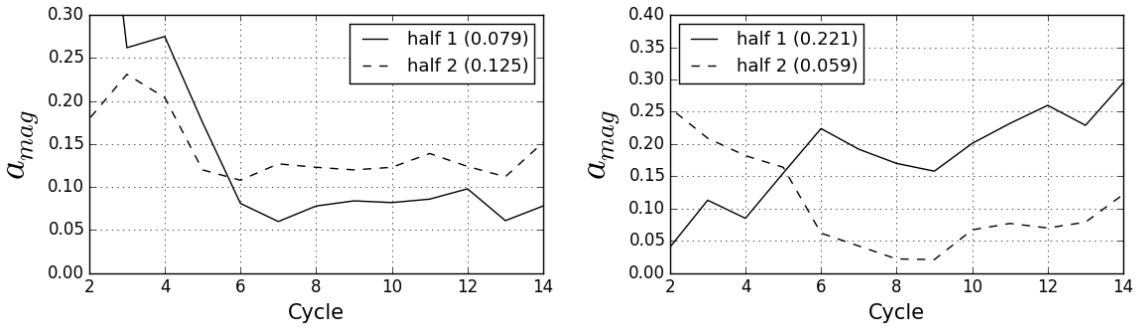

(a) Overview of a_{MAG} factors for GRACE 1.

(b) Overview of a_{MAG} factors for GRACE 2.

Fig. 4.14: Overview of a_{MAG} factors for GRACE 1 and 2 for both halves of each cycle. Values in brackets indicate the average a_{MAG} based on the data from cycles 6-14. The difference between the curves indicates that the magnetic disturbance is stronger when the left side of the satellite is directed towards the Sun. A larger difference further suggests a stronger asymmetry on GRACE 2.

This observation complies with expectations regarding the satellite asymmetry. Cycles 2 to 5 need to be interpreted with caution. A variation of the approach to determine the magnetic field (see chapter 2.3.1) influences the long-period plots of the RDM torque. These changes suggest a different size of a_{mag} in early mission years, clearly visible in the values for GRACE 1. The final quantification of the RDM is based on the results from cycles 6 to 14.
Multiplication of the weighted vector $\vec{m}_0 = (8, \pm 1, \pm 8)^T$ and the long term averages of a_{mag} yield the final approximation of the RDM $\vec{m}_{fin}$. It is important to note, that $\vec{m}_{fin}$ presents an order of magnitude for the respective period rather an absolute value. An overview of the results is shown in table 4.2. The values lie in the range of 0.67 to 2.51 Am^2. This conforms to the typical range for satellites and the maximum RDM of 5 Am^2 specified for GRACE. The aforementioned difference of the asymmetry between GRACE 1 and GRACE 2 becomes apparent when comparing the values of halves 1 and 2 for each satellite. The smaller values 0.7 Am^2 and 0.9 Am^2 that reflect illumination of the right panels are fairly similar in size. The difference of the two higher values is clearly larger. This discrepancy seems too large to be explained solely by inaccuracy of the telemetry. The result suggests an additional effect that increases the RDM when the left panel is generating power. A reasonable explanation is that there was a disturbance originating from the left panel of GRACE 2. The disturbance could be caused by partial failure of one or several panel strings creating an imbalance with regard to the generation of magnetic perturbations. In contrast to the previous conclusion that a panel effect is unlikely to explain the asymmetry on both satellites, here it would only affect one satellite which is a more likely scenario. A quantification of this observation is difficult due to the complex structure of the panel wiring. It is additionally complicated by the non straightforward formation of the magnetic dipole moment. Further investigation on this matter will not be pursued in this analysis and can be addressed in future work.

Half	$\overline{a}_{MAG}$	$\vec{m}_{fin}\,[Am^2]$	$\mid \vec{m}_{fin} \mid$
1	0.079	$(0.63, 0.08, 0.63)^T$	0.90 Am^2
2	0.125	$(1, 0.13, 1)^T$	1.42 Am^2

(a) GRACE 1

Half	$\overline{a}_{MAG}$	$\vec{m}_{fin}\,[Am^2]$	$\mid \vec{m}_{fin} \mid$
1	0.221	$(1.77, 0.22, 1, 77)^T$	2.51 Am^2
2	0.059	$(0.47, 0.06, 0.47)^T$	0.67 Am^2

(b) GRACE 2

Table 4.2: The table shows average values for $\overline{a}_{MAG}$ and the derived approximation of the RDM $\vec{m}_{fin}$. The averages are calculated based on data from cycles 6 to 14. The asymmetric satellite design leads to 36.6% (GRACE 1) and 73.3% (GRACE 2) larger values in phases when the left side is directed towards the Sun.

The above analysis manages to explain the origin of the observed long-period effect. The main conclusions of this section are:

- The long-period effect is caused by the solar radiation pressure and a magnetic torque due to the satellites' RDM.
- The RDM lies within the allowable limit of 5 Am^2.
- Asymmetric design of electronic sub-system causes an asymmetric RDM. It is higher during phases when the left panel is generating power.
- No evidence of a torque caused induced by currents within the panels was found on GRACE 1.
- On GRACE 2 a contribution to the RDM by the left panel may exist, causing a more pronounced asymmetry compared to GRACE 1.

4.3 Short-period effects

4.3.1 Noise reduction in PWM data

In this section the PWM and the respective disturbances are analyzed on a time scale of individual orbits. This should provide further insight on the satellites' typical short-period attitude stability and the formation of magnetic disturbance effects, especially weighting of the RDM vector components. The results should comply with the previous conclusion that currents within the solar panels do not cause noticeable perturbations.
The general approach is similar to the one used in the long-period analysis. The modeled effects

are compared by laying the respective curves on top of one another. Ideally, the progression should match from a qualitative perspective. This means that a positive trend of the attitude error requires a positive disturbance torque in the same time frame.
Analysis of effects on a smaller time scale is complicated by an increased noise in the PWM data. To find data suitable for an analysis of the magnetic disturbance, consideration of two aspects is necessary:

1. Subtraction the long-period influence of the solar radiation from the PWM data.
2. Finding an orbit free from any distortion other than the magnetic field and the Sun.

The SRP effect is subtracted using the LSQ factors a and b, derived in section 4.2 to compare the SRP and the PWM (Fig.4.8). The LSQ data can be found in the appendix A.2.3. The result is exemplified in Figure 4.16. The term 'distortion' in the second headword includes any kind

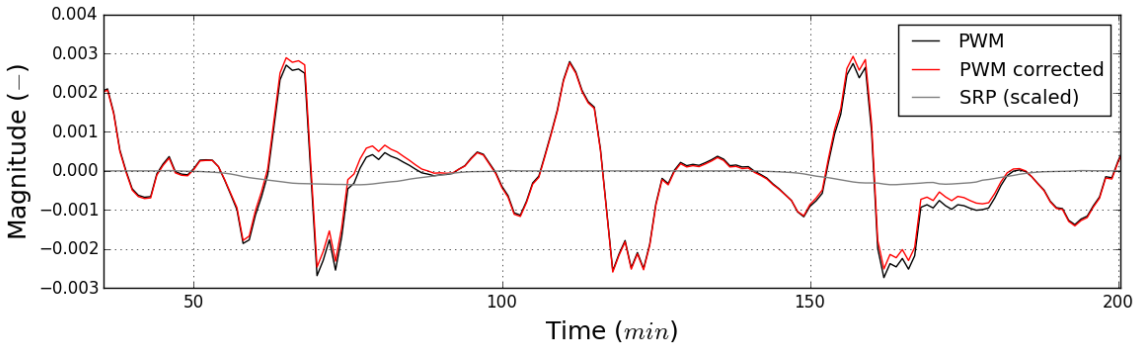

Fig. 4.15: The image illustrates the subtraction of the long-period SRP effect on the PWM. The SRP torque is scaled using the LSQ factors a and b derived in section 4.2.

of anomalous attitude caused by maneuvers or stochastic perturbations. The data of an orbit is free from undesired effects, when the PWM of the same orbit from another point in time has a similar progression. This requires to find a time frame, when the connection line between satellite and Earth passes over the exact same path on the surface. Matching data is obtained by the following steps:

1. Use GPS data to pinpoint a time step when GRACE crosses the equator from southern to northern hemisphere.
2. Calculate the orbital period **U** for the current altitude **h** (equation 4.9).
   - $r_\oplus$ denotes the radius, G the gravitational constant and $M_\oplus$ the Mass of Earth
3. Calculate the number of orbits per day up to the third decimal.
4. Determine the number of full days after which GRACE has completed an even number of orbits (± 0.05).
5. Repeat to receive three sets of corresponding PWM data.

$$U = 2\pi \frac{(r_\oplus + h)^3}{GM_\oplus} \tag{4.9}$$

The result is illustrated in Figure 4.16. It is recognizable from the plot that during certain orbits the data matches well (highlighted frame), but deviates during others. An average PWM curve is determined from the three data sets for the chosen time frame. The derived data is assumed to be free from any unwanted disturbances and is influenced primarily by magnetic effects. In all subsequent plots the MET label indicates the first of the three periods.

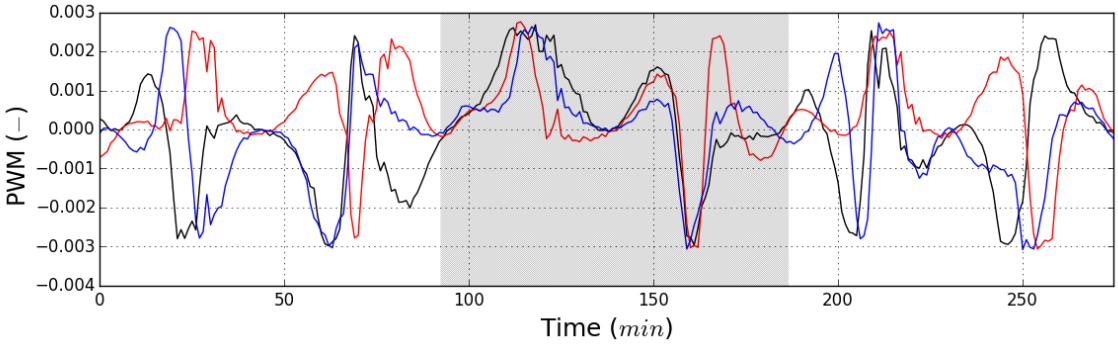

Fig. 4.16: Illustration of three PWM data plots (MET 4328, 4330, 4332). Each plot corresponds with the same path of GRACE relative to Earth. The highlighted frame marks an orbit where all curves match well. This indicates an orbit free of any influences apart from the magnetic field and Sun.

A typical orbit showing the roll attitude of GRACE is presented in Figure 4.17. It includes the PWM (red), the MTQ torque (grey) and the thruster pulses (black bars). Both actuators show only a qualitative progression. The data is smoothed with a Savitzki-Goley filter for easier readability [23]. The height of the bar denotes the pulse length. The PWM displays a consistent positive trend until roughly 1500 sec when the satellite approaches the equator. The increase is caused by a reduced control authority of the MTQ in this region (see 2.3.2). When the error gets close to the dead band (0.003) the thrusters are commanded. Interestingly, in all observed cases the thruster activation is strong enough to not only reduce the error to zero, but tilt the satellite in the opposite direction and, in some cases, reach the opposite dead band. As a consequence, a thruster torque with a reversed sign is commanded. This pattern can be observed in the PWM of close to all orbits. In some orbits the pattern even shows a third period of thruster activation. This is a desired control pattern chosen by mission operators, which was found to have a smaller impact on the payload measurements. In the present case, after the second sequence of pulses the PWM slowly shifts from negative to positive values. Roll stability is typically highest in the vicinity of the magnetic poles. In the second part of the plot this pattern is repeated in a very similar fashion. The symmetric progression of the PWM suggest that a strong magnetic effect induced by the panels is unlikely. Given the fairly long eclipse duration in this period the error would supposedly look different during the Sun phase. The magnetic panel torques #1 and #2 are plotted over the PWM in Figure 4.18 for better traceability of this idea.

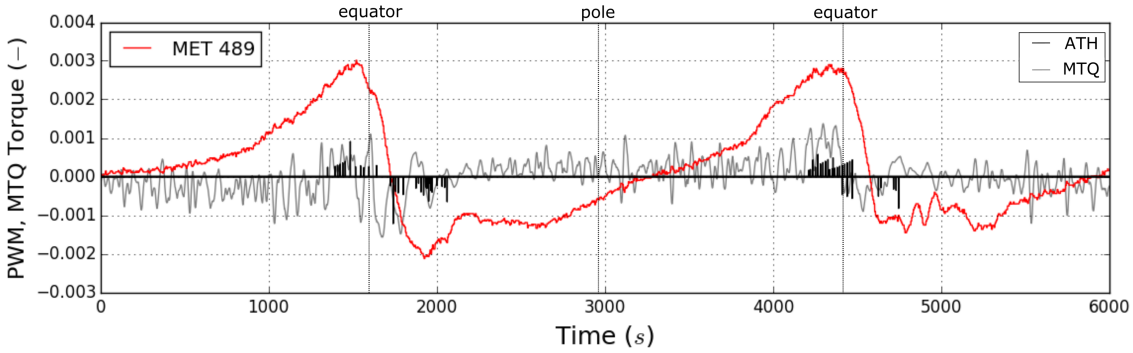

Fig. 4.17: Example of a typical roll attitude (red) progression during one orbit (GRACE 2, MET 489). A positive trend of the PWM indicates a positive disturbance torque. The height of the black bars indicates the duration of the thruster pulse.

4.3.2 Weighting of the RDM vector components

The exclusion of the panel induced torques leaves the RDM as arguably the only major source of disturbances regarding the roll attitude. In a next step a weighting of the RDM components is attempted by matching the curves of the PWM and the RDM. In the observed orbit in Figure 4.17, GRACE 2 is illuminated from the right side. In accordance with the analysis in section 4.2 this requires positive RDM components, $m_y > 0$ and $m_z > 0$. The RDM torque is modeled for different weightings of m_y and m_z to derive a plausible form of the magnetic torque that matches the trend of the PWM. The respective plots are shown in Figure 4.18. Examination of the plots shows a satisfactory progression of the torque for a weighting of roughly $\vec{m} = (1,1,8)^T$ (Fig. 4.18e). In this case, the torque is consistently positive with similar amplitudes in both halves of the orbit and shows a correlation with the trend of the PWM. All examples with a more balanced weighting or a larger m_y component generate a negative torque that does not match the PWM in the second half (Fig. 4.19a - 4.19d). Further increase of m_z shifts the torque to disproportionately high values in the second half (Fig. 4.18f). To confirm this conclusion, an orbit from the same day is inspected for GRACE 1. Illumination of the left panel on GRACE 1 requires reversed signs for both, m_y and m_z. The respective plot is shown in Figure 4.19. The progression in Figure 4.19b matches the trend of the PWM. An exemplary plot with a positive m_y yields a torque that is positive in some parts of the orbit opposed to the negative trend of the PWM.

A variation of the sign of m_y was necessary to achieve a satisfactory progression of the torque in some of the inspected orbits. Presumably, m_y is influenced by more than just the side panels and is subject to fluctuations. Given the smaller weighting of 1, it may change the sign even due to a small contribution of one of the electronic components or the harness. Analysis of a statistically significant number of orbits should reveal a tendency of the sign that complies with the expectations of the long period analysis. To date, GRACE has completed more than 80,000 orbits. Automating the search for distortion-free orbits poses a complex task. Such an analysis goes beyond the scope of this work. It would further require a detailed analysis of the electronic

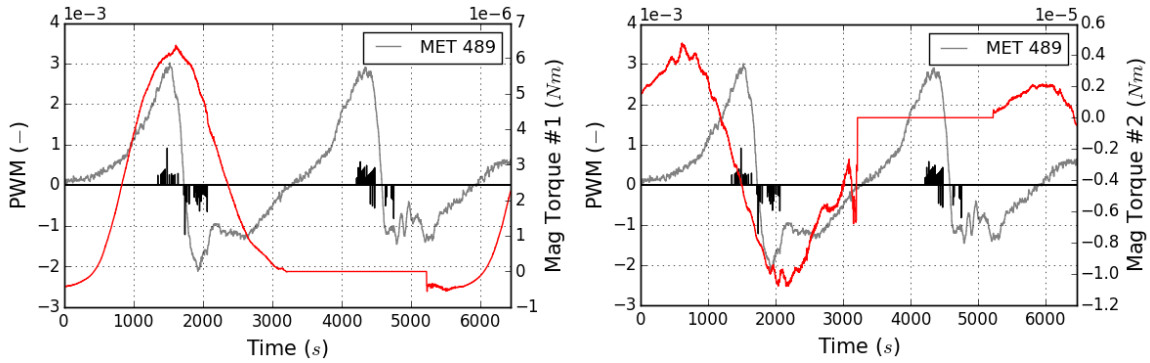

(a) PWM and panel induced torque #1. The model is only suited to explain the progression of the PWM during the first half of the orbit.

(b) PWM and panel induced torque #2. The curves only match during the first half of the orbit. After the second sequence of ATH pulses the PWM grows consistently until the 4440 second mark despite the magnetic torque being zero.

Fig. 4.18: Qualitative comparison of the PWM (MET 489, GRACE 2) and the panel induced torques #1 and #2. The PWM displays a symmetric progression during Sun and eclipse phases, the latter indicated by the torque being zero. This observation argues against that the existence of both disturbance torques.

sub-system including the structure of the harness, as well as flow direction and magnitude of currents.

Analysis of the roll attitude does not provide information on the m_x as it is not required to calculate the roll torque. A parameter study is repeated for the yaw attitude and yaw torque for the above orbit. The results are illustrated in Figure 4.20 for GRACE 2. Comparison of the plots yields reasonable curves for positive m_x, larger by trend compared to m_y (Fig. 4.20c, 4.20d). The enlarged X-component generates a largely negative torque in the observed time frame that corresponds to the negative trend of the PWM visible in the intervals (1300s-2000s), (3000s-3900s), (4200s-4900s). Choice of a negative m_x yields a mostly positive torque that does not match the attitude error. A very similar result is derived from the analysis of the respective orbit on GRACE 1 (Fig. 4.20). The error shows a negative trend despite rotation of the satellite. The best fit is achieved assuming a positive m_x.
A more optimistic weighting of $m_x = 8$ (potentially larger disturbance) is chosen in first approximation after comparison with selected other orbits (see appendix A.2.6). Note that the yaw attitude may differ from roll. Influences on the yaw motion haven't been analyzed in depth. The progression is influenced more frequently by ATH pulses.

The short-period analysis of the PWM and the respective disturbance effects illustrates the complexity of the topic. A comparison of PWM data from different days showed a strong deviation of the individual curves in most parts of the observed periods, even though the data describes the attitude in the same location. Interpretation of the attitude error has to be made with great care. The search for suitable, distortion-free orbits is very time-consuming and could

not be automated in the scope of this work. An extensive, statistically significant study may be attempted in a future work. The derived results are sufficient to estimate the order of magnitude of the magnetic dipole moment.
The following conclusions can be drawn from the analysis:

- The sign of the m_z component complies with the condition derived in chapter 4.2 that the SRP and magnetic torques must have the same effective direction.
- The sign of m_y may vary according to an unknown principle in some of the observed cases.
  - Analysis of a larger number of orbits should confirm statistically that the sign follows the expectation in the majority of the orbits.
- m_z is weighted by a factor **8** compared to m_y.
- m_x is positive and presumably larger compared to m_y. An optimistic weighting by factor **8** was chosen.

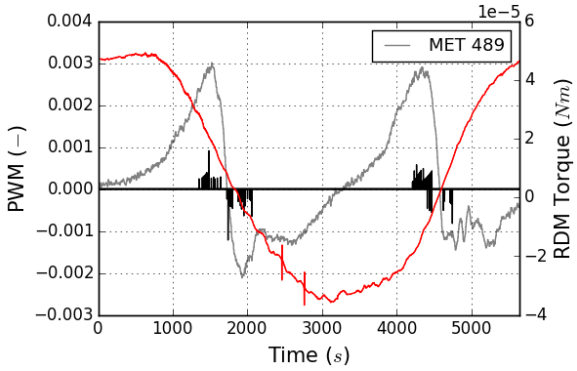

(a) RDM torque for $\vec{m} = (1,1,1)^T$. A balanced weighting of m_y and m_z induces a torque that fluctuates smoothly about zero. In the second half of the orbit the PWM is positive which requires a positive disturbance torque.

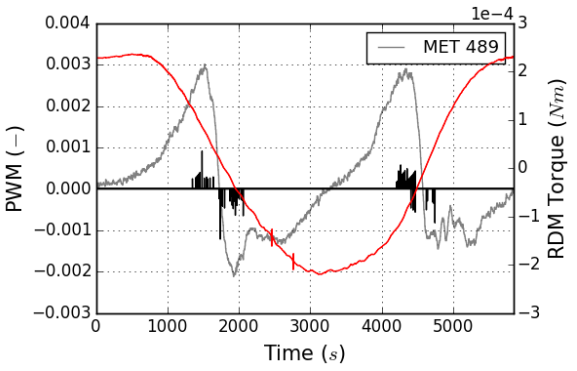

(b) RDM torque for $\vec{m} = (1,5,1)^T$. A weighting of m_y causes no significant changes compared to a balanced weighting. A positive PWM in the second half of the orbit can't be induced by a negative disturbance.

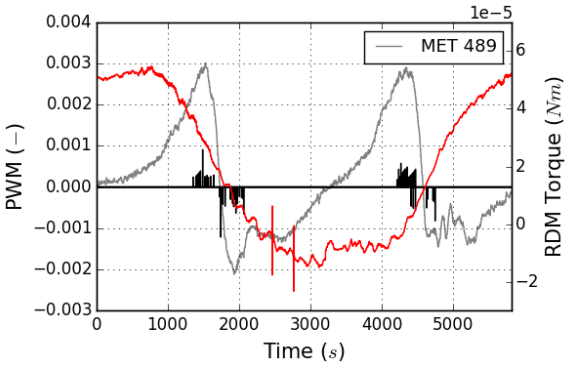

(c) RDM torque for $\vec{m} = (1,1,3)^T$. Light emphasis on the m_z component reduces the negative values of the torque compared to an even weighting.

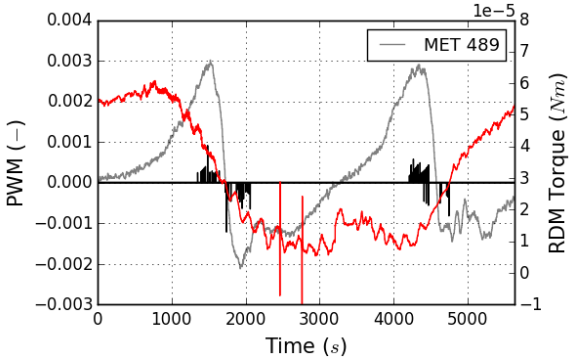

(d) RDM torque for $\vec{m} = (1,1,5)^T$. The torque is consistently positive, but with different amplitudes in the two halves of the orbit. This suggests the right direction for the weigthing.

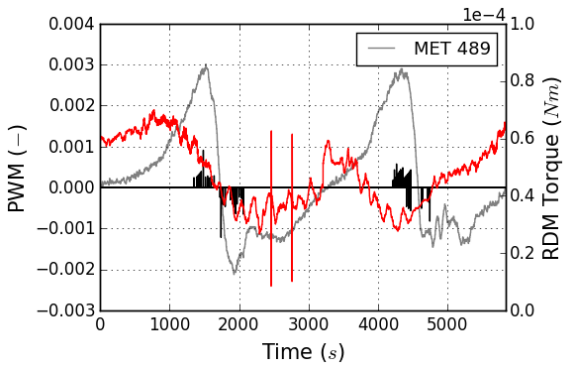

(e) RDM torque for $\vec{m} = (1,1,8)^T$. The torque is positive throughout the observed period. A correlation with the positive trend of the PWM indicates a realistic weighting.

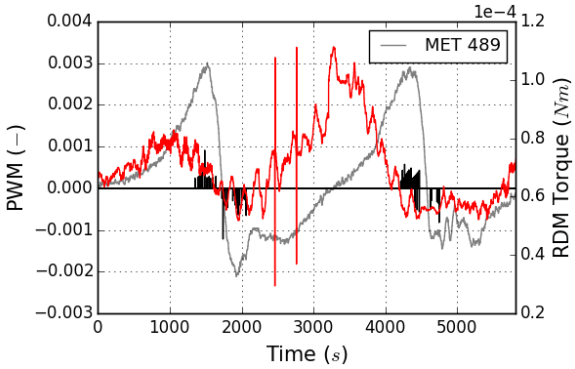

(f) RDM torque for $\vec{m} = (1,1,12)^T$. Further increase of m_z pushes the torque to more positive values. Given the smooth form of the PWM a stronger disturbance in the second half of the orbit is unliekly.

Fig. 4.18: Qualitative comparison of the PWM (grey) and RDM roll torque (red) for different weightings of $\vec{m}$ (GRACE 2, MET 489). A realistic weighting of the components is indicated by a matching progression of the curves. A positive trend of the PWM requires a positive torque.

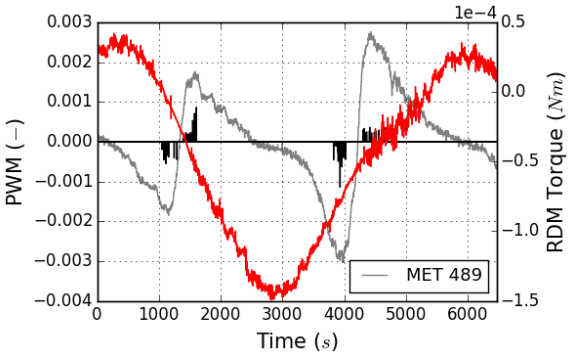

(a) RDM torque for $\vec{m} = (1,1,-8)^T$. The torque shows partially positive values that do not match the trend of the PWM.

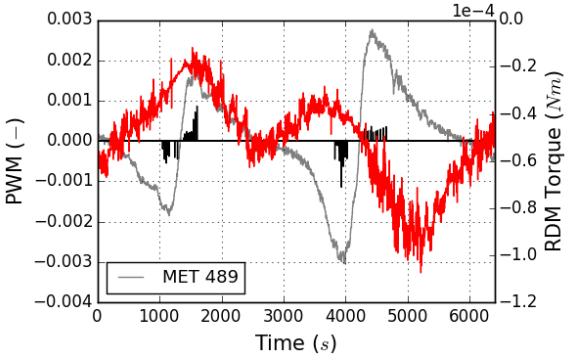

(b) RDM torque for $\vec{m} = (1,-1,-8)^T$. The torque is negative throughout the observed period in correspondence with the negative trend of the PWM.

Fig. 4.19: Comparison of the PWM (grey) and RDM roll torque (red) for different weightings of $\vec{m}$ (GRACE 1, MET 489). Illumination of the right panel induces a negative m_z component. A negative m_y generates a torque that matches the negative trend of the PWM.

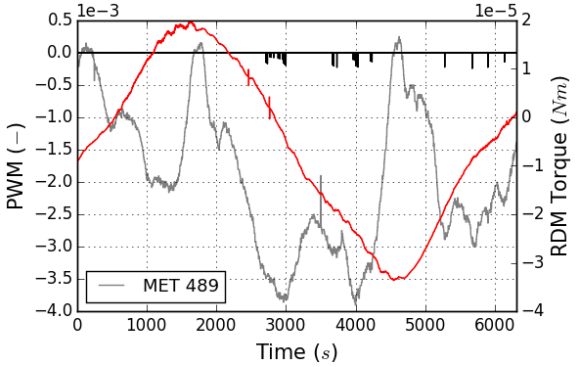

(a) RDM torque for $\vec{m} = (1,1,8)^T$. The positive values of the torque between 500s and 2800s does not match the partially negative trend of the PWM.

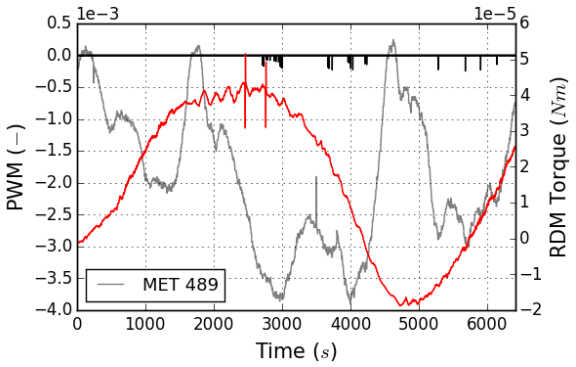

(b) RDM torque for $\vec{m} = (-3,1,8)^T$. A negative m_x induces a largely positive torque that does not follow the trend of the PWM.

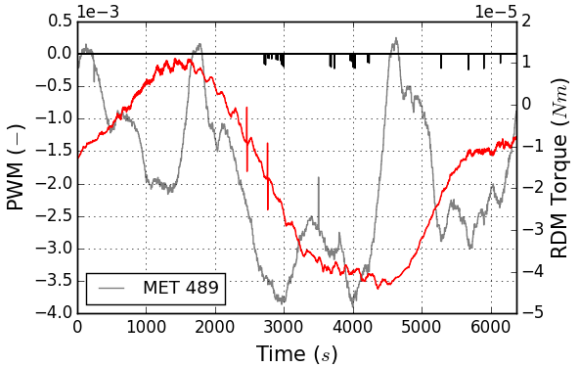

(c) RDM torque for $\vec{m} = (3,1,8)^T$. A slightly positve weighting of m_x reduces the interval in which the torque is positive.

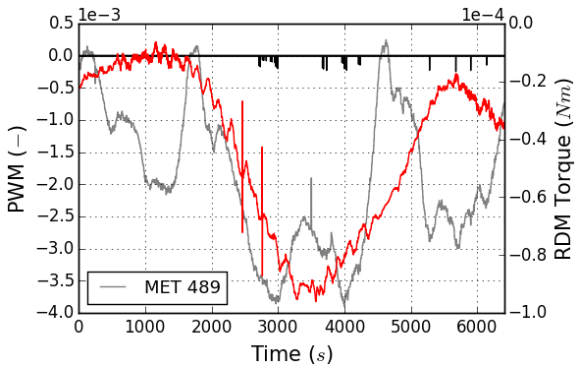

(d) RDM torque for $\vec{m} = (8,1,8)^T$. Stronger weighting induces a torque ≤ 0. The progression complies with the negative trend of PWM.

Fig. 4.20: Qualitative comparison of the PWM (grey) and RDM yaw torque (red) for different weightings of $\vec{m}$ (GRACE 2, MET 489). The yaw attitude provides information on m_x. The PWM shows a pronounced negative trend with exception of the interval (1500s-1800s). The interpretation is complicated by a more frequent thruster activation compared with roll.

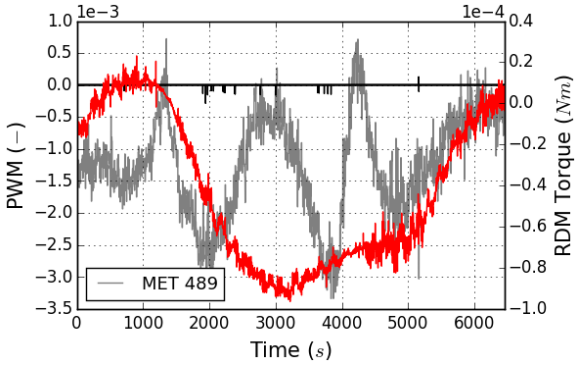

Fig. 4.21: Qualitative comparison of the PWM (grey) and RDM yaw torque (red) for $\vec{m} = (8, -1, -8)$ (GRACE 1, MET 489). The yaw attitude provides information on m_x. The sign of the torque matches the negative trend of the PWM.

5 Conclusion

This work investigates disturbance forces acting upon the GRACE satellites. The analysis provides a detailed explanation of the observed long-period disturbance in the roll attitude stability, which causes an unbalanced activation of the attitude thrusters. Understanding this effect is highly interesting in several ways. Firstly, all attitude perturbations have a direct influence on payload measurements and the accuracy of the gravitational field model. Secondly, knowledge of the effect can be used in order to optimize AOCS control. The compensation of the disturbance requires more frequent thruster actuation and hence additional consumption of fuel. The GRACE mission has shown that efficient usage of the limited resource is crucial for a long mission duration. Thirdly, long-term behavior of the effect provides insight on the robustness of the satellite design. The three aspects are all the more relevant in view of the GRACE Follow-On (GFO) mission, which is based on a very similar mission concept and satellite build. On the hand, this means that the GFO satellites will experience the same cyclical disturbance force. On the other hand, the similarity allows a direct transfer of knowledge acquired within the scope of GRACE. Hence, necessary measures can be taken to guarantee the best possible compensation of the disturbance.

The in-depth analysis shows that the periodic effect is caused by the solar radiation pressure and a magnetic torque. The latter originates from the satellites' residual magnetic dipole moment (RDM) $\vec{m}$. A Fourier spectrum of the PWM confirms that the roll attitude is determined by these two effects. A comparison of the angular momentum applied by the two AOCS actuators and the Sun allows to estimate the average magnitude of the magnetic dipole moment. The calculation shows a variation from 0.9 to 1.4 Am^2 on GRACE 1 and from 0.7 to 2.5 Am^2 on GRACE 2. The results are reasonable and satisfactory as all values lie in a typical region for LEO satellites and stay below the allowed maximum of 5 Am^2 specified for GRACE. The discrepancy within both satellites follows from an asymmetric structure of the electronic hardware and harness inside the bus. Larger disturbances can be observed when the left solar panel is directed towards the Sun. This phenomenon can be explained by the contribution of the solar panels to individual components of $\vec{m}$. Contributions of the left panel most likely add up with contributions of other electronic hardware, but cancel each other out when the right panel is powered. A plausible weighting of the components has been obtained by comparing the RDM torque and the PWM on the basis of individual orbits. In this context, plausibility implies a qualitative match of the curves, e.g. a positive trend of the attitude error requiring a positive disturbance torque. The final vector $\vec{m} = (8, \mp 1 \mp 8)^T$ suggests that the X and Z-components are larger compared to the Y-component. The X and Z-components change their sign, depending on the side panel that is currently illuminated. It was not possible to conduct a statistically significant study with a more

extensive amount of orbits due to the complexity of the problem and the enormous time effort necessary to search for suitable orbits.

Another focus of the analysis was to evaluate the potential existence of magnetic disturbances that originate particularly from currents within the solar panels. Such effects may result from imperfect design and manufacturing processes. Alternatively, they can be caused by partial failure of the panel as a consequence of aging processes or external impact. In both cases an unbalanced current flow will exert a force on the satellite. Investigation yields no indication of a panel induced torque on GRACE 1. Overall, the magnetic effect shows no significant change over the course of the mission, which allows the conclusion of well functioning panels.
On GRACE 2 the chance of a bias on the left panel exists that could explain the increased magnetic dipole moment of 2.5 Am^2 during illumination of the left side. The magnetic effect shows a slight increase starting in 2010 that may reflect the failure of individual strings of the solar panel. Proof of this conclusion based on satellite data has yet to be provided.

Aside from the last observation, the analysis displays a stable behavior on both satellites, especially regarding the roll attitude. This is a very good result, considering the long duration of the mission.

Future work

The presented results lay good groundwork for subsequent work. First and foremost, analysis of the yaw and pitch attitude can be conducted to complement and extend the achievements of this work. Naturally, the other axes require the consideration and modeling of additional disturbance forces.

The short-period analysis in this work is based on a limited number of orbits due to the high expenditure of time necessary for the observation of individual orbits. To gain more detailed insight on the characteristics of the magnetic dipole moment a more extensive amount of orbital data needs to be examined. A larger amount of data may allow drawing statistically significant conclusions that could confirm the results.

Finally, it is highly recommended to transfer the acquired results to the upcoming GRACE Follow-On mission. An estimation has shown that so far about 2.7 kg of fuel have been used on each satellite for the compensation of the long-period effect. In the current phase of the mission, GRACE 2 has about 3 kg of fuel left, which poses a critical issue for the remaining life expectancy of the satellite and the whole mission. Possibilities should be evaluated to relieve the thrusters as far as possible by allocating the compensation to the magnetic torque rods. The technical challenges with GRACE in recent years demonstrate that sufficient fuel reserves in an advanced mission phase are crucial for the continuation of the mission. The possible savings are substantial in view of a long and successful GFO mission.

Bibliography

[1] I. MARSON. A Short Walk along the Gravimeters Path. In: International Journal of Geophysics 2012.doi: 10.1155/2012/687813 (2012).

[2] J. M. GOODKIND. The superconducting gravimeter. In: Review of Scientific Instruments 70.doi: 10.1063/1.1150092 (1999).

[3] G. Veis C. A. LUNDQUIST. Geodetic Parameters for a 1966 Smithsonian Institution Standard Earth. In: Sao special report #200, Smithsonian Astrophysical Observatory (1966).

[4] B. Tapley et AL. The gravity recovery and climate experiment: Mission overview and early results. In: Geophysical Research Letters 31 (2014), p. 09607.

[5] H. Luer CH. REIGBER P. Schwintzer. The CHAMP geopotential mission. In: Bollettino Di Geofisica Teoretica Ed Applicata 40.3-4 (1999), pp. 285–289.

[6] Gravity Field and Steady-State Ocean Circulation Mission. Report for mission selection of the four candidates Earth Explorer mission ESA SP-1233. Tech. rep. European Space Agency, 1999.

[7] K. Nicklaus et AL. Optical Bench of the Laser Ranging Interferometer on GRACE Follow-On. In: International Conference of Space Optics (2014).

[8] O. BAUR. Greenland mass variation from time-variable gravity in the absence of GRACE. In: Geophysical Research Letters 40.16 (2013), pp. 4289–4293.

[9] Artist's concept of Gravity Recovery and Climate Experiment. NASA/JPL-Caltech. 2002. URL: https://www.nasa.gov/mission_pages/Grace/multimedia/gallery-index.html#lowerAccordion-set1-slide6 (visited on 07/05/2017).

[10] J. Herman et AL. Life with a weak Heart. Prolonging the GRACE Mission despite degraded Batteries. Tech. rep. SpaceOps 2012, Stockholm, Sweden, 2012.

[11] B. DACHWALD. Raumfahrzeugbau II Vorlesungsskript. RWTH Aachen, 2010.

[12] GSOC internal information from software documentation. Not open for public disclosure.

[13] J. HERMAN. Attitude control for GRACE: the first low-flying satellite formation. Tech. rep. ESA SP-548: 18th International Symposium on Space Flight Dynamics.

[14] F. PRIEMDAHL. The Fluxgate Magnetometer. In: Journal of Physics E: Scientific Instruments 12 (1979), pp. 241–253.

[15] International Geomagnetic Reference Field. International Union of Geodesy and Geophysics. 2014. URL: https://www.ngdc.noaa.gov/IAGA/vmod/igrf.html (visited on 22/12/2014).

[16] Department of Defense. World Geodetic Syste, 1984. National Imagery and Mapping Agency. 2000. URL: http://earth-info.nga.mil/GandG/publications/tr8350.2/wgs84fin.pdf (visited on 06/07/2017).

[17] A. Pickles J. L. JORGENSEN. fast and robust pointing and tracking using a second generation star tracker. In: proceeding of the International Society for Optical Engineering 3351 (1998), pp. 51–61.

[18] J. Wertz et ALL. Space Mission Engineering: The New SMAD. Microcosm Press, 2011.

[19] A. Milani et ALL. Non-gravitational perturbations and satellite geodesy. ISBN 0-85274-538-9. Adam Hilger Ltd., Bristol, UK, 1987.

[20] U. Hugentoblerl O. MONTENBRUCK P. Steigenberger. Enhanced Solar Radiation Pressure Modeling for Galileo Satellites. In: J. Geod 89 (2015), pp. 283–297.

[21] A. DAVIS. Technical Memorandum - 141110. Estimated torques on the satellites. University of Texas, Center for Space Research. 2014. URL: InternalEmail.

[22] S. DeLapp T. STERN. Techniques for Magnetic Cleanliness on Spacecraft Solar Arrays. Tech. rep. 2nd International Energy Conversion Engineering conference, doi: 10.2514/ 6.2004-5581, 2004.

[23] M. Golay A. SAVITZKY. Smoothing and differentiation of Data by Simplified Least Squares Procedures. In: Annual Summer Symposium of Analytical Chemistry 36.8 (1964), pp. 1627–1639.

[24] J. Tukey W. COOLEY. An Algorithm for the Machine Calculation of Complex Fourier Series. In: Math. Comp. 19 (1965), pp. 297–301.

[25] W. Press et AL. Numerical Recipes. The Art of Scientific Computing. Cambridge Univesity Press, 1986.

A Appendix

A.1 GRACE Mission

Cycles overview

Table A.1 provides an overview of all GRACE cycles. A cycle has a period of approximately 321.6 days and is the equivalent of a solar year for GRACE. The duration of 365.25 days is shortened due to the drift of the GRACE orbit (progression of the RAAN) with a period of 8 years. Most calculations are based on data from cycles 6 to 14 which denote a calm phase of the mission, free from swaps and without major technical difficulties. Cycles 15 to 17 are excluded from most analyses due to problems with the battery that led to many operational measures. This results in strong fluctuations of the attitude data that do not allow meaningful analysis regarding the problems this work focuses on.
All performed swaps are noted in the table. The first swap was performed to relieve the front facing MWI (Microwave Instrument) of the chasing satellite from atmospheric particle and radiation loads. Starting in 2014 swaps are performed every 160 days as a necessary consequence of star camera problems.

Cycle	Start				Swap (MET)
	MET	YEAR	DOY	DATE	
1	1	2002	76.5	17.03	
2	321	2003	32.5	01.02	
3	641	2003	353.5	18.12	
4	961	2004	308.5	03.11	
5	1284	2005	264.6	21.09	1365
6	1605	2006	220.6	08.08	
7	1926	2007	176.6	25.06	
8	2247	2008	131.6	11.05	
9	2569	2009	87.7	29.03	
10	2890	2010	43.7	13.02	
11	3212	2010	364.7	01.01	
12	3533	2011	320.7	18.11	
13	3852	2012	275.7	02.10	
14	4174	2013	231.8	20.08	
15	4495	2014	187.8	07.07	4516, 4656
16	4816	2015	143.8	24.05	4834, 4964
17	5137	2016	98.8	09.04	5147, 5294
18	5458	2017	54.8	24.02	

Table A.1: Overview of all GRACE cycles with corresponding MET (Mission Elapse Time), year, DOY (Day Of Year) and date. All performed swaps are included.

Orbit

The following images illustrate typical characteristics of the GRACE orbit. Figure A.1 shows the orientation of the orbit plane relative to the Sun for a low and a high β′ angle. The drift of the orbit due to the progression of the RAAN is illustrated in Figure A.2.

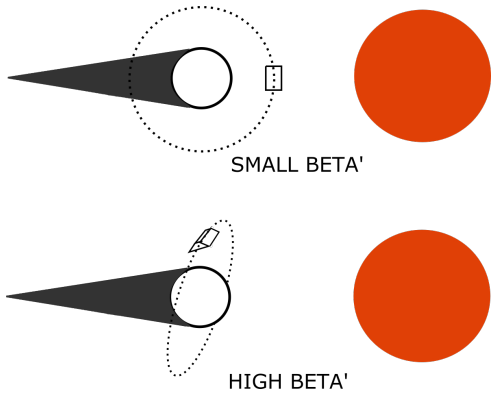

Fig. A.1: rientation of the orbit relative to the Sun for a low (top) and high (bottom) β′. Phases with low β′ are characterized by long eclipses. The satellites experience full-sun orbits for β′ >+70 deg or lower than <-70 deg.

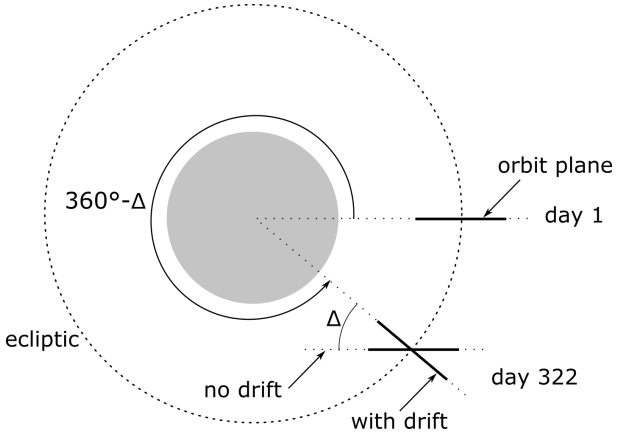

Fig. A.2: Illustration of the RAAN progression of the GRACE orbit. The orbital plane completes a revolution relative to the Sun in 321.6 days. This characteristic period is referred to as cycle.

Thruster locations

The mounting locations of all GRACE attitude thrusters are listed in table A.2. All coordinates mark a position in the satellite body frame. The number in the 'Thruster' column denotes the branch number (1/2) and the number of the thruster (1-6). **Y** (Yaw), **P** (Pitch), **R** (Roll) and the preceding sign indicate the direction of the applied torque.

Thruster		Position [mm]		
		x	y	z
11	-Y	-1450	-719	0
12	+P	-1450	0	-444
13	+Y	-1450	719	0
14	-P	-1450	0	444
15	-R	0	-970	+300
16	+R	0	-467	-300

(a) Branch 1

Thruster		Position [mm]		
		x	y	z
21	-Y	1450	719	0
22	+P	1450	0	275
23	+Y	1450	-719	0
24	-P	1450	0	-444
25	-R	0	+467	-300
26	+R	0	+970	+300

(b) Branch 2

Table A.2: Mounting location of the roll attitude thrusters.

A.2 Complementary data and figures

A.2.1 Disturbance models

This appendix illustrates complementary plots of the SRP and panel induced torques modeled in chapter 3. Figure A.3 illustrates the solar radiation torque about the yaw and pitch axes. Figure A.4 shows the panel induced torques #1 and #2 about the yaw and pitch axes.

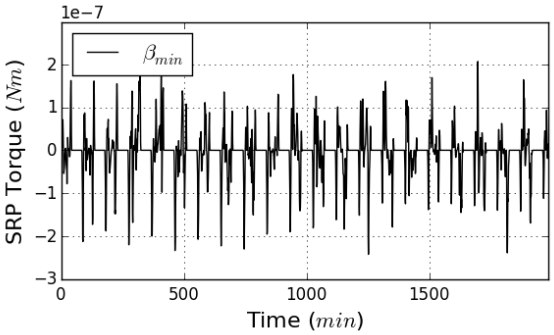

(a) SRP torque about the yaw axis for a low β′ angle. The phase is characterized by long eclipses. The torque is small and fluctuation about the X-axis due to a balanced out force on both sides of the satellite.

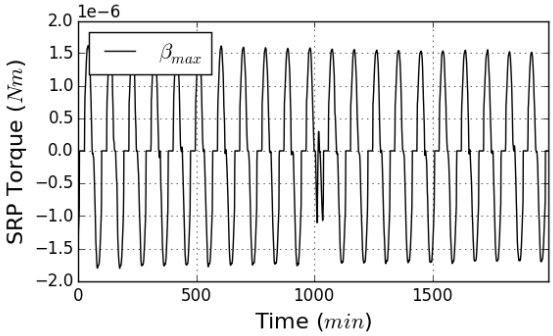

(b) SRP torque about the yaw axis for a high β′ angle. The phase is characterized by short eclipses. The torque displays a smooth progression with a small anomaly in the center of the plot.

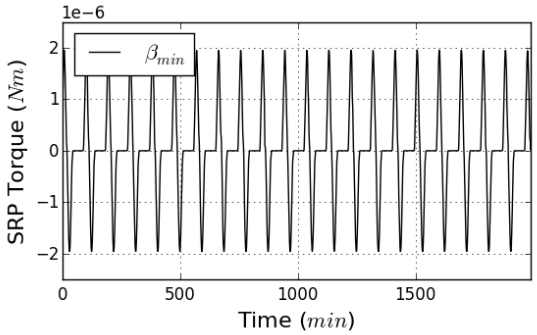

(c) SRP torque about the pitch axis for a low β′ angle. The phase is characterized by long eclipses. The torque displays a smooth progression with positive and negative values.

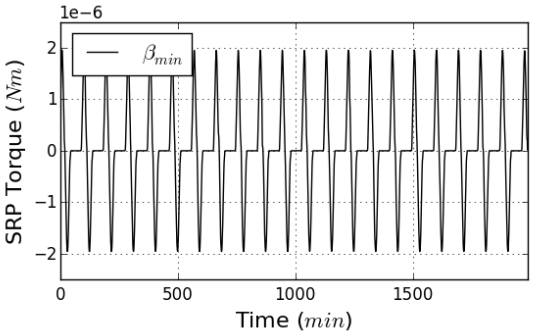

(d) SRP torque about the pitch axis for a high β′ angle. The phase is characterized by short eclipses. The torque displays a smooth progression with positive and negative values, but an order of magnitude smaller compared to the pitch torque during a phase with a low β′.

Fig. A.3: Illustration of the modeled SRP torque about yaw and pitch axes with GRACE telemetry as input.

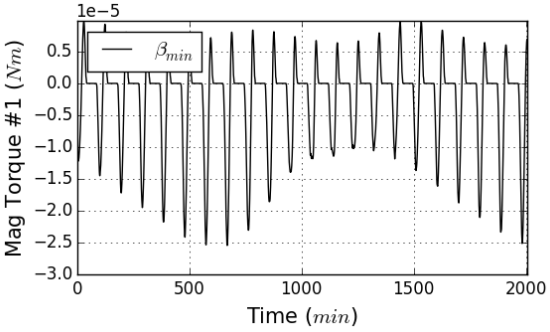

(a) Panel induced torque #1 about the yaw axis for a low β′ angle. The phase is characterized by long eclipses.

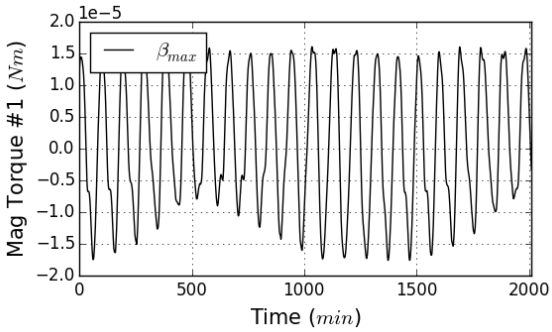

(b) Panel induced torque #1 about the yaw axis for a high β′ angle. The phase is characterized by short eclipses.

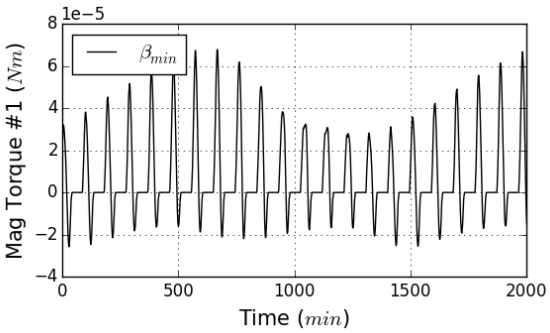

(c) Panel induced torque #1 about the pitch axis for a low β′ angle. The phase is characterized by long eclipses.

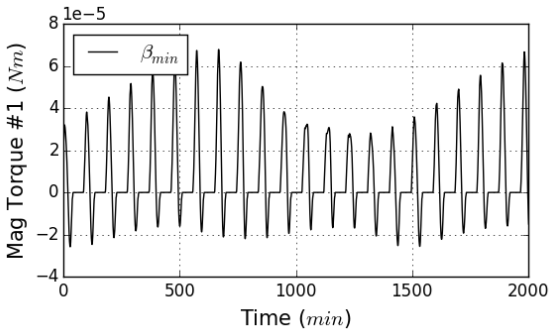

(d) Panel induced torque #1 about the pitch axis for a high β′ angle. The phase is characterized by short eclipses.

Fig. A.4: Illustration of the modeled torque induced by the solar panels about yaw and pitch axes. GRACE telemetry is used as input. The torque may be generated due to disadvantageous aging behavior or damaged the panel. This could create an imbalance within the panel regarding the induction of magnetic effects. No yaw or pitch torque is created for model #2.

A.2.2 Fast Fourier spectra

Figures A.5 shows the Fast Fourier spectrum of the magnetic field vector $\vec{B}$ that shows the origin of the characteristic peak pattern visible in the spectra of the PWM and all torque models related to the magnetic field.

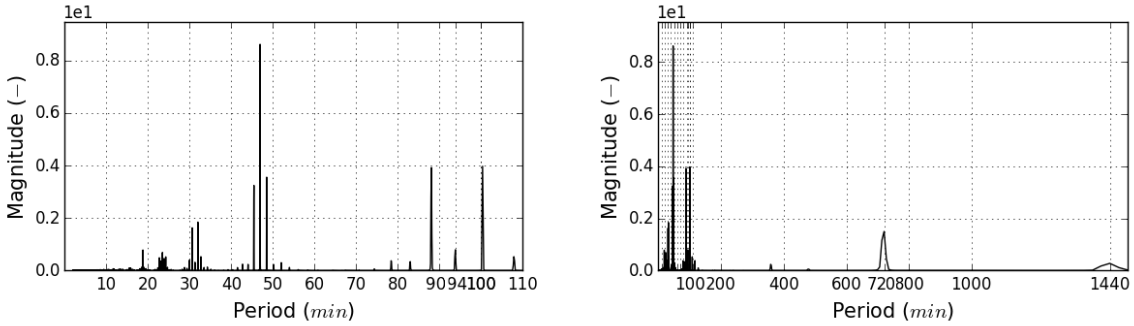

Fig. A.5: Fast Fourier spectrum of the magnetic field vector $\vec{B}$. The characteristic patterns of peaks visible at the orbital ($\approx$ 94 min) and half orbital ($\approx$ 47 min) periods can be attributed to the dynamics of the magnetic field. The patterns are recognizable in the PWM and all effects related to the magnetic field including the MTQ torque.

Figure A.6 shows the GRACE 2 frequency spectra of the PWM in all three axes. The characteristic periods (peaks) in the PWM the originate from the disturbance forces influencing the respective attitude.

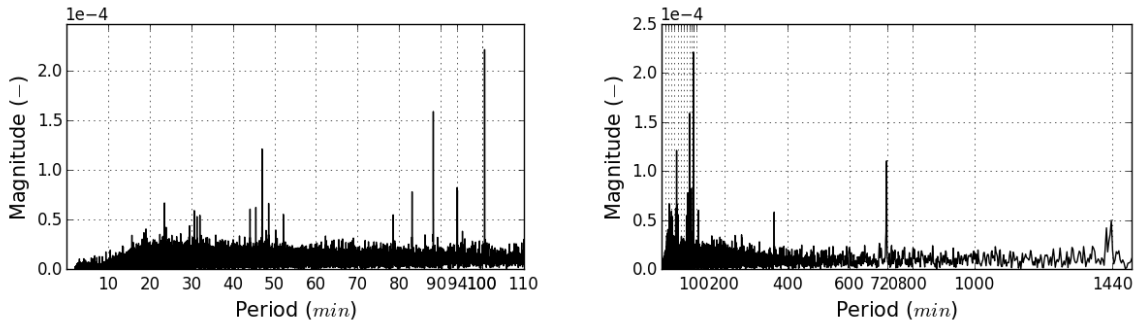

(a) Spectrum of the PWM for the Roll attitude. A pronounced pattern of peaks is visible at the orbital ($\approx 94 min$) and half orbital ($\approx 47 min$). Less distinct repetitions are visible at smaller periods. Further periodicities are noticeable at the 720 min (half a day) and 360 min marks. A 1440 min (full day) peak is indicated but small compared to the others.

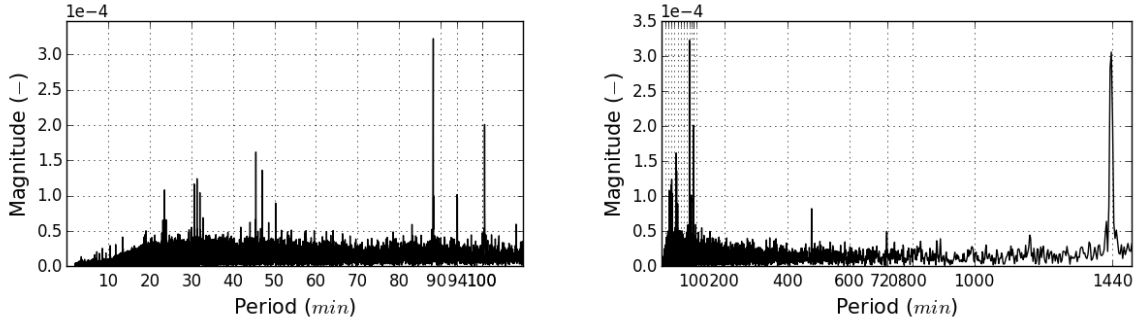

(b) Spectrum of the PWM for the Yaw attitude. The distribution of peaks closely resembles that in roll. The peak at the orbital period ($\approx 94 min$) seems to be slightly less pronounced. A very disitnct peak is located at the 1440 min (full day) mark. The 720 min peak is very small compared to roll.

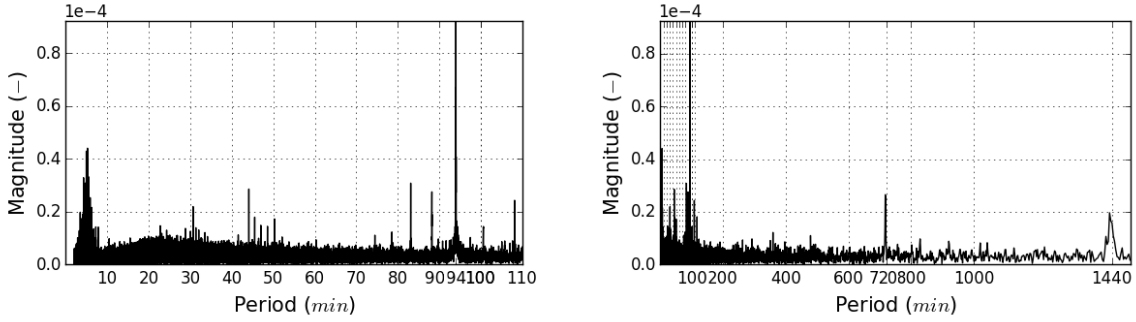

(c) Spectrum of the PWM for the Pitch attitude. The strongest periodicity is visible at the orbital period ($\approx 94 min$) mark. It is surrounded by a sequence of smaller peaks. The peak at the half orbital period is less pronounced compared to the other axes. A cluster of high-frequent peaks ($< 10 min$) is noticeable that doesn't appear in roll and yaw. Between 10 and 25 min an anomaly is visible that has no physical significance.

Fig. A.6: Fast Fourier spectra of the PWM in all three axes derived from 322 days of data (cycle 4, GRACE 2). All peaks indicate periodicities within the effects that influence the respective attitude.

A.2.3 PWM and SRP least squares fit

Table A.3 sums up the scaling factors derived from the fitting of SRP and PWM using a least squares fit (GRACE 1 and 2). The factors are used in the analysis of short-period effects to subtract the impact of the solar radiation from the PWM. The least squares algorithm (LSQ) has the form:

$$X_{LSQ} = a + b \cdot X \tag{A.1}$$

The listed chi^2 values are all $<< 1$ which indicates a good quality of the fit.

Cycle	a	b	chi^2
1	9.11E-05	64.81	2.06E-06
2	2.91E-05	71.07	2.76E-06
3	3.66E-05	97.09	3.09E-06
4	1.38E-05	118.83	2.79E-06
5	2.41E-05	95.3	2.34E-06
6	2.30E-05	88.72	2.26E-06
7	2.03E-05	94.47	2.53E-06
8	2.47E-05	78.54	1.99E-06
9	1.92E-05	93.15	2.20E-06
10	1.99E-06	75.22	2.08E-06
11	8.62E-06	85.88	1.96E-06
12	6.40E-06	98.15	2.91E-06
13	8.57E-06	77.09	2.83E-06
14	3.52E-05	86.32	1.84E-06
15	3.75E-05	160.47	5.49E-06
16	8.17E-05	161.8	7.34E-06

(a) GRACE 1

Cycle	a	b	chi^2
1	1.19E-05	76.92	6.33E-06
2	2.22E-06	115.33	4.97E-06
3	4.88E-05	88.8	3.13E-06
4	1.97E-05	115.59	2.90E-06
5	2.23E-05	91.15	2.20E-06
6	-2.96E-05	88.5	2.02E-06
7	-1.45E-05	83.16	2.41E-06
8	-1.15E-05	69.89	2.10E-06
9	-1.69E-05	69.96	2.19E-06
10	-5.83E-06	66.71	1.85E-06
11	-1.49E-05	78.87	2.14E-06
12	-6.44E-06	77.1	1.93E-06
13	-8.86E-06	75.47	2.53E-06
14	-3.29E-05	75.85	2.40E-06
15	3.35E-05	155.9	8.75E-06
16	9.03E-05	108.2	1.01E-05

(b) GRACE 2

Table A.3: Overview of scaling factors derived from a least squares fit of the SRP and PWM long-period plots.

Figures A.7 and A.8 show the histograms derived from the LSQ fit of SRP and PWM. A Gaussian distribution of the errors indicates that no systematic/period effects are hidden in the PWM data. In other words that the residues show a random distribution. Deviation from the Gaussian bell form is partly due to fluctuations in the PWM data caused by maneuvers, mode switches etc. Another reason may be the magnetic dipole moment whose real form is not exactly known.

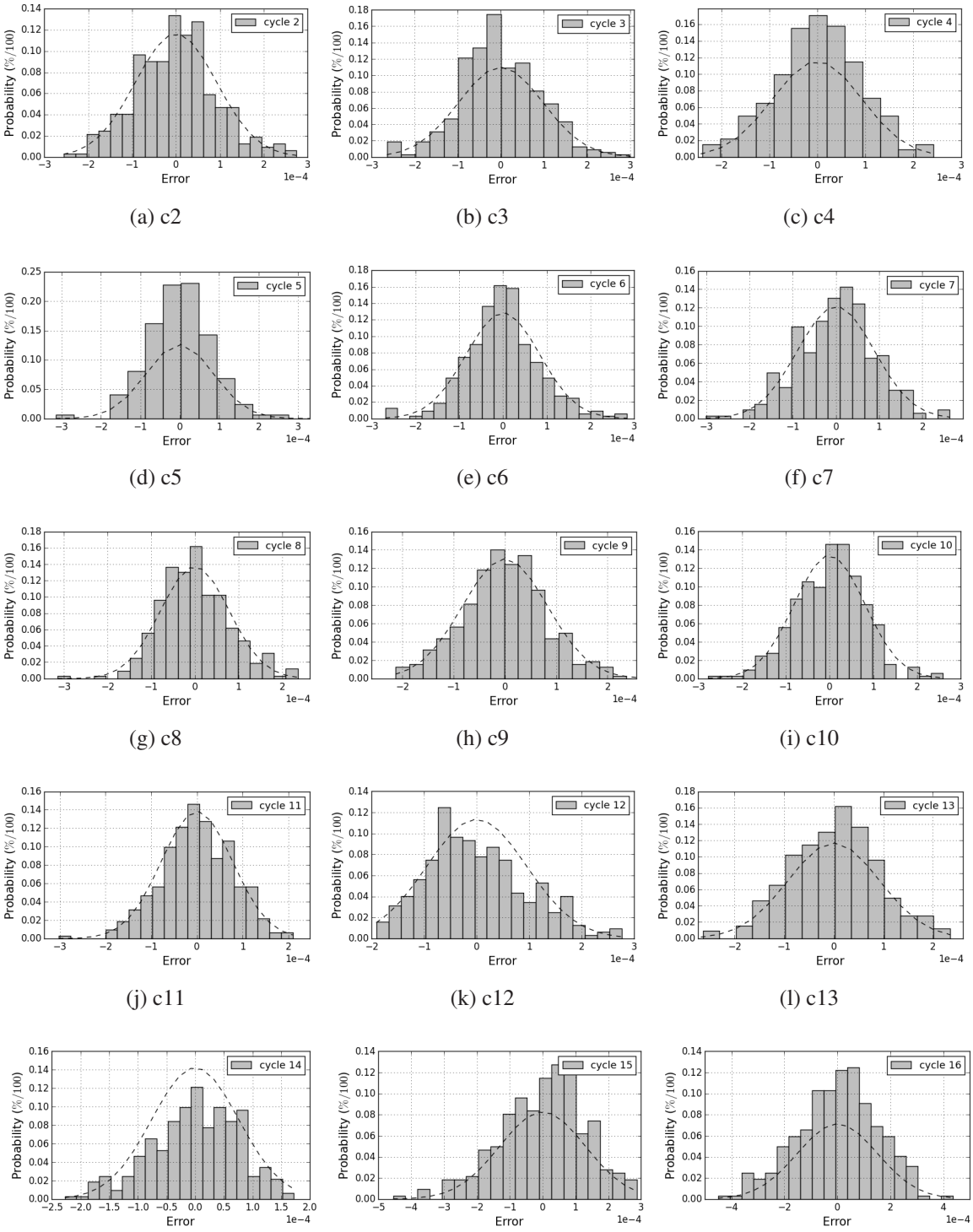

(a) c2 (b) c3 (c) c4

(d) c5 (e) c6 (f) c7

(g) c8 (h) c9 (i) c10

(j) c11 (k) c12 (l) c13

(m) c14 (n) c15 (o) c16

Fig. A.7: The histograms show the distribution of the residues derived from the least squares fit of PWM and SRP. A Gaussian form indicates a good fit of the to curves. See the above text for details. The sub captions denote the cycle. GRACE 1.

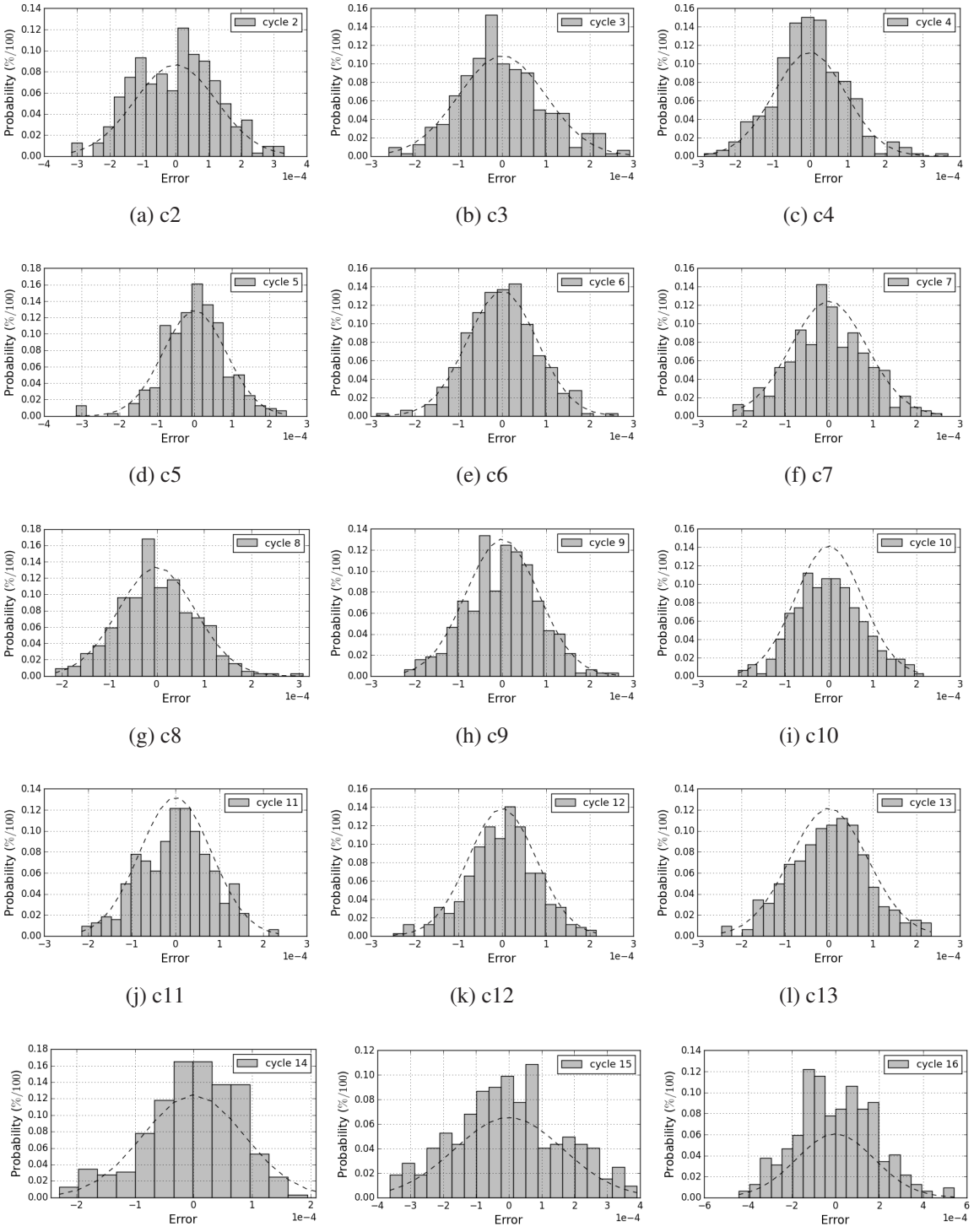

(a) c2 (b) c3 (c) c4

(d) c5 (e) c6 (f) c7

(g) c8 (h) c9 (i) c10

(j) c11 (k) c12 (l) c13

(m) c14 (n) c15 (o) c16

Fig. A.8: The histograms show the distribution of the residues derived from the least sqaures fit of PWM and SRP. A Gaussian form indicates a good fit of the to curves. See the above text for details. The sub captions denote the cycle. GRACE 2.

A.2.4 PWM and TOT least squares fit

The figures A.9 and A.10 show the fit of the long-period curves of the TOT and the PWM for several non-consecutive cycles. The matching progression of the curves illustrates that the excessive thruster activation is significant enough to be visible in the attitude roll error. The curves are fitted using a least squares algorithm (LSQ) of the form:

$$X_{LSQ} = a + b \cdot X \tag{A.2}$$

The listed chi^2 values are all $<< 1$ which indicates a good quality of the fit.

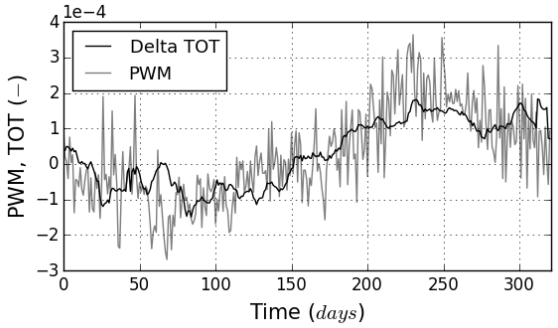

(a) Cycle 2. $chi^2 = 2.76 \cdot 10^{-6}$.

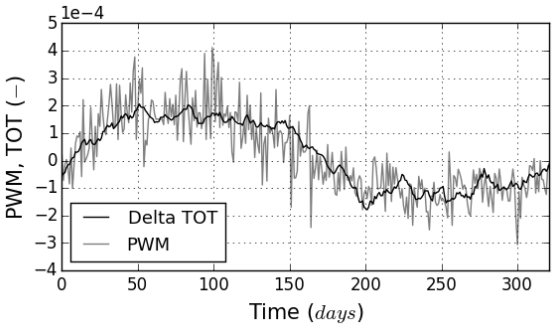

(b) Cycle 6. $chi^2 = 2.14 \cdot 10^{-6}$.

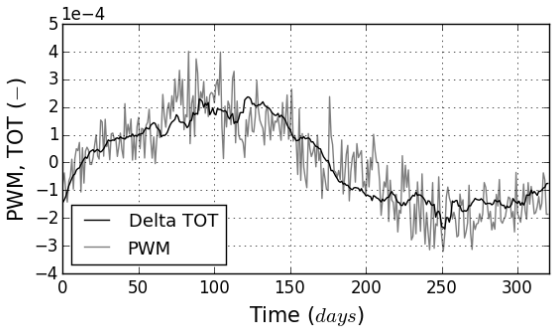

(c) Cycle 12. $chi^2 = 2.29 \cdot 10^{-6}$.

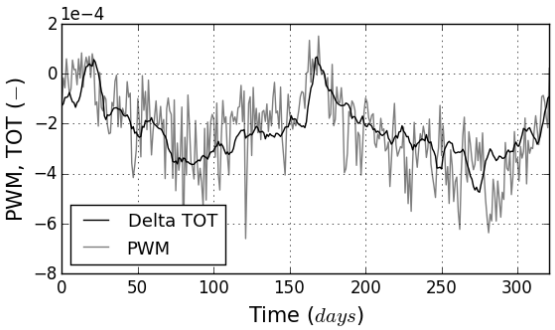

(d) Cycle 15. $chi^2 = 4.64 \cdot 10^{-6}$.

Fig. A.9: Fit of TOT and PWM long-period plots for GRACE 1.

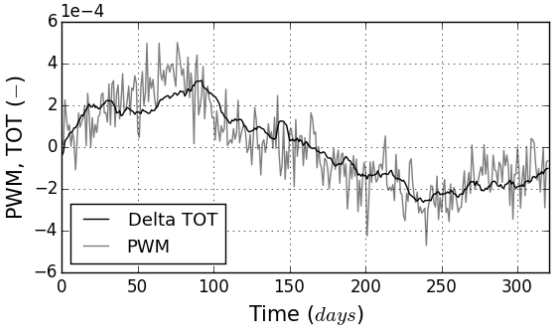

(a) Cycle 2. $chi^2 = 3.48 \cdot 10^{-6}$.

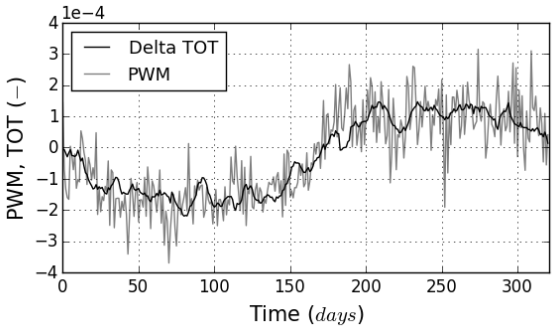

(b) Cycle 6. $chi^2 = 2.08 \cdot 10^{-6}$.

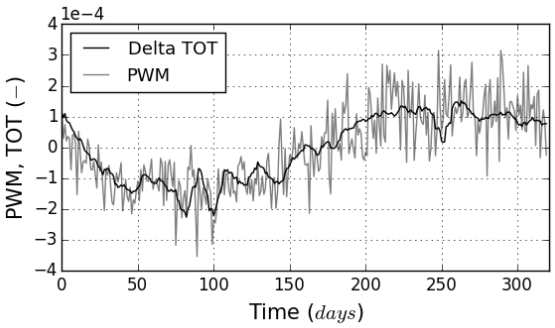

(c) Cycle 12. $chi^2 = 1.97 \cdot 10^{-6}$.

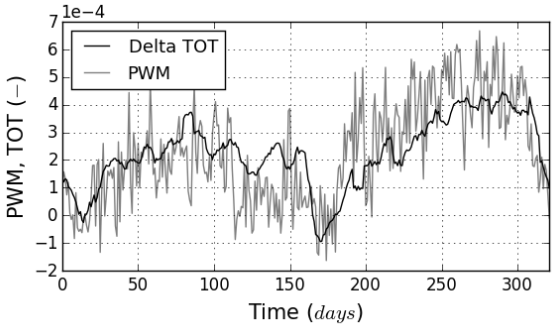

(d) Cycle 15. $chi^2 = 6.38 \cdot 10^{-6}$.

Fig. A.10: Fit of TOT and PWM long-period plots for GRACE 2.

A.2.5 TOT long-period effect

The following plots show the observed long-period thruster behavior for the cycles of GRACE 1 that were not shown in the main text (A.11) and for GRACE 2 (A.12, A.13).

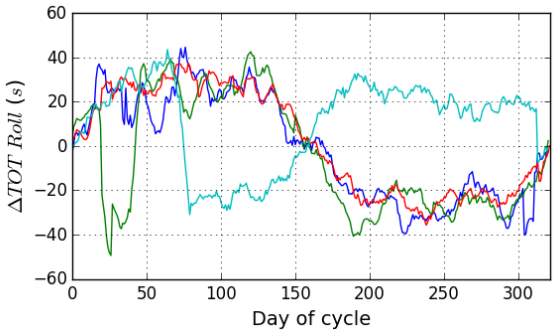

(a) $\triangle TOT$ values in roll. The values show a sine-shaped progression with a period of 321.6 days. The jump in the cyan curve is caused by the satellite swap performed in cycle 5.

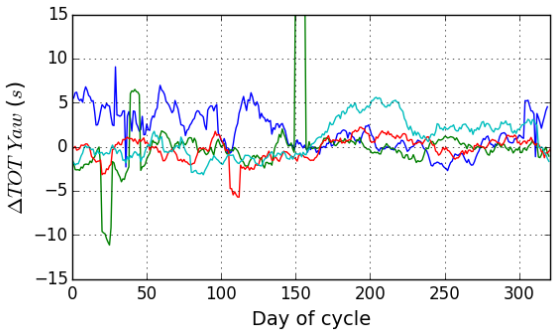

(b) $\triangle TOT$ values in yaw. The periodic effect is barely recognizable stressing the assumption that the effect in yaw is caused by a weak roll-yaw-coupling.

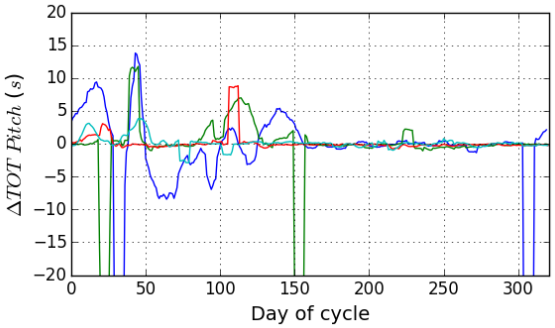

(c) $\triangle TOT$ values in pitch. The values show non-systematic fluctuations about zero. This suggests that the pitch attitude is not influenced by the periodic effect.

Fig. A.11: Illustration of the $\triangle TOT$ observed in the ATH actuation based on data from cycles 2 to 5 (GRACE 1). The values are derived from the sum of all thruster activation (positive and negative) of one day. In roll and yaw a deviation from zero is noticeable indicating a long-period effect on the satellites. The effect is weaker in yaw indicating that it caused by roll-yaw-coupling. In pitch no periodic effect is noticeable.

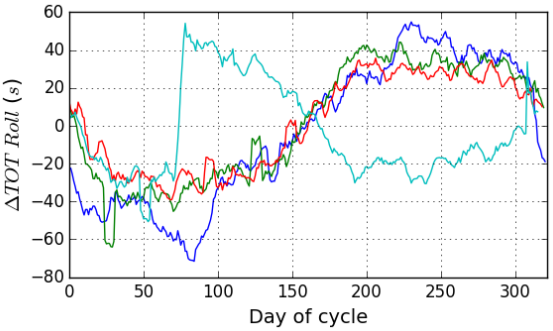

(a) $\triangle TOT$ values in roll. The values show a sine-shaped progression with a period of 321.6 days. The jump in cyan curve is caused by the satellite swap in cycle 5.

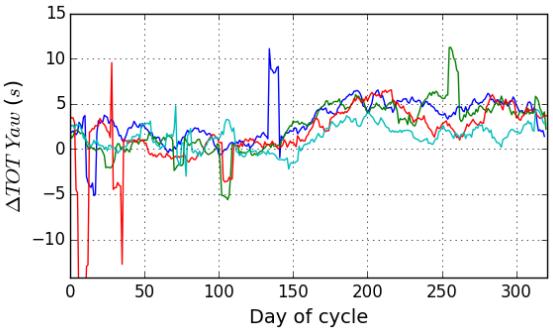

(b) $\triangle TOT$ values in yaw. The pattern is similar compared to roll, but significantly less pronounced.

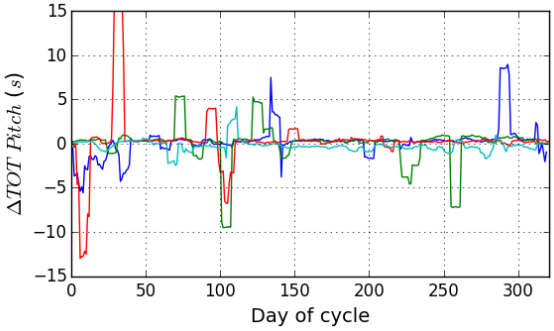

(c) $\triangle TOT$ values in pitch. The values show non-systematic fluctuations about zero. This suggests that the pitch attitude is not influenced by the periodic effect.

Fig. A.12: Illustration of the $\triangle TOT$ observed in the ATH actuation based on data from cycles 2 to 5 (GRACE 2). The values are derived from the sum of all thruster activation (positive and negative) of one day. In roll and yaw a deviation from zero is noticeable indicating a long-period effect on the satellites. The effect is weaker in yaw indicating that it caused by roll-yaw-coupling. In pitch no periodic effect is noticeable.

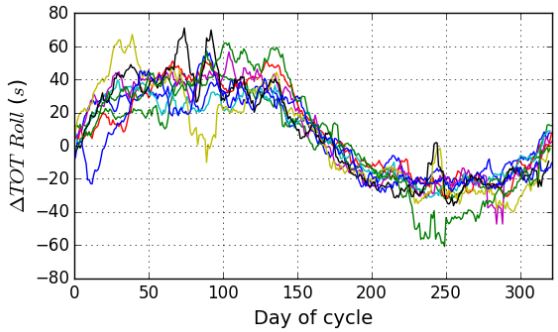

(a) $\triangle TOT$ values in roll. The values show a sine-shaped progression with a period of 321.6 days.

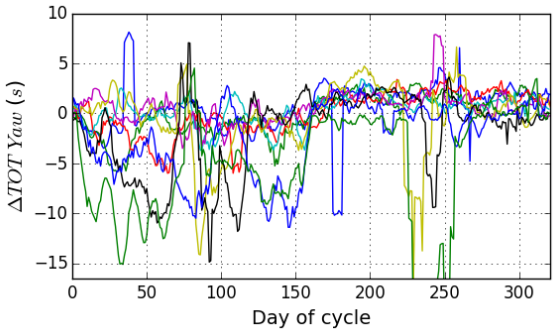

(b) $\triangle TOT$ values in yaw. The sine-shaped effect is barely visible.

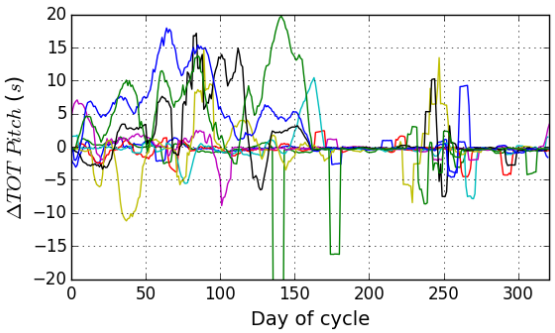

(c) $\triangle TOT$ values in pitch. The values show non-systematic fluctuations about zero. This suggests that the pitch attitude is not influenced by the periodic effect.

Fig. A.13: Illustration of the $\triangle TOT$ observed in the ATH actuation based on data from cycles 6 to 14 (GRACE 2). The values are derived from the sum of all thruster activation (positive and negative) of one day. In roll and yaw a deviation from zero is noticeable indicating a long-period effect on the satellites. The effect is weaker in yaw indicating that it caused by roll-yaw-coupling. In pitch no periodic effect is noticeable.

A.2.6 Orbit analysis

The following figures show the complementary plots for the orbit analysis in chapter 4.3. They show some exemplary orbit the residual magnetic dipole moment (RDM) parameter study was done for. In-depth understanding and modeling of the RDM requires the analysis of an extensive amount of orbits that can not be done in the scope of this work. The few chosen examples comply with the information on the sign of the m_z components gained in chapter 4.2. The sign of the m_y component does not fit in all orbits. This indicates that it is influenced by effects other than the ones identified. It is expected that an extensive study would allow to draw statistical conclusions that would confirm the assumptions made in chapter 4.2.

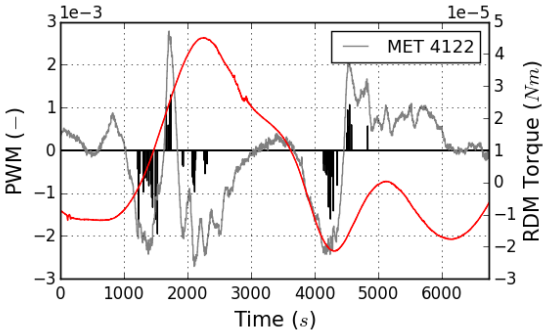

(a) GRACE 1. RDM roll torque for $\vec{m} = (1,-1,-6)^T$. The chosen weighting fits the negative trend of the PWM in the phases before the satellite reaches the poles at 1300s and 4500s. In other phases evaluation is difficult due to intense thruster activation.

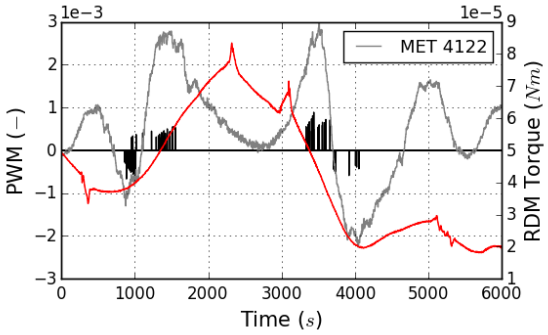

(b) GRACE 2. RDM roll torque for $\vec{m} = (1,1,8)^T$. The chosen weighting complies with the largely positive trend of the PWM visible in the frames (2800-3500)s and (4800-5100)s. In other phases of the orbit the attitude is dominated by AOCS activation.

Fig. A.14: Illustration of the chosen weighting of the RDM components for an orbit in MET 4122. The PWM data was rid of known disturbances to assure the validity of the comparison. A realistic weighting of the components is indicated by a matching progression of the curves. The yaw analysis is missing as it did not allow meaningful judgment regarding the X-component.

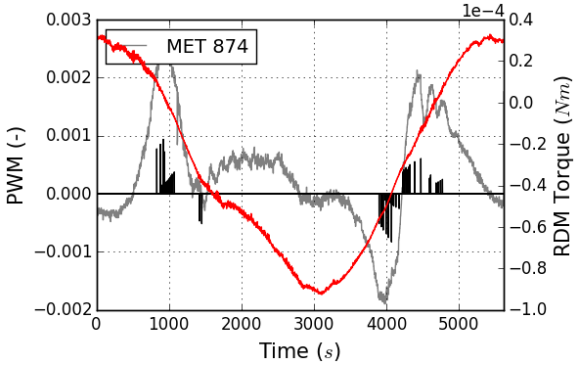

(a) GRACE 1. RDM roll torque for $\vec{m} = (1,-1,-6)^T$. The weighting fits the positive trend of the PWM until the first thruster activation and the negative trend in the second part of the orbit. The chosen weighting of m_z is a bit smaller than the conservative factor 8 chosen in the analysis.

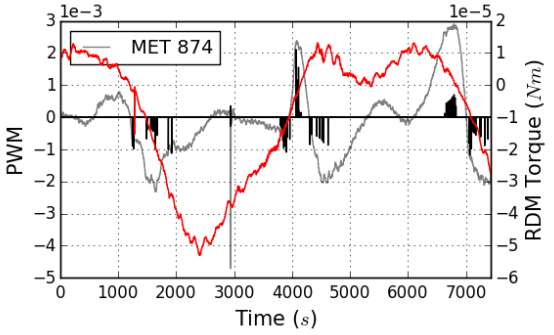

(b) GRACE 2. RDM roll torque for $\vec{m} = (1,1,6)^T$. The torque fits the negative trend of the until 5300s and the positive progression until the end of the shown period. The chosen weighting of m_z is a bit smaller than the conservative factor 8 chosen in the analysis.

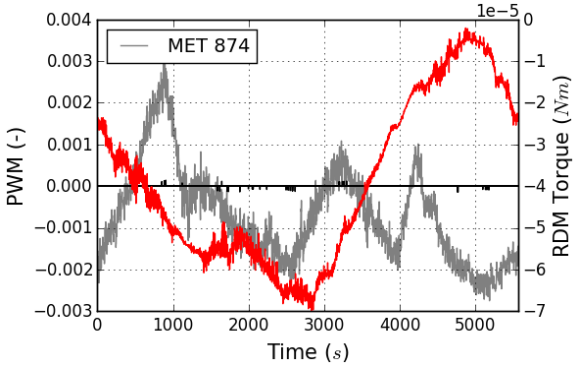

(c) GRACE 1. RDM yaw torque for $\vec{m} = (8,-1,-6)^T$. The PWM is largely influenced by the thruster pulses but a negative trend is visible that fits the chosen weighting.

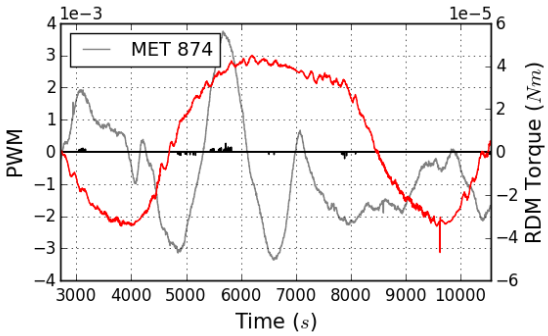

(d) GRACE 2. RDM yaw torque for $\vec{m} = (5,1,6)^T$. The curves fit in the intervals (3500-4500)s and (8500-10500)s. The orbit illustrates that the yaw attitude may be influenced by other effects than the once used in the roll attitude analysis. In the time frame (5500-7000) the trend is dominated by the thruster pulses.

Fig. A.15: Illustration of the chosen weighting of the RDM components for an orbit in MET 874. The PWM data was rid of known disturbances to assure the validity of the comparison. A realistic weighting of the components is indicated by a matching progression of the curves.

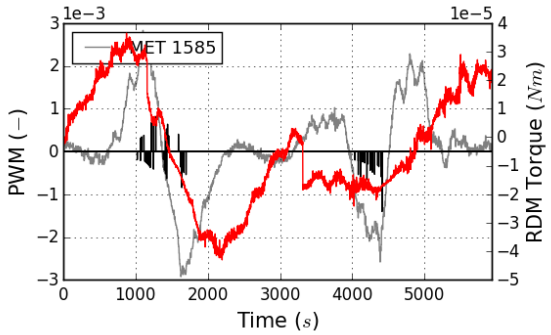

(a) GRACE 1. RDM roll torque for $\vec{m} = (1,-1,-8)^T$. The chosen weighting complies fairly well with the negative trend of the PWM.

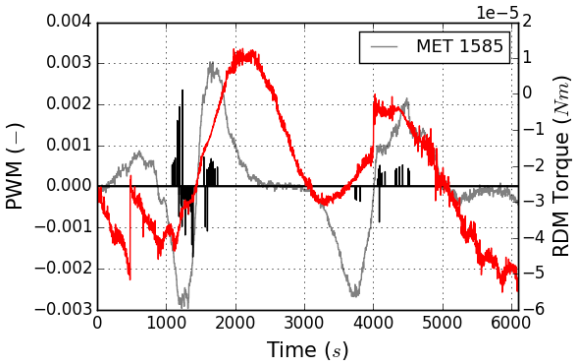

(b) GRACE 2. RDM roll torque for $\vec{m} = (1,1,8)^T$. The chosen weighting complies well with the positive trend of the PWM in the first half of the orbit and with the negative trend in the second half.

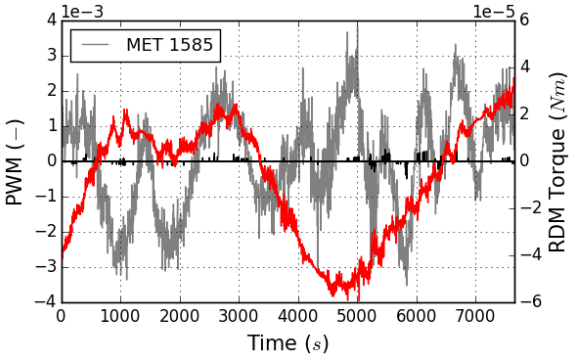

(c) GRACE 1. RDM yaw torque for $\vec{m} = (8,-1,-5)^T$. The trend of the PWM is hard to recognize due to thruster activation, but a negative trend is visible in the second half of the orbit that fits the torque curve.

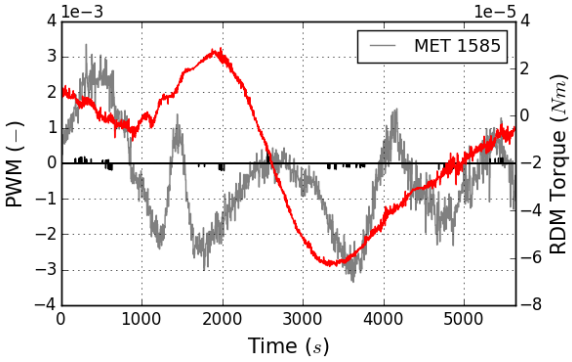

(d) GRACE 2. RDM yaw torque for $\vec{m} = (8,1,8)^T$. The torque approx. fits the positive trend of the PWM until 500 s and the negative trend visible in the frame (2700-3700)s. The weighting of m_x chosen here is 5. In the analysis a conservative value of 8 was chosen.

Fig. A.16: Illustration of the chosen weighting of the RDM components for an orbit in MET 1585. The PWM data was rid of known disturbances to assure the validity of the comparison. A realistic weighting of the components is indicated by a matching progression of the curves.

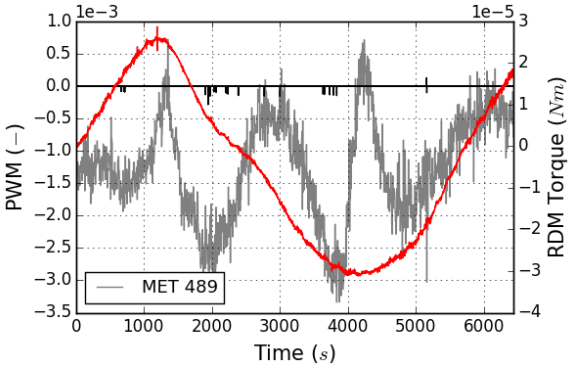

(a) RDM torque for $\vec{m} = (1, -1, -8)^T$. A balanced weighting of m_y and m_z induces a torque that is positive in the first 2500 s opposed to the negative trend of the PWM.

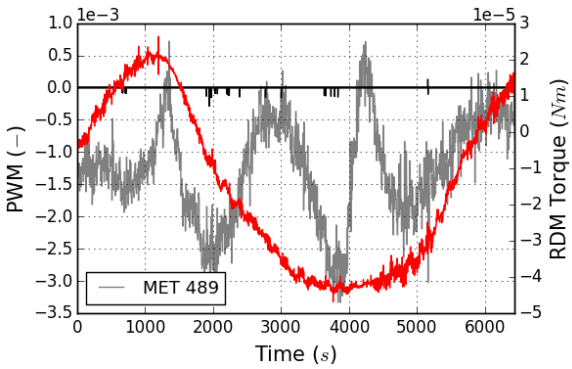

(b) RDM torque for $\vec{m} = (3, -1, -8)^T$. A weighting of m_y reduces the phase where the torque is positive ((0-1800)s).

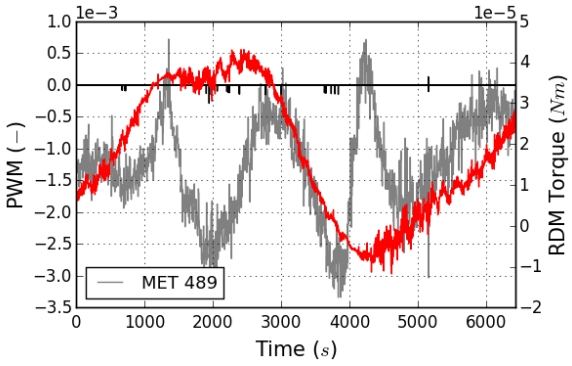

(c) RDM torque for $\vec{m} = (-3, -1, -8)^T$. A negative X-component results in a largely positive torque that does not fit the PWM.

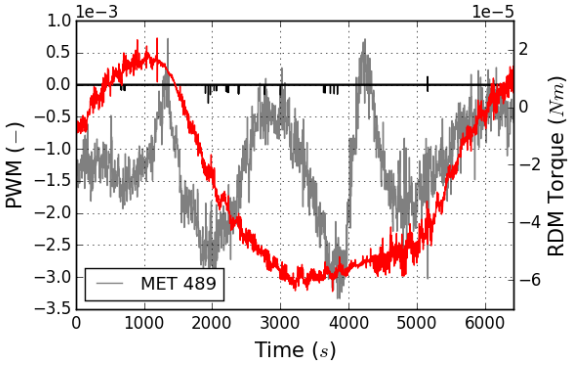

(d) RDM torque for $\vec{m} = (5, -1, -8)^T$. Further weighting of the X-component further reduces the period where the torque is positive ((200-1600)s).

Fig. A.17: Qualitative comparison of the PWM (grey) and RDM **yaw** torque (red) for different weightings of $\vec{m}$ (GRACE 1, MET 489). The PWM data was rid of known disturbances to assure the validity of the comparison. A realistic weighting of the components is indicated by a matching progression of the curves.